18

Viscous effects of the irrotational flow outside boundary layers on rigid solids

High-Reynolds-number flows may be approximated by an outer irrotational flow and small layers on the boundary and narrow wakes where vorticity is important. The irrotational flow gives rise to an extra viscous dissipation over and above the dissipation in the boundary layer. At high Reynolds numbers the viscous dissipation in the irrotational flow outside is a very small fraction of the total which vanishes asymptotically as Reynolds number tends to infinity.

Prandtl's boundary layer theory is asymptotic and does not account for the viscous effects of the outer irrotational flow. Viscous effects on the normal stresses at the boundary of a solid cannot be obtained from Prandtl's theory. It is very well known and easily demonstrated that as a consequence of the continuity equation, the viscous normal stress must vanish on a rigid solid. The only way that viscous effects can act on a boundary is through the pressure but the pressure in Prandtl's theory is not viscous. It is determined by Bernoulli's equation in the irrotational flow and is imposed unchanged on the wall through the thin boundary layer. Therefore the important pressure drag cannot be calculated from Prandtl's theory. In addition, the mismatch between the irrotational shear stress and the shear stress at the outer edge of the boundary layer given by Prandtl's theory is not resolved.

Our work here is motivated by the desire to understand the dynamical effect of the fact that the viscous dissipation of the outer irrotational flow is not zero and that the viscous effects on the normal stress on a solid are due only to the pressure and at finite-Reynolds number, no matter how large, there will be a viscous effect on the pressure, not given in Prandtl's theory. We take into account the viscous effects of the outer irrotational flow; it can be said that this work gives rise to a boundary layer theory at a finite-Reynolds number.

From the previous studies of gas-liquid flows, we have seen two closely related methods to account for the viscous effects of irrotational flows, DM and VCVPF. The dissipation of the outer potential flow increases the drag calculated from the boundary layer alone. Our calculation in this chapter shows that the drag increase is proportional to 1/Re. The pressure correction is the kernel of VCVPF. At the outer edge of the boundary layer, the shear stress evaluated on the boundary layer solution using Prandtl's theory does not necessarily equal the irrotational shear stress; this is analogous to the discrepancy between the zero-shear-stress condition and non-zero irrotational shear stress at a gas-liquid interface. This discrepancy induces vorticity and a pressure correction can be calculated.

The method of VCVPF can only determine the pressure correction at the outer edge of the boundary layer, not the variation through the layer. We develop a new boundary analysis, in which the pressure inside the boundary layer is solved and the continuity of the shear stress at the outer edge of the boundary layer is imposed. This analysis is applied to the problem of the flow past a rapidly rotating cylinder. Inside the boundary layer, the velocity field is decomposed into an irrotational purely rotary flow and a boundary layer flow. Inserting this decomposition into the Navier-Stokes equations, we obtain a new set of equations for the unknown boundary layer flow. This new set of equations can be solved by expanding the solution into a power series. Our solution is in reasonable to excellent agreement with the numerical simulation of Padrino and Joseph (2006). The decomposition for the velocity inside the boundary layer can be regarded as a Helmholtz decomposition. However, the flow outside is approximated by a potential.

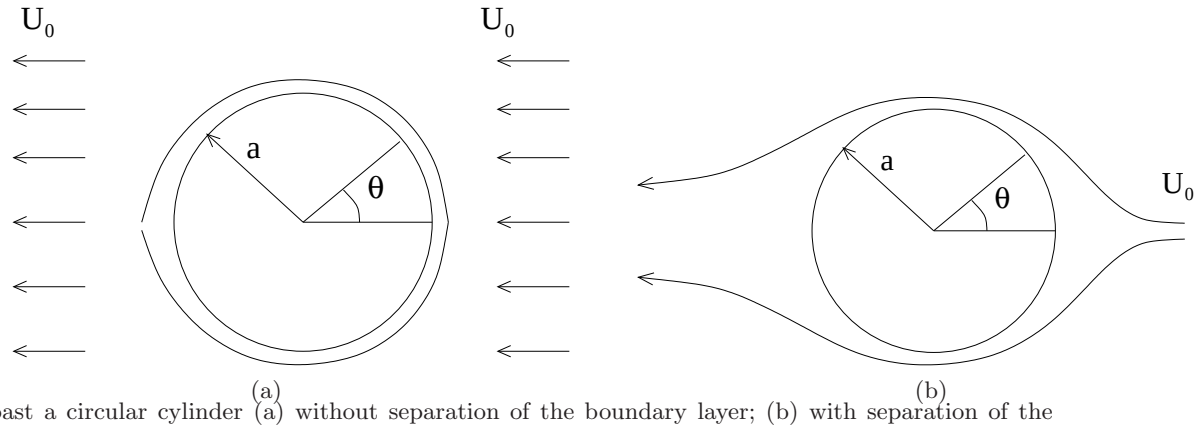

Fig. 18.1. The flow past a circular cylinder (a) without separation of the boundary layer; (b) with separation of the boundary layer.

18.1 Extra drag due to viscous dissipation of the irrotational flow outside the boundary layer

For a body moving with a constant velocity in an otherwise quiescent liquid, the non-zero viscous dissipation of the outer potential flow gives rise to an additional drag, increasing the drag calculated from the boundary layer alone. The drag is considered in three cases here, on a two-dimensional circular gas bubble in a streaming flow, at the edge of the boundary layer around a rapidly rotating cylinder in a uniform flow, and on an airfoil in a streaming flow. The drag may be computed using the dissipation method or the viscous pressure correction of the irrotational pressure.

In Section 18.1.1 we compute the drag on a two-dimensional circular gas bubble using the dissipation method and VCVPF. This problem sets the frame for considerations of the additional drag on the boundary layer around a solid. Figure 18.1 shows the flow past a circular cylinder. Suppose that there is no separation of the boundary layer (figure 18.1.a), the flow is like a uniform flow past a circular gas bubble. The additional drag at the edge of the boundary layer can be computed just like the drag on a gas bubble. Practically, boundary layer separation occurs (figure 18.1.b) and the potential flow solution for the outer flow is not known. One of the methods to suppress separation is to rotate the cylinder rapidly. We compute the additional drag at the edge of the boundary layer of a rapidly rotating cylinder in a uniform flow in Section 18.1.2. The flow past an airfoil, which can be obtained by conformal transformation from the flow over a rotating cylinder, is the subject in Section 18.1.3.

18.1.1 Pressure corrections for the drag on a circular gas bubble

†The drag D per unit length on a stationary circular gas bubble of radius a in a uniform stream $-U_0$ may be obtained using the dissipation method introduced by Levich (1949) to compute the drag on a spherical gas bubble. The steady rise velocity U_0 of the circular gas bubble in the irrotational flow of a viscous liquid can be obtained from the stationary bubble in a uniform stream by a Galilean transformation. This problem is a good frame to set the considerations which lead to viscous effects on boundary layers around solid bodies due to extra pressure generated by the unphysical shear stress as the outer edge of the boundary layer. The solid and its entrained boundary layer can be regarded as a boundary layer bubble.

The irrotational flow of a viscous liquid over a stationary gas bubble is given by viscous potential flow $\mathbf{u} = \nabla\phi$, $\nabla^2\phi = 0$. $p = p_\mathrm{i}$ is the pressure according to Bernoulli's equation; the stress in the liquid is $\mathbf{T} = -p_\mathrm{i}\mathbf{1} + 2\mu\nabla\otimes\nabla\phi$ where μ is the viscosity.

† We call the readers' attention to the fact that in our problem, the uniform flow is from right to left (see figure 18.1). The drag on the bubble is in the uniform flow direction and is negative.

The velocity potential for the stationary gas bubble is

$$\phi = -U_0 r \left(1 + \frac{a^2}{r^2}\right) \cos\theta, \tag{18.1.1}$$

and, at $r = a$ we get

$$u_r = 0 \quad \text{and} \quad u_\theta = 2U_0 \sin\theta \tag{18.1.2}$$

and

$$[\tau_{rr},\, \tau_{r\theta}] = -\frac{4\mu U_0}{a}[\cos\theta,\, \sin\theta] \tag{18.1.3}$$

are the normal and shear stresses, respectively and $p_{\rm i}$ is determined by the Bernoulli's equation

$$p_{\rm i} = p_\infty + \frac{\rho}{2} U_0^2 (1 - 4\sin^2\theta). \tag{18.1.4}$$

The dissipation $\mathcal{D}$ per unit length of the potential flow may be evaluated using the identity

$$\begin{aligned} \mathcal{D} &\equiv \int_V 2\mu \mathbf{D} : \mathbf{D}\, dV = \int_A \mathbf{u} \cdot 2\mu \mathbf{D} \cdot \mathbf{n}\, dA \\ &= \int_A -(u_r \tau_{rr} + u_\theta \tau_{r\theta})\, dA = 8\pi\mu U_0^2, \end{aligned} \tag{18.1.5}$$

where $\mathbf{D}$ is the rate of strain tensor, V is the volume occupied by the fluid and A is the boundary of V. The drag due to the dissipation of the potential flow can then be calculated

$$D = \mathcal{D}/(-U_0) = -8\pi\mu U_0. \tag{18.1.6}$$

A direct calculation of the drag on the bubble, using viscous potential flow to calculate the stress traction at $r = a$ yields a different result

$$D = \int_A \mathbf{e}_x \cdot \mathbf{T} \cdot (-\mathbf{n})\, \mathrm{d}A = \int_A [(-p_{\rm i} + \tau_{rr})\mathbf{e}_x \cdot \mathbf{e}_r + \tau_{r\theta} \mathbf{e}_x \cdot \mathbf{e}_\theta]\, \mathrm{d}A = 0. \tag{18.1.7}$$

This is because the integral of $p_{\rm i}$ vanishes and

$$\int_A \tau_{rr} \mathbf{e}_x \cdot \mathbf{e}_r\, \mathrm{d}A = -\int_A \tau_{r\theta} \mathbf{e}_x \cdot \mathbf{e}_\theta\, \mathrm{d}A. \tag{18.1.8}$$

This result $D = 0$ with a nonzero dissipation $8\pi\mu U_0^2$ is a paradox which is even more paradoxical than D'Alembert's.

In an exact formulation of the flow past a circular bubble, without assuming potential flow, and with $\tau_{r\theta} = 0$ at $r = a$, we have

$$D = \int_A (-p + \tau_{rr}) \mathbf{e}_x \cdot \mathbf{e}_r\, \mathrm{d}A. \tag{18.1.9}$$

The effects of viscosity can enter this integral through p or τ_{rr}.

We next assume that the nonphysical irrotational shear stress $\tau_{r\theta}$ is removed in a boundary layer in which the vorticity is not zero. The thickness δ of the vortical layer is very small at high Reynolds number. The rate of strain in the vortical layer is of the order U_0/a in order that the shear stress be zero; the volume of the vortical layer is of the order $a\delta$ per unit length. Therefore the dissipation per unit length in the vortical layer is of the order $\mu U_0^2 \delta/a$, which is negligible compared the dissipation in the bulk volume (18.1.5). It is further assumed that the boundary layer contribution to τ_{rr} is also negligible. It follows then that the direct calculation of drag can agree with the dissipation calculation only if

$$p = p_{\rm i} + p_{\rm v}, \tag{18.1.10}$$

where $p_{\rm v}$ is the additional contribution to pressure in the vorticity boundary layer. The mechanical energy equation at steady state gives rise to

$$\mathcal{D} \equiv \int_V 2\mu \mathbf{D} : \mathbf{D}\, dV = \int_A \mathbf{u} \cdot \mathbf{T} \cdot \mathbf{n}\, \mathrm{d}A. \tag{18.1.11}$$

Given the structure described above, we have

$$\mathcal{D} = -\int_A u_r(-p_\mathrm{v} + \tau_{rr})\, dA. \tag{18.1.12}$$

Comparing (18.1.12) with (18.1.5), one can see that (12.6.1) holds with $\mathbf{n} = -\mathbf{e}_r$, $\mathbf{t} = -\mathbf{e}_\theta$, $\tau_s = \tau_{r\theta}$ in the case of the circular gas bubble.

The extra pressure must be a 2π periodic solution on the circle and can be represented by a Fourier series

$$-p_\mathrm{v} = \sum_{k=0}^{\infty}(C_k \mathrm{cos}k\theta + D_k \mathrm{sin}k\theta), \tag{18.1.13}$$

Inserting now (18.1.13) and (18.1.3) into (12.6.1), we find that

$$-\int_0^{2\pi} U_0 \mathrm{cos}\theta \left(C_1 \mathrm{cos}\theta + D_1 \mathrm{sin}\theta + \sum_{k\neq 1}(C_k \mathrm{cos}k\theta + D_k \mathrm{sin}k\theta) \right) a\, d\theta = 4\pi\mu U_0^2. \tag{18.1.14}$$

The above integration is performed on the surface of the bubble and the vortical layer is not considered. Evaluation of (18.1.14) using orthogonality gives

$$C_1 = -4\mu U_0/a. \tag{18.1.15}$$

The other coefficients are undetermined. The only term in the Fourier series (18.1.13) entering into the direct calculation of the drag is proportional to $\mathrm{cos}\theta$. Hence

$$D = \int_0^{2\pi} (-p_\mathrm{v} + \tau_{rr})\mathbf{e}_x \cdot \mathbf{e}_r\, a\mathrm{d}\theta = \int_0^{2\pi} (-p_\mathrm{v} + \tau_{rr}) a\mathrm{cos}\theta\, \mathrm{d}\theta = -8\pi\mu U_0 \tag{18.1.16}$$

is the same D as calculated by dissipation method in (18.1.6).

It is of interest to consider the separate contribution to the drag of $-p_\mathrm{v}$ and τ_{rr} in (18.1.16)

$$D = D_{p_\mathrm{v}} + D_{\tau_{rr}} = -4\pi\mu U_0 - 4\pi\mu U_0 = -8\pi\mu U_0. \tag{18.1.17}$$

If somehow the surface of the bubble were made rigid so that the no-slip condition could be realized, then the continuity equation would imply that $D_{\tau_{rr}} = 0$ and D_{p_v} would be the pressure drag on the rigid solid. Moore (1959) calculated the drag on a spherical gas bubble using the viscous normal stress alone and get $D = -8\pi\mu U_0 a$. The Levich drag is $-12\pi\mu U_0 a$ and the difference is the drag $D_{p_\mathrm{v}} = -4\pi\mu U_0 a$, which is, in the present mode of imagination, the viscous drag on a rigid sphere due to the viscous irrotational flow.

The existence and asymptotic validity of a boundary layer of the type assumed here and elsewhere have not been established. The details of the size of the layer, the boundary layer equations, the variation of velocity, vorticity and pressure in the layer have not been given. Kang and Leal (1988a) did calculations from the vorticity equation in the case of the drag on a spherical gas bubble. Results indicating a boundary layer structure of the type described here were obtained but their results are partial and do not give the details listed above.

The nature of the boundary layer may be determined in the appropriate asymptotic limit more easily in two dimensions than in three. In the two dimensional problem we may obtain an exact solution of the stream function equation

$$\frac{1}{r}\frac{\partial\psi}{\partial\theta}\frac{\partial}{\partial r}\nabla^2\psi - \frac{1}{r}\frac{\partial\psi}{\partial r}\frac{\partial}{\partial\theta}\nabla^2\psi = \nu\nabla^4\psi \tag{18.1.18}$$

where

$$\nabla^2\psi = \frac{1}{r}\frac{\partial}{\partial r}\left(r\frac{\partial\psi}{\partial r}\right) + \frac{1}{r^2}\frac{\partial^2\psi}{\partial\theta^2},$$

in the region outside the circle subject to the conditions that

$$\mathbf{u} = -\mathbf{e}_x U_0 \quad \text{at } \infty, \tag{18.1.19}$$

and

$$u_r = 0, \quad \tau_{r\theta} = 0 \quad \text{at } r = a. \tag{18.1.20}$$

This problem is well posed; it is like the flow over a stationary solid cylinder except that the no-slip condition on the tangential velocity on the stationary solid circle is replaced by a zero-shear-stress condition on a circular bubble.

The solution of (18.1.18), (18.1.19) and (18.1.20) determines a stream function $\psi(r,\theta)$. Once this function is determined, the pressure may be determined from the equations of motion and the pressure correction can be obtained.

18.1.2 A rotating cylinder in a uniform stream

†The potential flow over a rotating cylinder in a uniform stream plays an important role in classical airfoil theory in which the flow and airfoil shape is obtained by conformal transformation, and the Kutta condition suppressing separation at the trailing edge is obtained by adjusting the ratio of the rotational speed to the streaming speed.

We study the extra pressure contribution to the drag at the outer edge of Prandtl's boundary layer on a solid cylinder rotating so fast that the separation of the boundary layer is suppressed. We compare the analysis of the extra pressure associated with the viscous dissipation of the irrotational flow outside the boundary layer with a numerical solution of the unapproximated equations for values as close to the appropriate asymptotic values as the numerical solution will allow.

The readers should remember that our work here is motivated by the desire to understand the dynamical effect of the fact that the viscous dissipation of the irrotational flow outside Prandtl's boundary layer is not zero and that the viscous effects on the normal stress on a solid are due only to the pressure and at finite-Reynolds number, no matter how large, there will be a viscous effect on the pressure, not given in Prandtl's theory.

18.1.2.1 Dissipation calculation

We consider the uniform flow $-U_0$ past a fixed circular cylinder with circulation Γ. Suppose no separation of the boundary layer occurs, the flow outside the boundary layer is given by the potential

$$\phi = -U_0 r\left(1+\frac{a^2}{r^2}\right)\cos\theta + \frac{\Gamma\theta}{2\pi}. \tag{18.1.21}$$

The velocity and stress at the surface of the cylinder can be evaluated using (18.1.21):

$$u_r = 0, \quad \text{and} \quad u_\theta = 2U_0\sin\theta + \frac{\Gamma}{2\pi a}; \tag{18.1.22}$$

$$\tau_{rr} = -4\mu U_0\cos\theta/a, \quad \text{and} \quad \tau_{r\theta} = -4\mu U_0\sin\theta/a - \mu\Gamma/(\pi a^2). \tag{18.1.23}$$

The dissipation $\mathcal{D}$ of the potential flow can be evaluated:

$$\mathcal{D} = -\int_A (u_r\tau_{rr} + u_\theta\tau_{r\theta})\,dA = 8\pi\mu U_0^2 + \frac{\mu\Gamma^2}{\pi a^2}. \tag{18.1.24}$$

The dissipation is equal to the sum of the dissipation of an irrotational purely rotary flow and a streaming flow past a fixed cylinder; the cross-terms in $u_\theta\tau_{r\theta}$ do not appear in the dissipation expression because they integrate to zero. The dissipation of the potential flow should be equal to the power of the drag D and the torque T

$$D(-U_0) + T\frac{\Gamma}{2\pi a^2} = \mathcal{D}. \tag{18.1.25}$$

Ackeret (1952) computed the same dissipation for the problem under consideration. He did not consider the torque and equated the dissipation to the power of the drag alone and obtained

$$D = \mathcal{D}/(-U_0) = -8\pi\mu U_0 - \frac{\mu\Gamma^2}{\pi a^2 U_0}. \tag{18.1.26}$$

† We call the readers' attention to the fact that in our problem, the uniform flow is from right to left (see figure 18.1) and the cylinder rotates counter-clockwise. The lift on the cylinder points upward and is positive. The drag on the cylinder is negative if it is in the uniform flow direction; the drag is positive if it is opposite to the uniform flow direction.

Ackeret argued that it is worth to consider the potential flow solution if the viscous liquid is allowed to slip at solid boundaries. He did not mention gas bubbles, liquid-gas flows, the additional drag or the relation of his solution to unphysical irrotational shear stress at the edge of the boundary layer.

We argue that the additional drag cannot be computed from (18.1.25) with the torque T undetermined. We will obtain the additional drag in a later section by computing the pressure correction p_{v}, following the method laid down in our calculation of p_{v} in the case of a circular gas bubble.

18.1.2.2 Boundary layer analysis

Glauert (1957) carried out a boundary layer analysis of the flow past a rotating cylinder. He assumed that the ratio

$$\alpha = 2U_0/Q \tag{18.1.27}$$

where U_0 is magnitude of the uniform stream velocity and Q is the circulatory velocity of the flow at the outer edge of the boundary layer, is smaller than unity and separation is suppressed. He obtained a solution of the boundary layer equations in the form of a power series in α, and deduced the ratio Q/q, where q is the cylinder's peripheral velocity. q is related to the angular velocity Ω of the cylinder by $q = \Omega a$. Glauert's solution suggests that Q is approximately equal to q for large values of q; it follows that

$$\alpha \to 2U_0/q = \frac{2}{q/U_0} \quad \text{as} \quad q \to \infty. \tag{18.1.28}$$

Glauert used Prandtl's boundary layer theory in which the irrotational pressure of the outer flow is imposed on the solid wall through the boundary layer. Assuming that the boundary layer thickness is negligible compared to the cylinder radius, Glauert used the boundary layer equations for steady two-dimensional flows:

$$\frac{\partial u}{\partial x} + \frac{\partial v}{\partial y} = 0, \tag{18.1.29}$$

$$u\frac{\partial u}{\partial x} + v\frac{\partial u}{\partial y} = U\frac{\mathrm{d}U}{\mathrm{d}x} + \nu\frac{\partial^2 u}{\partial y^2}, \tag{18.1.30}$$

where U is the irrotational velocity at the edge of the boundary layer; x is measured round the cylinder circumference and y normal to it. Glauert chose $x = 0$ to be the point at which the surface moves in the same direction as the uniform stream (the top of the cylinder). We will follow his choice here. Let φ represent the polar angle measured from the point $x = 0$, then $\varphi = x/a$. Glauert obtained the following solutions

$$u = Q\left(1 + \alpha f_1^{'}(y)\mathrm{e}^{\imath\varphi} + \alpha^2\left[f_2^{'}(y)\mathrm{e}^{2\imath\varphi} + g_2^{'}(y)\right] + \ldots\right); \tag{18.1.31}$$

$$v = -Q\left[\frac{\imath}{a}\alpha f_1(y)\mathrm{e}^{\imath\varphi} + \frac{2\imath}{a}\alpha^2 f_2(y)\mathrm{e}^{2\imath\varphi} + \ldots\right]; \tag{18.1.32}$$

$$\frac{\partial u}{\partial y} = Q\left(\alpha f_1^{''}\mathrm{e}^{\imath\varphi} + \alpha^2\left[f_2^{''}(y)\mathrm{e}^{2\imath\varphi} + g_2^{''}(y)\right] + \ldots\right), \tag{18.1.33}$$

where $f_1(y)$, $f_2(y)$ and $g_2(y)$ are functions of y and were determined by Glauert. Because $f_1^{'}(0) = f_2^{'}(0) = 0$ and $g_2^{'}(0) > 0$ given by Glauert's solution, the velocity at the surface of the cylinder can be obtained from (18.1.31):

$$q = Q\left(1 + \alpha^2 g_2^{'}(0) + \ldots\right), \tag{18.1.34}$$

which shows that $Q < q$. Since the shear stress at the cylinder surface is given by $\mu(\partial u/\partial y)_{y=0}$, it can be inferred from (18.1.33) that the shear stress is zero at the cylinder surface when α is zero. In other words, when there is no streaming flow but only viscous irrotational rotary flow, Glauert's solution suggests that the shear stress at the cylinder surface is zero. However, the real shear stress is $-2\mu q/a$.

The reason for this discrepancy is that the irrotational rotary flow component is not considered in Glauert's solution, which is an approximation consistent with the assumption that δ/a is negligible compared to 1. Thus

the shear stress induced by the rotary flow is ignored. The irrotational rotary component of the velocity inside the boundary layer can be written as

$$u_{p\varphi} = Q\frac{a+\delta}{r}, \tag{18.1.35}$$

where δ is the thickness of the boundary layer. We propose a simple modification of Glauert's solution

$$u_\varphi = u_{p\varphi} + u_b = Q\left(\frac{a+\delta}{r} + \alpha f_1^{'}(y)\mathrm{e}^{\imath\varphi} + \alpha^2\left[f_2^{'}(y)\mathrm{e}^{2\imath\varphi} + g_2^{'}(y)\right] + \ldots\right); \tag{18.1.36}$$

$$u_r = v_b = -Q\left[\frac{\imath}{a}\alpha f_1(y)\mathrm{e}^{\imath\varphi} + \frac{2\imath}{a}\alpha^2 f_2(y)\mathrm{e}^{2\imath\varphi} + \ldots\right]. \tag{18.1.37}$$

$f_1(y)$, $f_2(y)$, $g_2(y)$ ... are solutions of boundary layer equations (18.1.29) and (18.1.30), which are based on the assumption that δ/a is negligible compared to 1. Under the same assumption, $(a+\delta)/r \approx 1$ inside the boundary layer and (18.1.36) reduces to Glauert's solution (18.1.31). Thus it appears that the $(a+\delta)/r$ term is not consistent with the solutions of $f_1(y)$, $f_2(y)$ and $g_2(y)$. However, (18.1.36) is a simple modification to address the defect of ignoring the irrotational rotary component of the flow inside the boundary layer. We will show that the modified Glauert's solution is in better agreement with numerical simulation data than Glauert's solution. In Section 18.2, we will carry out a new boundary layer analysis for the flow past a rotating cylinder, in which the inconsistency mentioned above is resolved.

A key problem in the boundary layer analysis is to determine the circulatory velocity Q when given the cylinder rotational speed q. At $y = 0$ ($r = a$), (18.1.36) gives rise to

$$\begin{aligned} q &= Q\left[\frac{a+\delta}{a} + \alpha^2 g_2^{'}(0) + \alpha^4 h_4^{'}(0)\right] \\ &= Q\left[1 + \frac{\delta}{a} + 3\left(\frac{U_0}{Q}\right)^2 - 5.76\left(\frac{U_0}{Q}\right)^4\right], \end{aligned} \tag{18.1.38}$$

where Glauert's solutions for g_2 and h_4 have been used and the terms on the order of α^5 or higher are ignored. We invert (18.1.38) to obtain the expression for Q in terms of q

$$\frac{Q}{q} = \frac{1}{1+\delta/a} - 3\left(\frac{U_0}{q}\right)^2 - 3.23\left(1 - 0.803\frac{\delta}{a}\right)\left(\frac{U_0}{q}\right)^4. \tag{18.1.39}$$

If δ/a is ignored, (18.1.39) reduces to

$$\frac{Q}{q} = 1 - 3\left(\frac{U_0}{q}\right)^2 - 3.23\left(\frac{U_0}{q}\right)^4, \tag{18.1.40}$$

which is the same as Glauert's result. When $U_0 = 0$, there is only irrotational purely rotary flow and boundary layer does not exist. Thus $\delta = 0$ and (18.1.39) indicates $Q = q$.

We calculate the shear stress at the cylinder surface. The contribution from the irrotational purely rotary flow is

$$\mu\left(\frac{\partial u_{p\varphi}}{\partial r} - \frac{u_{p\varphi}}{r}\right) = -2\mu Q\frac{a+\delta}{a^2} \quad \text{at } r = a,$$

which is added to Glauert's shear stress to obtain the total shear stress

$$\tau_{r\varphi} = \mu Q\left[-2\frac{a+\delta}{a^2} + \alpha f_1^{''}(0)\mathrm{e}^{\imath\varphi} + \alpha^2\left[f_2^{''}(0)\mathrm{e}^{2\imath\varphi} + g_2^{''}(0)\right] + \ldots\right]. \tag{18.1.41}$$

The torque T on the cylinder is given by

$$T = -a^2\int_0^{2\pi}\tau_{r\varphi}\mathrm{d}\varphi. \tag{18.1.42}$$

Only terms independent of φ in (18.1.41) contribute to (18.1.42) and we obtain

$$T = 8\pi\rho U_0^2 \frac{a(a+\delta)}{R_e}\frac{Q}{U_0} + 4\pi\rho U_0^2 \frac{a^2}{\sqrt{R_e}}\left[\left(\frac{U_0}{Q}\right)^{\frac{1}{2}} - 2.022\left(\frac{U_0}{Q}\right)^{\frac{5}{2}} + \ldots\right], \tag{18.1.43}$$

$$C_T = \frac{T}{2\rho U_0^2 a^2} = 4\pi\left(1+\frac{\delta}{a}\right)\frac{1}{R_e}\frac{Q}{U_0} + \frac{2\pi}{\sqrt{R_e}}\left[\left(\frac{U_0}{Q}\right)^{\frac{1}{2}} - 2.022\left(\frac{U_0}{Q}\right)^{\frac{5}{2}} + \ldots\right], \tag{18.1.44}$$

where C_T is the torque coefficient and

$$R_e = 2U_0 a/\nu \tag{18.1.45}$$

is the Reynolds number based on U_0. The first term on the right hand side of (18.1.43) is the torque induced by the rotary flow component and is on the order of $1/R_e$; the second term is the torque given by Glauert and is on the order of $1/\sqrt{R_e}$. When $R_e \to \infty$, the term by Glauert is the dominant one. However, when R_e is finite and Q/U_0 is large, the first term can be more significant than the second one. When $U_0 = 0$, the torque is equal to $T = 4\pi\mu q a$, which is the torque on the cylinder when there is only the viscous irrotational purely rotary flow.

Glauert cited Reid's (1924) experimental result about the torque

$$T = 20\pi\rho U_0^2 \frac{a^2}{\sqrt{R_e}}, \tag{18.1.46}$$

which was measured for $q = U_0$. Glauert noted that Reid's torque was far above the value given by him and remarked about this discrepancy "... but it is doubtful if it has much accuracy or relevance, in view of the experimental imperfections and also the separation occurring at this low rotational speed." We will compare our torque expression to the results of numerical simulation in which the rotational speed is high and separation is suppressed.

The lift and drag on the cylinder are given by the pressure and shear stress at the wall. The pressure in Glauert's solution is a constant across the boundary layer and is equal to the irrotational pressure at the outer edge of the boundary layer; it does not give drag and the pressure lift can be computed using the classical lift coefficient formula in aerodynamics:

$$C_{L_p} = \frac{\rho U_0 \Gamma}{\rho U_0^2 a} = \frac{2\pi Q}{U_0}. \tag{18.1.47}$$

In our simple modification of Glauert's solution, we add the irrotational rotary flow component $u_{p\varphi}$ to the velocity and the pressure induced by $u_{p\varphi}$ is

$$p_p = p_{pc} - \frac{\rho}{2}u_{p\varphi}^2 = p_{pc} - \frac{\rho}{2}\frac{(a+\delta)^2}{r^2}Q^2, \tag{18.1.48}$$

where p_{pc} is a constant for the pressure. As an approximation, we assume that the total pressure is obtained by a simple addition of p_p and the pressure given by Glauert. On the cylinder surface $r = a$, p_p is independent of θ and does not contribute to the lift. Therefore the pressure lift expression (18.1.47) still holds. After inserting (18.1.39) into (18.1.47), we obtain

$$C_{L_p} = 2\pi\frac{q}{U_0}\left[\frac{1}{1+\delta/a} - 3\left(\frac{U_0}{q}\right)^2 - 3.23\left(1 - 0.803\frac{\delta}{a}\right)\left(\frac{U_0}{q}\right)^4\right]. \tag{18.1.49}$$

Since our Q (18.1.39) is smaller than Glauert's result (18.1.40), our pressure lift is smaller than Glauert's. Glauert did not consider the friction drag and lift, but they can be computed from his solution easily:

$$C_{D_f} = \frac{D_f}{\rho U_0^2 a} = -\frac{2\pi}{\sqrt{R_e}}\sqrt{\frac{Q}{U_0}}, \qquad C_{L_f} = \frac{L_f}{\rho U_0^2 a} = \frac{2\pi}{\sqrt{R_e}}\sqrt{\frac{Q}{U_0}}. \tag{18.1.50}$$

Our simple modification changes the shear stress at the wall only by a constant, thus the expressions for the friction drag and lift do not change, but their values change due to Q.

We compare our simple modification of Glauert's solution, the results of numerical simulation from Padrino and Joseph (2004) and Glauert's solution in table 18.1 (see Section 18.3). Six cases, (R_e, q/U_0)=(200, 4), (200, 5), (400, 4), (400, 5), (400, 6) and (1000, 3), are considered. Though the boundary layer thickness δ/a is not

solution	R_e	q/U_0	δ_L/a	α	C_{L_p}	C_T
Glauert's solution	200	4	-	0.625	20.102	0.215
Modified Glauert's solution	200	4	0.145	0.741	16.961	0.390
Numerical simulation	200	4	-	-	16.961	0.453
Glauert's solution	200	5	-	0.457	27.483	0.195
Modified Glauert's solution	200	5	0.0434	0.480	26.183	0.465
Numerical simulation	200	5	-	-	26.183	0.514
Glauert's solution	400	4	-	0.625	20.102	0.152
Modified Glauert's solution	400	4	0.112	0.714	17.609	0.237
Numerical simulation	400	4	-	-	17.609	0.275
Glauert's solution	400	5	-	0.457	27.483	0.138
Modified Glauert's solution	400	5	0.0354	0.476	26.415	0.272
Numerical simulation	400	5	-	-	26.415	0.297
Glauert's solution	400	6	-	0.365	34.463	0.126
Modified Glauert's solution	400	6	0.0380	0.380	33.087	0.299
Numerical simulation	400	6	-	-	33.087	0.316
Glauert's solution	1000	3	-	1.064	11.812	0.108
Modified Glauert's solution	1000	3	0.0837	1.207	10.409	0.0632
Numerical simulation	1000	3	-	-	10.409	0.118

Table 18.1. *Comparison of the coefficients for the pressure lift and torque on the cylinder obtained from Glauert's solution, the simple modification of Glauert's solution and numerical simulation. In the simple modification of Glauert's solution, we use an effective boundary layer thickness δ_L/a, which is determined by matching C_{L_p} computed from our simple modification (18.1.49) to the results of numerical simulation. For (R_e, q/U_0)=(1000, 3), $\alpha > 1$ for both our simple modification and Glauert's solution. These solutions are not expected to converge to the true results.*

needed in Glauert's solution, it must be prescribed in our simple modification. We choose an effective boundary layer thickness $\delta/a = \delta_L/a$ which is determined by matching C_{L_p} computed from our simple modification (18.1.49) to the results of numerical simulation. Table 18.1 shows that $\delta_L/a \ll 1$, δ_L/a decreases with increasing R_e at a fixed q/U_0, and δ_L/a generally decreases with increasing q/U_0, because the rotary flow suppresses the boundary layer. The torque coefficient is not sensitive to the choice of δ/a as long as $\delta/a \ll 1$, which can be seen from (18.1.44) and (18.1.39). The pressure lift and torque in numerical simulation are obtained by integration at the cylinder surface. The values of $\alpha = 2U_0/Q$ are listed for Glauert's solution and our simple modification for each pair of R_e and q/U_0. For (R_e, q/U_0)=(1000, 3), $\alpha > 1$ for both our simple modification and Glauert's solution. These solutions are not expected to converge to the true results. A comparison of the solutions with $\alpha < 1$ shows that the values of C_{L_p} from our simple modification and numerical simulation are smaller than those from Glauert's solution; the values of the torque from our simple modification are much closer to the numerical results than those from the Glauert's solution.

If the results of numerical simulation are not available, our analysis cannot provide the value of δ/a. Then Glauert's pressure lift may be taken as a reasonable approximation, and the torque coefficient may be computed from (18.1.44) with $\delta/a = 0$. Since the torque coefficient is not sensitive to the choice of δ/a, it still improves Glauert's solution of the torque substantially.

18.1.2.3 Pressure correction and the additional drag

We consider the pressure correction at the outer edge of the boundary layer and the additional drag induced by it. The shear stress at the outer edge of the boundary layer can be computed in two ways: from the outside potential flow or from the boundary layer solution. If we consider a rotating cylinder with its entrained boundary layer moving with U_0 in a liquid, the potential flow outside $r = a + \delta$ has the following velocity

$$u_\theta = U_0 \frac{(a+\delta)^2}{r^2} \sin\theta + Q \frac{a+\delta}{r}, \quad u_r = U_0 \frac{(a+\delta)^2}{r^2} \cos\theta. \tag{18.1.51}$$

The irrotational shear stress at $r = a + \delta$ is

$$\tau_{r\theta} = -\mu \left(\frac{4U_0 \sin\theta}{a+\delta} + \frac{2Q}{a+\delta} \right). \tag{18.1.52}$$

The shear stress from the boundary layer analysis is

$$\begin{aligned} \tau_{r\theta} &= \mu \left(\frac{\partial u_{p\varphi}}{\partial r} - \frac{u_{p\varphi}}{r} + \frac{\partial u_b}{\partial y} + \frac{\partial v_b}{\partial x} \right) \\ &= \mu \left[-2Q \frac{a+\delta}{r^2} + Q\alpha f_1''(y) \sin\theta + \ldots + Q \frac{\alpha}{a^2} f_1 \sin\theta + \ldots \right]. \end{aligned} \tag{18.1.53}$$

Glauert's solution gives $f_1''(\delta) \approx 0$ and $f_1(\delta) \sim O(\delta)$, which is negligible. Thus the shear stress at $r = a + \delta$ from the boundary layer solution is approximately

$$\tau_{r\theta} \approx -\mu \frac{2Q}{a+\delta}. \tag{18.1.54}$$

Comparing (18.1.52) with (18.1.54), we can see that the shear stress is not continuous and the discrepancy is

$$\tau_{r\theta}^d = -\mu \frac{4U_0 \sin\theta}{a+\delta}. \tag{18.1.55}$$

This shear stress discrepancy induces extra vorticity at the outer edge of the boundary layer and a pressure correction. The power of the pressure correction is equal to the power of the shear stress discrepancy

$$-\int_0^{2\pi} u_r(-p_{\mathrm{v}})(a+\delta)\,\mathrm{d}\theta = -\int_0^{2\pi} u_\theta \tau_{r\theta}^d (a+\delta)\,\mathrm{d}\theta = 4\pi\mu U_0^2. \tag{18.1.56}$$

Again we expand the pressure correction as a Fourier series (18.1.13) and insert it into (18.1.56)

$$-\int_0^{2\pi} U_0 \cos\theta \left(C_1 \cos\theta + D_1 \sin\theta + \sum_{k\neq 1} (C_k \cos k\theta + D_k \sin k\theta) \right) (a+\delta)\,d\theta = 4\pi\mu U_0^2 \tag{18.1.57}$$

which gives rise to

$$\begin{aligned} -C_1 &= \frac{4\mu U_0}{a+\delta} \quad \text{and} \\ p_{\mathrm{v}} &= \frac{4\mu U_0}{a+\delta} \cos\theta - D_1 \sin\theta - \sum_{k\neq 1} (C_k \cos k\theta + D_k \sin k\theta). \end{aligned} \tag{18.1.58}$$

We evaluate the additional drag by direct integration of the traction vector at the outer edge of the boundary layer

$$D = \int_0^{2\pi} [(-p_{\mathrm{i}} - p_{\mathrm{v}} + \tau_{rr})\mathbf{e}_x \cdot \mathbf{e}_r + \tau_{r\theta} \mathbf{e}_x \cdot \mathbf{e}_\theta](a+\delta)\,\mathrm{d}\theta, \tag{18.1.59}$$

where τ_{rr} is the viscous normal stress evaluated on the potential flow velocity (18.1.51), $\tau_{r\theta}$ is the shear stress (18.1.54) evaluated using the boundary layer solution. The above choices are made because τ_{rr} is essentially continuous at the outer edge of the boundary layer but $\tau_{r\theta}$ is not; we choose $\tau_{r\theta}$ from the boundary layer solution and this is analogous to using zero shear stress at a gas-liquid interface. The irrotational pressure p_{i} does not contribute to the drag and we may write (18.1.59) as

$$\begin{aligned} D &= \int_0^{2\pi} (-p_{\mathrm{v}}) \cos\theta (a+\delta)\,\mathrm{d}\theta + \int_0^{2\pi} \tau_{rr} \cos\theta (a+\delta)\,\mathrm{d}\theta - \int_0^{2\pi} \tau_{r\theta} \sin\theta (a+\delta)\,\mathrm{d}\theta \\ &= -4\pi\mu U_0 - 4\pi\mu U_0 - 0 = -8\pi\mu U_0, \end{aligned} \tag{18.1.60}$$

which is the same as the drag on a circular gas bubble (18.1.16). Our additional drag (18.1.60) is much smaller than the one (18.1.26) computed by Ackeret (1952) when the rotational velocity is much larger than the streaming velocity. Equation (18.1.60) indicates that the additional drag only depends on the forward speed U_0 and not on the spinning speed q. The additional drag should be the drag evaluated at the outer edge of the boundary layer, but the boundary layer thickness does not affect the additional drag since δ/a does not appear in (18.1.60).

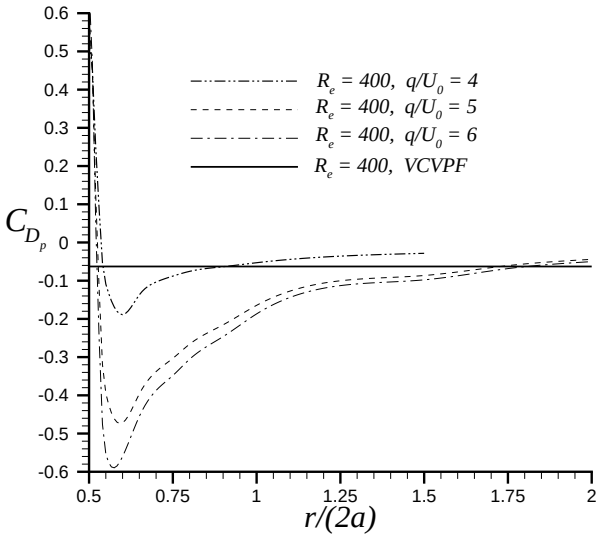

Fig. 18.2. The pressure drag coefficient C_{D_p} at different radial position $r/(2a)$ computed from numerical simulation (18.1.62) for R_e=400: dash-double-dotted line - q/U_0= 4; dashed line - q/U_0= 5; dash-dotted line - q/U_0= 6. The solid straight line gives C_{D_p} computed from (18.1.61) for R_e=400. Each curve for $C_{D_p}(r)$ has two intersections with the straight line, at which C_{D_p} given by (18.1.61) is equal to C_{D_p} computed from numerical simulation at $r = a + \delta$.

If we only consider the additional drag due to the pressure, we obtain

$$D_p = -4\pi\mu U_0 \quad \text{and} \quad C_{D_p} = \frac{D_p}{\rho U_0^2 a} = -\frac{8\pi}{R_e}, \tag{18.1.61}$$

which should be compared to C_{D_p} computed from numerical simulation at the outer edge of the boundary layer. However, in practice the vorticity extends to infinity and a clear-cut boundary layer edge does not exist. To address this difficulty, we present C_{D_p} computed from numerical simulation at different values of r

$$C_{D_p}(r) = \frac{1}{\rho U_0^2 a} \int_0^{2\pi} (-p)\mathbf{e}_x \cdot \mathbf{e}_r \, r \, \mathrm{d}\theta, \tag{18.1.62}$$

and compare to C_{D_p} from (18.1.61). As an example, we plot $C_{D_p}(r)$ from numerical simulation for $R_e = 400$ and q/U_0=4, 5 and 6 in figure 18.2; the straight line gives C_{D_p} computed from (18.1.61) for $R_e = 400$. Note that the results of numerical simulation depend on q/U_0 but equation (18.1.61) does not. Each curve for $C_{D_p}(r)$ has two intersections with the straight line, the one close to the wall denoted by δ_{D1}/a and the other one far way from the wall denoted by δ_{D2}/a. In table 18.2 we list the values of δ_{D1}/a and δ_{D2}/a for (R_e, q/U_0)=(200, 4), (200, 5), (400, 4), (400, 5), (400, 6) and (1000, 3). The vorticity field in the whole domain was computed in numerical simulation. The magnitude of the vorticity on the circle with the radius $r = a + \delta_{D1}$ or $r = a + \delta_{D2}$ was estimated from the numerical data and expressed as a certain percentage of the maximum magnitude of the vorticity field. This percentage is between 12.6% to 20.4% at $r = a + \delta_{D1}$ and is between 0.003% to 0.913% at $r = a + \delta_{D2}$. This percentage is 20.6% at $r = a + \delta_{D1}$ for (R_e, q/U_0) = (400, 6), which indicates that roughly speaking, the vorticity magnitude at a radial position $r > a + \delta_{D1}$ is less than 20.6% of the maximum vorticity magnitude. The reason is that the vorticity magnitude generally decreases as r increases. When $r > a + \delta_{D2}$, the vorticity is almost negligible.

A comparison of table 18.1 and 18.2 shows that δ_{D1}/a is close to the effective boundary layer thickness δ_L/a determined by matching C_{L_p}. When we insert δ_{D1}/a into the expressions for C_{L_p} and C_T on the cylinder, (18.1.49) and (18.1.44) respectively, the results are in fair agreement with the numerical simulation and are better than Glauert's solutions (see table 18.3 and table 18.1). Thus δ_{D1}/a can be used not only as an effective boundary layer thickness for C_{D_p}, but also for C_{L_p} and C_T. This result shows that one effective boundary layer thickness for both the VCVPF calculation and the simple modification of Glauert's solution exists.

Figure 18.2 shows that C_{D_p} changes significantly with r near the wall; C_{D_p} reaches its minimum then

R_e	q/U_0	C_{D_p}	δ_{D1}/a	vorticity %	δ_{D2}/a	vorticity %
200	4	-0.126	0.161	13.1	0.594	0.913
200	5	-0.126	0.0838	14.6	2.03	0.00455
400	4	-0.0628	0.0835	18.1	0.811	0.418
400	5	-0.0628	0.0553	20.8	2.46	0.00340
400	6	-0.0628	0.0473	20.7	2.65	0.00365
1000	3	-0.0251	0.0552	20.4	1.56	0.0139

Table 18.2. *The values of δ_{D1}/a and δ_{D2}/a at which C_{D_p} given by (18.1.61) is equal to C_{D_p} computed from numerical simulation (18.1.62). The magnitude of the vorticity on the circle with the radius $r = a + \delta_{D1}$ or $r = a + \delta_{D2}$ was estimated from the numerical data and expressed as a certain percentage of the maximum magnitude of the vorticity field. This percentage is between 12.6% to 20.4% at $r = a + \delta_{D1}$ and is between 0.003% to 0.913% at $r = a + \delta_{D2}$.*

R_e	q/U_0	δ_{D1}/a	α	C_{L_p}	C_T
200	4	0.161	0.754	16.659	0.388
200	5	0.0838	0.501	25.065	0.466
400	4	0.0835	0.691	18.188	0.239
400	5	0.0553	0.486	25.845	0.273
400	6	0.0473	0.384	32.765	0.299
1000	3	0.0552	1.157	10.862	0.0718

Table 18.3. *The calculation of C_{L_p} (18.1.49) and C_T (18.1.44) on the cylinder using δ_{D1}/a determined by matching C_{D_p} as an effective boundary layer thickness. The results are in fair agreement with the numerical data shown in table 18.1. This demonstrates that δ_{D1}/a can be used not only as an effective boundary layer thickness for C_{D_p}, but also for C_{L_p} and C_T.*

increases; the magnitude of C_{D_p} approaches zero as r increases to infinity. In the region near the second intersection $r = a + \delta_{D2}$, the C_{D_p} curve is rather flat and the straight line given by (18.1.61) is a reasonable approximation to the numerical results. This region may be viewed as a transition region from the inner flow where the vorticity is important to the outer flow where the vorticity is negligible. The VCVPF calculation cannot predict variation of C_{D_p} near the wall.

The term $D_1 \sin\theta$ in the pressure correction should give rise to an extra lift force in addition to the contribution from the irrotational pressure. However, D_1 is not determined in the VCVPF calculation. In the new boundary layer analysis in Section 18.3 the pressure is not assumed to be a constant across the boundary layer and it is solved from the governing equations. We determined the terms proportional to $\sin\theta$, $\cos\theta$, $\sin 2\theta$ and $\cos 2\theta$ up to $O(\alpha^2)$.

18.1.3 The additional drag on an airfoil by dissipation method

We consider a symmetrical Joukowski airfoil moving in a liquid at an angle of attack β with a constant velocity U_0 (figure 18.3). The airfoil is obtained by the Joukowski transformation

$$z = \zeta + \frac{c^2}{\zeta}, \tag{18.1.63}$$

in conjunction with a circle in the ζ plane. The radius a of the circle is slightly larger than the transformation coefficient c,

$$a = c + m = c(1 + \varepsilon), \tag{18.1.64}$$

where $\varepsilon = m/c$ is assumed to be small compared with unity. The center of the circle is displaced from the origin to $(-m, 0)$, so that the circle passes through one of the critical points of the Joukowski transformation, $\zeta = c$, which gives rise to the cusp of the airfoil in the z plane.

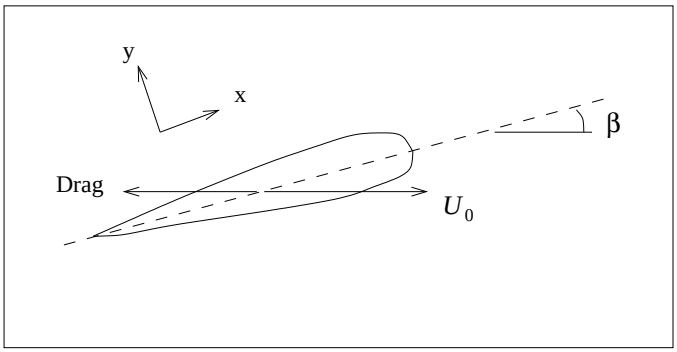

Fig. 18.3. A symmetrical airfoil moving in a liquid at an angle of attack β with a constant velocity U_0. The additional drag on the airfoil computed using the dissipation method is opposite to the moving direction of the airfoil and is defined as negative.

In the ζ plane, a generic point (r, θ) on the circle satisfies

$$(c+m)^2 = r^2 + m^2 + 2rm\cos\theta, \tag{18.1.65}$$

which leads to

$$r = -m\cos\theta + \sqrt{c^2 + 2cm + m^2\cos^2\theta}. \tag{18.1.66}$$

The airfoil surface is then given by

$$z = r\mathrm{e}^{\imath\theta} + \frac{c^2}{r}\mathrm{e}^{-\imath\theta}, \tag{18.1.67}$$

or

$$x = \left(r + \frac{c^2}{r}\right)\cos\theta \quad \text{and} \quad y = \left(r - \frac{c^2}{r}\right)\sin\theta. \tag{18.1.68}$$

The complex potential for a uniform flow past a circle with circulation is

$$f(\zeta) = U_0\left[(\zeta+m)\mathrm{e}^{-\imath\beta} + \frac{a^2}{\zeta+m}\mathrm{e}^{\imath\beta}\right] + \frac{\imath\Gamma}{2\pi}\log\left(\frac{\zeta+m}{a}\right). \tag{18.1.69}$$

Equation (18.1.69) along with the inverse Joukowski transformation

$$\zeta = \frac{z}{2} \pm \sqrt{\frac{z^2}{4} - c^2} \tag{18.1.70}$$

gives the potential for the flow past an airfoil in the z plane. The Kutta condition requires the circulation to be

$$\Gamma = 4\pi U_0 a\sin\beta. \tag{18.1.71}$$

The dissipation calculation will be carried out in dimensionless form. We choose U_0 and c to be the scales for velocity and length, respectively. The dimensionless form of the potential is

$$\frac{f(\zeta)}{U_0 c} = (\zeta+\varepsilon)\mathrm{e}^{-\imath\beta} + \frac{(1+\varepsilon)^2}{\zeta+\varepsilon}\mathrm{e}^{\imath\beta} + 2\imath\sin\beta(1+\varepsilon)\log\left(\frac{\zeta+\varepsilon}{1+\varepsilon}\right). \tag{18.1.72}$$

Note that we use the same symbols for the dimensional and dimensionless variables. The inverse Joukowski transformation in the dimensionless form is

$$\zeta = \frac{z}{2} \pm \sqrt{\frac{z^2}{4} - 1}. \tag{18.1.73}$$

The velocities can be evaluated on the potential

$$u = \frac{1}{2}\left(\frac{\mathrm{d}f}{\mathrm{d}z} + \frac{\mathrm{d}\bar{f}}{\mathrm{d}\bar{z}}\right) \quad \text{and} \quad v = \frac{\imath}{2}\left(\frac{\mathrm{d}f}{\mathrm{d}z} - \frac{\mathrm{d}\bar{f}}{\mathrm{d}\bar{z}}\right) \tag{18.1.74}$$

β	ε =0.3	ε =0.2	ε =0.1	ε =0.05	ε =0.01
0	4.34	3.48	2.53	2.05	1.67
$\pi/20$	6.24	6.30	9.39	22.7	410
$\pi/10$	11.8	14.5	29.3	82.8	1.59×10^3
$\pi/6$	23.7	32.3	72.6	213	4.17×10^3
$\pi/4$	43.2	61.1	142	424	8.34×10^3

Table 18.4. *The integral I as a function of the attack angle β and the nose sharpness parameter ε (the smaller ε, the sharper the nose). The drag coefficient can be obtained by $C_D = -I/(2R_e^{'})$, where the Reynolds number $R_e^{'} = \dfrac{\rho U_0 c}{\mu}$. Here $c \approx l/4$, where l is the length of the airfoil.*

and the rate of strain tensor is

$$2\mathbf{D} = \begin{bmatrix} \frac{\mathrm{d}^2 f}{\mathrm{d}z^2} + \frac{\mathrm{d}^2 \bar{f}}{\mathrm{d}\bar{z}^2} & \imath\left(\frac{\mathrm{d}^2 f}{\mathrm{d}z^2} - \frac{\mathrm{d}^2 \bar{f}}{\mathrm{d}\bar{z}^2}\right) \\ \imath\left(\frac{\mathrm{d}^2 f}{\mathrm{d}z^2} - \frac{\mathrm{d}^2 \bar{f}}{\mathrm{d}\bar{z}^2}\right) & -\left(\frac{\mathrm{d}^2 f}{\mathrm{d}z^2} + \frac{\mathrm{d}^2 \bar{f}}{\mathrm{d}\bar{z}^2}\right) \end{bmatrix}. \tag{18.1.75}$$

The surface of the airfoil is given by

$$x = \left(r + \frac{1}{r}\right)\cos\theta \quad \text{and} \quad y = \left(r - \frac{1}{r}\right)\sin\theta, \tag{18.1.76}$$

where

$$r = -\varepsilon\cos\theta + \sqrt{1 + 2\varepsilon + \varepsilon^2\cos^2\theta}. \tag{18.1.77}$$

Let $\dot{x} = \mathrm{d}x/\mathrm{d}\theta$ and $\dot{y} = \mathrm{d}y/\mathrm{d}\theta$, then the norm on the surface can be written as

$$\mathbf{n} = n_x\mathbf{e}_x + n_y\mathbf{e}_y = \frac{-\dot{y}\mathbf{e}_x + \dot{x}\mathbf{e}_y}{\sqrt{\dot{x}^2 + \dot{y}^2}}, \tag{18.1.78}$$

and

$$\mathrm{d}s = \sqrt{\dot{x}^2 + \dot{y}^2}\mathrm{d}\theta. \tag{18.1.79}$$

Now we calculate the dissipation

$$\mathcal{D} = \mu U_0^2 \int_A \mathbf{u}\cdot 2\mathbf{D}\cdot\mathbf{n}\, dA = \mu U_0^2 I, \tag{18.1.80}$$

where

$$I = \int_0^{2\pi} \left[n_x(2\mathbf{D})_{xx}u + n_x(2\mathbf{D})_{xy}v + n_y(2\mathbf{D})_{yx}u + n_y(2\mathbf{D})_{yy}v\right]\sqrt{\dot{x}^2 + \dot{y}^2}\mathrm{d}\theta. \tag{18.1.81}$$

The integral I is computed numerically. The additional drag is then obtained $D = \mathcal{D}/(-U_0)$ and the drag coefficient

$$C_D = \frac{D}{\frac{1}{2}\rho U_0^2 4c} = -\frac{\mu U_0 I}{\frac{1}{2}\rho U_0^2 4c} = -\frac{1}{R_e^{'}}\frac{I}{2}, \tag{18.1.82}$$

where the Reynolds number is

$$R_e^{'} = \frac{\rho U_0 c}{\mu}. \tag{18.1.83}$$

The drag coefficient depends on the parameter ε and the angle of attack β. The parameter ε determines the maximum thickness of the airfoil and the roundness of the leading nose. The smaller ε, the thinner the airfoil and the sharper the leading nose. In table 18.4 we present the magnitude of the drag coefficient multiplied by the Reynolds number as a function of the parameter ε and the angle of attack β. When ε is fixed, the magnitude of the drag coefficient increases with β. The reason is that when β is not zero, the stream must turn around the leading nose and a large amount of dissipation is generated near the leading nose. When β is fixed at zero, the dissipation decreases as ε decreases. This is because a slimmer airfoil leads to less disturbance to the uniform

flow and smaller dissipation. At the limit when ε is zero, the flow becomes a uniform flow past a flat plate at a zero attack angle, in which the drag is zero. However, when β is fixed at non-zero values, the magnitude of the drag coefficient increases as ε decreases. The reason is that the major contribution to the dissipation is from the flow which turns around the leading nose. A smaller value of ε leads to a sharper leading nose and larger dissipation. At the limit when ε is zero, the leading edge coincide with one of the critical points of the Joukowski transformation, the velocity at the leading edge is singular and the dissipation calculation breaks down.

If the Reynolds number is in the order of hundreds or thousands, the additional drag is negligible when $\beta = 0$ or when β is small and the airfoil is not very sharp at the leading edge; the additional drag is evident when β is non-zero and the airfoil has a very sharp leading edge.

18.1.4 Discussion and conclusion

This work concerns the drag on a body moving at a constant velocity $U_0\mathbf{e}_\imath$ in an otherwise quiescent viscous liquid. The Reynolds number is high and the flow can be approximated by an outer potential flow and a boundary layer adjacent to the surface of the body. The drag is defined as

$$D = \int_A \mathbf{e}_\imath \cdot \mathbf{T} \cdot (-\mathbf{n})\, \mathrm{d}A. \tag{18.1.84}$$

The dissipation calculation is one of the methods to compute the drag and it is based on the mechanical energy equation:

$$\frac{\mathrm{d}}{\mathrm{d}t}\int_V \frac{\rho|\mathbf{u}|^2}{2}\, \mathrm{d}V = \int_A \mathbf{u}\cdot\mathbf{T}\cdot\mathbf{n}\, \mathrm{d}A - \int_V 2\mu\mathbf{D}:\mathbf{D}\, \mathrm{d}V. \tag{18.1.85}$$

At steady state, (18.1.85) becomes

$$\int_A \mathbf{u}\cdot\mathbf{T}\cdot\mathbf{n}\, \mathrm{d}A = \int_A \left[\mathbf{u}\cdot\mathbf{n}(-p+\tau_n) + \mathbf{u}\cdot\mathbf{t}\tau_s\right]\, \mathrm{d}A = \mathcal{D}. \tag{18.1.86}$$

If the body is a gas of negligible density and viscosity, the shear stress τ_s is zero at the interface. The continuity of the normal velocity at the gas-liquid interface gives $\mathbf{u}\cdot\mathbf{n} = U_0\mathbf{e}_\imath\cdot\mathbf{n}$. Thus (18.1.86) can be written as

$$\int_A U_0\mathbf{e}_\imath\cdot\mathbf{n}(-p+\tau_n)\, \mathrm{d}A = \mathcal{D} \qquad \Rightarrow \qquad U_0(-D) = \mathcal{D} = \mathcal{D}_{BL} + \mathcal{D}_P, \tag{18.1.87}$$

where $\mathcal{D}_{BL}$ is the dissipation inside the boundary layer and $\mathcal{D}_P$ is the dissipation of the outer potential flow. In gas-liquid flows, the boundary layer is assumed to be very weak and $\mathcal{D}_{BL}$ is negligible to the first order approximation. Thus we have the drag on a gas body

$$D \approx \mathcal{D}_P/(-U_0), \tag{18.1.88}$$

which is used in our calculation of the drag on a circular gas bubble in Section 18.1.1.

If the body is solid, the no-slip condition at the wall gives $\mathbf{u} = U_0\mathbf{e}_\imath$. Thus (18.1.86) can be written as

$$\int_A U_0\mathbf{e}_\imath\cdot\mathbf{T}\cdot\mathbf{n}\, \mathrm{d}A = \mathcal{D}_{BL} + \mathcal{D}_P \qquad \Rightarrow \qquad U_0(-D) = \mathcal{D}_{BL} + \mathcal{D}_P. \tag{18.1.89}$$

The boundary layer near a solid wall is usually strong and accounts for the major part of the total dissipation. However, $\mathcal{D}_P$ is not zero and does contribute to the drag. We call $\mathcal{D}_P/U_0$ an additional drag and it is computed for an airfoil in Section 18.1.3. The dissipation of the outer potential flow increases the drag calculated from the boundary layer flow alone. Our calculation shows that the coefficient of the additional drag is proportional to $1/R_e$. Thus the additional drag is small when the Reynolds number is high.

The situation is different for a rotating cylinder moving in a liquid. The no-slip condition at the wall gives $\mathbf{u} = U_0\mathbf{e}_\imath + \Omega a\mathbf{e}_\theta$, where Ω is the angular speed of the cylinder. Equation (18.1.86) can be written as

$$\begin{aligned}\int_A (U_0\mathbf{e}_\imath + \Omega a\mathbf{e}_\theta)\cdot\mathbf{T}\cdot\mathbf{n}\, \mathrm{d}A &= U_0\int_A \mathbf{e}_\imath\cdot\mathbf{T}\cdot\mathbf{n}\, \mathrm{d}A + \Omega\int_A a\tau_{\theta n}\, \mathrm{d}A,\\ \Rightarrow \qquad U_0(-D) + \Omega T &= \mathcal{D}.\end{aligned} \tag{18.1.90}$$

Equation (18.1.90) is not enough to determine two unknowns, the drag D and the torque T. Thus the dissipation method alone cannot give the drag or the torque in this case.

Padrino and Joseph (2006) numerically simulated the flow past a rapidly rotating cylinder. When the Reynolds number is R_e=400 and the ratio between the cylinder rotating speed and the streaming flow speed q/U_0=4, they obtained $\mathcal{D}_{BL}$:$\mathcal{D}_P$=1.72:1. Although in this case the dissipation cannot be used to compute the drag or the torque independently, the data show that the viscous dissipation of the outer potential flow can be significant.

We extend the idea of the viscous pressure correction from gas-liquid flows to Prandtl's boundary layer outside a solid. At the outer edge of the boundary layer, the shear stress evaluated on the boundary layer solution using Prandtl's theory does not necessarily equal the shear stress evaluated on the outside potential flow; this is analogous to the discrepancy between the zero shear stress and non-zero irrotational shear stress at a gas-liquid interface. The shear stress discrepancy at the outer edge of the boundary layer induces extra vorticity and a viscous pressure correction. The power of the pressure correction is equal to the power of this shear stress discrepancy.

We apply the method of VCVPF to the boundary layer around a rapidly rotating cylinder in a uniform flow in Section 18.1.2. The pressure correction is expanded as a Fourier series and we determine the coefficient for the cosθ term, which is the only term in the Fourier series contributing to the drag. We integrate the pressure correction and viscous stresses to obtain the additional drag at the outer edge of the boundary layer, which is not obtained by the dissipation calculation for this problem. Numerical simulations confirm that the pressure in the region near the cylinder surface gives rise to a noticeable drag. After choosing an effective boundary layer thickness, we are able to fit the pressure drag computed from VCVPF theory to the pressure drag from numerical simulation. We note that this pressure drag at the outer edge of the boundary layer is different from the pressure drag on the cylinder. Actually, the simulations show that the pressure drag changes sign across the boundary layer. The method of VCVPF can only determine the pressure correction at the outer edge of the boundary layer, not the variation inside the boundary layer. A boundary layer analysis for the flow past a rapidly rotating cylinder will be presented in the next section, in which the pressure inside the boundary layer is solved.

18.2 Glauert's solution of the boundary layer on a rapidly rotating clylinder in a uniform stream revisited

We perform a boundary layer analysis for the streaming flow past a rapidly rotating circular cylinder (figure 18.4) †. The starting point is the full continuity and momentum equations without any approximations. We assume that the solution is a boundary layer flow near the cylinder surface with the potential flow outside the boundary layer. The order of magnitude of the terms in the continuity and momentum equations can be estimated inside the boundary layer. When terms in the order of δ/a and higher are dropped, where δ is the boundary layer thickness and a is the radius of the cylinder, the equations used by Glauert (1957) are recovered. Glauert's solution ignores the irrotational rotary component of the flow inside the boundary layer, which is consistent with dropping δ/a terms in the governing equations.

We propose a new solution to this problem, in which the velocity field is decomposed into two parts. Outside the boundary layer, the flow is irrotational and can be decomposed into a purely rotary flow and a potential flow past a fixed cylinder. Inside the boundary layer, the velocity is decomposed into an irrotational purely rotary flow and a boundary layer flow. Inserting this decomposition of the velocity field inside the boundary layer into the governing equations, we obtain a new set of equations for the boundary layer flow, in which we do not drop the terms in the order of δ/a or higher. The pressure can no longer be assumed to be a constant across the boundary layer, and the continuity of shear stress at the outer edge of the boundary layer is enforced. We solve this new set of equations using Glauert's method, i.e. to expand the solutions as a power series of $\alpha = 2U_0/Q$, where U_0 is the uniform stream velocity and Q is the circulatory velocity at the outer edge of the

† We call the readers' attention to the fact that in our problem, the uniform flow is from right to left and the cylinder rotates counter-clockwise (see figure 18.4). The lift on the cylinder points upward and is defined as positive. The drag on the cylinder is negative if it is in the uniform flow direction; the drag is positive if it is opposite to the uniform flow direction.

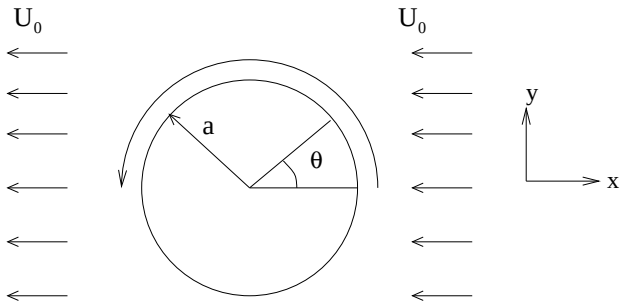

Fig. 18.4. The uniform streaming flow past a rotating cylinder.

boundary layer. The pressure from this boundary layer solution has two parts, an inertial part and a viscous part. The inertial part comes from the inertia terms in the momentum equations and is in agreement with the irrotational pressure; the viscous part comes from the viscous stress terms in the momentum equations and may be viewed as a viscous pressure correction, which contributes to both drag and lift. Our boundary layer solution is in reasonable to excellent agreement with the numerical simulation which will be presented in Section 18.3.

18.2.1 Introduction

The flow pattern depends critically on the ratio between the uniform stream velocity U_0 and the fluid circulatory velocity Q. Potential flow theory shows that when $2U_0/Q < 1$, there is no stagnation point on the cylinder and a region of closed streamlines exists near the cylinder. The fluid circulatory velocity Q is closely related to the peripheral velocity of the cylinder $q = \Omega a$, where Ω is the angular velocity of the cylinder; Q and q are approximately equal for large values of q. Experiments (Prandtl and Tietjens 1931) and simulations (Padrino and Joseph 2006) confirm that separation is largely suppressed and a closed boundary layer around the cylinder may be expected when q is much larger than U_0.

A number of theoretical studies have been dedicated to this problem based on the assumption that the ratio q/U_0 is high, separation is suppressed, and a steady state solution of the problem exists. Glauert (1957) solved the steady-state, two-dimensional boundary layer equations and obtained the solution in the form of a power series in $\alpha = 2U_0/Q$, which is related to the speed ratio q/U_0 by

$$\alpha \to 2U_0/q = \frac{2}{q/U_0} \quad \text{as} \quad q \to \infty. \tag{18.2.1}$$

He carried out the analysis up to and including boundary layer functions associated with α^4 and obtained

$$\frac{Q}{q} = 1 - 3\left(\frac{U_0}{q}\right)^2 - 3.24\left(\frac{U_0}{q}\right)^4 + \dots. \tag{18.2.2}$$

In his boundary layer equations, the pressure was assumed to be a constant across the boundary layer; thus the irrotational pressure is the only component in the normal stress acting on the cylinder. The pressure does not contribute to the drag and its contribution to the lift is the same as in the classical aerodynamics equation $L_p = \rho U_0 \Gamma$, where $\Gamma = 2\pi a Q$ is the circulation. The coefficient for the pressure lift is

$$C_{L_p} = \frac{L_p}{\rho U_0^2 a} = 2\pi\frac{Q}{U_0} = 2\pi\frac{q}{U_0}\left[1 - 3\left(\frac{U_0}{q}\right)^2 - 3.24\left(\frac{U_0}{q}\right)^4 + \dots\right]. \tag{18.2.3}$$

The effect of the boundary layer analysis on the pressure lift is through the value of Q and it should be noted that C_{L_p} is independent of the Reynolds number. Glauert did not consider the friction drag and lift, but they can be readily obtained from his solution:

$$C_{D_f} = \frac{D_f}{\rho U_0^2 a} = -\frac{2\pi}{\sqrt{R_e}}\sqrt{\frac{Q}{U_0}}, \qquad C_{L_f} = \frac{L_f}{\rho U_0^2 a} = \frac{2\pi}{\sqrt{R_e}}\sqrt{\frac{Q}{U_0}}, \tag{18.2.4}$$

where

$$R_e = \frac{2a\rho U_0}{\mu} \tag{18.2.5}$$

is the Reynolds number based on the uniform streaming velocity. Glauert computed the torque needed to maintain the rotation

$$T = 2\sqrt{2}\pi\rho U_0^{\frac{3}{2}} a^{\frac{3}{2}}\sqrt{\nu}\left[\left(\frac{U_0}{q}\right)^{\frac{1}{2}} - 0.522\left(\frac{U_0}{q}\right)^{\frac{5}{2}} + \ldots\right] \tag{18.2.6}$$

and the torque coefficient is

$$C_T = \frac{T}{2\rho U_0^2 a^2} = \frac{2\pi}{\sqrt{R_e}}\left[\left(\frac{U_0}{q}\right)^{\frac{1}{2}} - 0.522\left(\frac{U_0}{q}\right)^{\frac{5}{2}} + \ldots\right]. \tag{18.2.7}$$

Wood (1957) studied a class of two-dimensional, laminar boundary layer flows with closed streamlines. The velocity at the solid boundary was supposed uniform, and the velocity in the boundary layer was supposed to differ only slightly from that of the boundary. A formal solution of the boundary layer was then derived by expanding the velocity in a power series in a small parameter representative of the small differences of the speed through the boundary layer. He applied the theory to the uniform streaming flow past a rotating cylinder and obtained a circulation which was equivalent to the first two terms of equation (18.2.2).

Moore (1957) also considered this problem assuming that the cylinder rotation velocity was much greater than that of the uniform stream. He argued that the effect of the uniform streaming flow could be regarded as a perturbation of the viscous irrotational rotary flow induced by a rotating cylinder and obtained a uniformly valid first approximation to the flow field by solving the stream function equation. In the limit of large Reynolds number, Moore also obtained a circulation which was equivalent to the first two terms of equation (18.2.2). Moore showed that the drag was small, in the order of $(U_0/q)^3$ and the lift coefficient was

$$C_L = 2\pi\frac{q}{U_0}\left[1 + O\left(\frac{U_0}{q}\right)^2\right], \tag{18.2.8}$$

which is comparable to Glauert's pressure lift (18.2.3), but Moore did not give the coefficient of $(U_0/q)^2$. In the limit of large Reynolds number, Moore showed that the torque was

$$T = 4\pi\mu aq\left(1 + \frac{\sqrt{2}}{2}\left(\frac{U_0}{q}\right)^2\sqrt{R_e}\right), \tag{18.2.9}$$

where the first term on the right hand side $4\pi\mu aq$ is the torque when there is only viscous irrotational rotary flow but no streaming flow. The torque coefficient is

$$C_T = \frac{4\pi}{R_e}\frac{q}{U_0} + \frac{2\sqrt{2}\pi}{\sqrt{R_e}}\frac{U_0}{q}, \tag{18.2.10}$$

where the second term on the right hand side is similar to Glauert's torque coefficient (18.2.7), but the powers of U_0/q are different.

Numerical simulations have been widely used to study the flow past a rotating cylinder. A review of the numerical studies can be found in Section 18.3. The numerical results in Section 18.3 show that separation is largely suppressed and a steady state solution can be obtained. The numerical simulation will serve as the benchmark for the analysis in this work.

We investigate the uniform streaming flow past a rotating cylinder adopting the same assumption as in Glauert (1957), Moore (1957), and Wood (1957), i.e. the cylinder rotation velocity is much greater than that of the uniform stream, separation is suppressed, and a steady state solution of the problem exists. Our work here is intended to be an improvement of Glauert's boundary layer solution. The boundary layer equations used by Glauert can be recovered when terms in the order of δ/a and higher are dropped from the unapproximated continuity and momentum equations. To be consistent, one should have

$$Q\frac{a+\delta}{r} \sim Q, \quad \text{for} \quad a \le r \le a+\delta,$$

which means that the irrotational rotary component of the flow inside the boundary layer is ignored. The tangential velocity given by Glauert is

$$u = Q\left(1 + \alpha f_1^{'} \mathrm{e}^{\imath\theta} + \alpha^2\left[f_2^{'}\mathrm{e}^{2\imath\theta} + g_2^{'}\right] + \ldots\right), \tag{18.2.11}$$

which is a perturbation about a uniform flow, not a perturbation about the viscous irrotational rotary flow. It can be inferred from (18.2.11) that the shear stress at the cylinder surface approaches zero when α approaches zero. In other words, Glauert's solution suggests that the shear stress at the cylinder surface approaches zero when the streaming flow is extremely weak compared to the rotation of the cylinder. However, the real limiting value for the shear stress is $-2\mu q/a$. This discrepancy carries on to the computation of the torque. Glauert's torque expression (18.2.6) indicates that the torque is zero when $U_0 = 0$, however, the actual torque to maintain the rotation of the cylinder in a viscous irrotational purely rotary flow is $4\pi\mu aq$, which is also shown in Moore's torque expression (18.2.9).

We propose a new solution to this problem, in which the velocity is decomposed into two parts. Outside the boundary layer, the flow is irrotational and can be decomposed into a viscous irrotational purely rotary flow and a potential flow past a fixed cylinder. Inside the boundary layer, the velocity field is decomposed into a viscous irrotational purely rotary flow and a boundary layer flow which is expanded as a power series of $\alpha = 2U_0/Q$. This decomposition of the velocity field in the boundary layer is actually a perturbation of the purely rotary flow with α being the perturbation parameter, which is similar to Moore's approach. The difference is that Moore tried to obtain a uniformly valid solution for the flow, whereas we are seeking the solution valid in the boundary layer. Inserting this decomposition of the velocity field inside the boundary layer into the governing equations, we obtain a new set of equations for the boundary layer flow, in which we do not drop the terms in the order of δ/a or higher. There are significant differences between our new equations and Glauert's boundary layer equations. In Glauert's study the pressure is assumed to be a constant across the boundary layer and the momentum equation in the radial direction is not used. The direct result of this approximation by Glauert (and Prandtl), is that the normal stress on a solid is imposed by the irrotational pressure, independent of the Reynolds number. Viscous effects on the normal stress on a solid wall, which always exist at finite-Reynolds number, no matter how large, are not available. In our new equations, the pressure is an unknown and the momentum equation in the radial direction does appear. Because we have an extra unknown, an extra boundary condition is needed and we choose to enforce the continuity of the shear stress at the outer edge of the boundary layer. The technique to solve this new set of equations is almost the same as that used by Glauert. The power series expansions are inserted into the new set of equations and the coefficients of different powers of α are compared, then ordinary differential equations for the functions in the power series are obtained and solved. The inertia terms in the momentum equations give rise to the irrotational pressure and the viscous terms lead to a viscous pressure correction, which contributes to both drag and lift.

One of the key differences between our new boundary layer analysis and the classical boundary layer theory of Prandtl is about the calculation of the pressure drag. In the classical boundary layer approximation, the pressure is constant across the layer and the irrotational pressure of the outer flow is imposed on the surface of the body. This approximation is not good enough for the purpose of the drag calculation and leads to zero pressure drag. Lighthill (1963) remarked "Errors, due to neglecting either the pressure gradient across the layer, or the displacement-thickness effect on U, produce a resultant pressure force ('form drag') comparable with the whole viscous force on the body ('skin-friction drag'). Accordingly, such errors cannot be neglected, as often no drag is present from other causes, the pressure forces in pure irrotational flow having zero resultant." Various techniques were developed to calculate the pressure drag as a patch for Prandtl's theory. Lighthill (1963) described these methods "To get round these difficulties, one does not in practice attempt to calculate surface pressure more precisely, but uses a combination of arguments (Chapter X) in which drag is inferred, from conservation of momentum for large masses of fluid, in terms of the state of the boundary layer at the trailing edge." Schlichting (1960) reviewed methods for the calculation of the profile drag (the sum of the friction drag and the pressure drag) devised by Pretsch (1938) and Squire and Young (1938). These methods are tied in with the boundary layer calculation and the drag is obtained based on the principle of momentum conservation. Schlichting remarked about these methods "However, in order to be in a position to calculate pressure drag it is necessary in each case to make use of certain additional empirical relations." The method by which we treat the drag is totally different. We solve for the pressure on the body from governing equations. The pressure drag

is computed by direct integration of the pressure over the surface of the body, not by arguments of conservation of the momentum.

In our new set of equations for the boundary layer flow and its boundary conditions, we assume that the boundary layer thickness δ/a is known, then we can compute the solution. This is different from the problems such as the Blasius's solution, in which the boundary condition at the outer edge of the boundary layer can be stretched to infinity and the solution is obtained without knowledge of the boundary layer thickness. We prescribe δ/a at different values, compute the solution, then compare them to the results of numerical simulation; the value of δ/a which leads to the best agreement with the simulation results may be viewed as a proper boundary layer thickness. The boundary layer thickness determined in this way satisfies approximately $(\delta/a) \propto (1/\sqrt{R_e})$ and decreases with increasing q/U_0. Comparison of our solution using the proper δ/a with the simulation results and Glauert's and Moore's solutions shows that our lift and torque are in reasonable to excellent agreement with the simulation results and the agreement for the drag is less good if the speed ratio q/U_0 is not high enough. It is also demonstrated our solution is indeed an improvement of Glauert's solution.

18.2.2 Unapproximated governing equations

Using the polar coordinate system $(r,\, \theta)$, the continuity equation is

$$\frac{\partial v_r}{\partial r} + \frac{v_r}{r} + \frac{1}{r}\frac{\partial v_\theta}{\partial \theta} = 0, \tag{18.2.12}$$

and the momentum equations for steady flows are

$$\left(v_r \frac{\partial}{\partial r} + \frac{v_\theta}{r}\frac{\partial}{\partial \theta}\right) v_\theta + \frac{v_r v_\theta}{r} = -\frac{1}{r\rho}\frac{\partial \mathrm{P}}{\partial \theta} + \nu\left(\nabla^2 v_\theta - \frac{v_\theta}{r^2} + \frac{2}{r^2}\frac{\partial v_r}{\partial \theta}\right); \tag{18.2.13}$$

$$\left(v_r \frac{\partial}{\partial r} + \frac{v_\theta}{r}\frac{\partial}{\partial \theta}\right) v_r - \frac{v_\theta^2}{r} = -\frac{1}{\rho}\frac{\partial \mathrm{P}}{\partial r} + \nu\left(\nabla^2 v_r - \frac{v_r}{r^2} - \frac{2}{r^2}\frac{\partial v_\theta}{\partial \theta}\right), \tag{18.2.14}$$

where

$$\nabla^2 = \frac{\partial^2}{\partial r^2} + \frac{1}{r}\frac{\partial}{\partial r} + \frac{1}{r^2}\frac{\partial^2}{\partial \theta^2}.$$

18.2.3 Boundary layer approximation and Glauert's equations

The flow may be approximated by a boundary layer near the cylinder surface and a potential flow outside. Inside the boundary layer, we have the following estimations

$$v_\theta \sim Q, \quad r \sim a, \quad \frac{\partial}{\partial r} \sim \frac{1}{\delta}, \quad \frac{\partial}{\partial \theta} \sim 1. \tag{18.2.15}$$

With these estimates, the magnitude of the terms in (18.2.12) can be written as

$$\frac{v_r}{\delta} + \frac{v_r}{a} + \frac{Q}{a} = 0.$$

If we consider v_r/a to be negligible compared to v_r/δ, we have

$$\frac{v_r}{\delta} + \frac{Q}{a} = 0 \quad \Rightarrow \quad v_r \sim Q\frac{\delta}{a}, \tag{18.2.16}$$

and the continuity equation may be written as

$$\frac{\partial v_r}{\partial r} + \frac{1}{r}\frac{\partial v_\theta}{\partial \theta} = 0. \tag{18.2.17}$$

We estimate the magnitude of terms in equation (18.2.13):

$$\frac{Q^2}{a}\left(1 + 1 + \frac{\delta}{a}\right) = -\frac{1}{r\rho}\frac{\partial \mathrm{P}}{\partial \theta} + \nu\frac{Q}{\delta^2}\left(1 + \frac{\delta}{a} + \frac{\delta^2}{a^2} - \frac{\delta^2}{a^2} + \frac{\delta^3}{a^3}\right). \tag{18.2.18}$$

If we drop the terms of the order of δ/a and higher, equation (18.2.13) becomes

$$v_r\frac{\partial v_\theta}{\partial r}+\frac{v_\theta}{r}\frac{\partial v_\theta}{\partial \theta}=-\frac{1}{r\rho}\frac{\partial \mathrm{P}}{\partial \theta}+\nu\frac{\partial^2 v_\theta}{\partial r^2}. \tag{18.2.19}$$

Now we estimate the magnitude of terms in (18.2.14):

$$\frac{Q^2}{a}\left(\frac{\delta}{a}+\frac{\delta}{a}-1\right)=-\frac{1}{\rho}\frac{\partial \mathrm{P}}{\partial r}+\nu\frac{Q}{\delta^2}\left(\frac{\delta}{a}+\frac{\delta^2}{a^2}+\frac{\delta^3}{a^3}-\frac{\delta^3}{a^3}+\frac{\delta^2}{a^2}\right). \tag{18.2.20}$$

Thus (18.2.14) becomes

$$\frac{v_\theta^2}{r}=\frac{1}{\rho}\frac{\partial \mathrm{P}}{\partial r}, \tag{18.2.21}$$

which indicates that the change of the pressure across the boundary layer is on the order of δ and the pressure can still be assumed to be constant if δ/a is negligible (Schlichting 1960).

Now if we use x for $r\theta$, y for r, u for v_θ and v for v_r, equations (18.2.17) and (18.2.19) may be written as

$$\frac{\partial u}{\partial x}+\frac{\partial v}{\partial y}=0, \tag{18.2.22}$$

$$u\frac{\partial u}{\partial x}+v\frac{\partial u}{\partial y}=-\frac{1}{\rho}\frac{\partial \mathrm{P}}{\partial x}+\nu\frac{\partial^2 u}{\partial y^2}, \tag{18.2.23}$$

which are the two-dimensional boundary layer equations used by Glauert (1957). If δ/a terms are dropped, the irrotational rotary component of the velocity inside the boundary layer will be ignored. In reality, the boundary layer thickness is never zero and is found to be rather large in numerical simulations. Therefore, dropping δ/a terms can cause substantial error.

18.2.4 Decomposition of the velocity and pressure field

We propose a new solution, in which the total velocity and pressure are decomposed into two parts

$$v_\theta=u_{p\theta}+u_\theta,\quad v_r=u_r,\quad \mathrm{P}=p_p+p \tag{18.2.24}$$

where

$$u_{p\theta}=Q\frac{a+\delta}{r},\quad \text{and}\quad p_p=p_\infty-\frac{\rho}{2}\frac{(a+\delta)^2}{r^2}Q^2 \tag{18.2.25}$$

are the irrotational purely rotary velocity and the pressure induced by rotation. It is noted that $v_\theta=u_{p\theta}$, $v_r=0$ and $\mathrm{P}=p_p$ is a potential solution and is an exact solution for the unapproximated governing equations and no-slip boundary condition.

Outside the boundary layer, the flow is irrotational and can be decomposed into two potential flows: the irrotational purely rotary flow and the uniform flow past a circle with the radius $a+\delta$. The velocity from the second potential flow is

$$u_\theta=U_0\left[1+\frac{(a+\delta)^2}{r^2}\right]\sin\theta,\quad u_r=-U_0\left[1-\frac{(a+\delta)^2}{r^2}\right]\cos\theta. \tag{18.2.26}$$

At the outer edge of the boundary layer ($r=a+\delta$), the tangential velocity is

$$v_\theta=2U_0\sin\theta+Q. \tag{18.2.27}$$

The total pressure at $r=a+\delta$ can be obtained from Bernoulli's equation

$$\mathrm{P}=p_\infty^{'}+\frac{\rho}{2}U_0^2\left(1-4\sin^2\theta\right)-2\rho U_0 Q\sin\theta-\frac{\rho}{2}Q^2. \tag{18.2.28}$$

After subtracting p_p from (18.2.28), we obtain the pressure p at $r=a+\delta$

$$p=c+\frac{\rho}{2}U_0^2\left(1-4\sin^2\theta\right)-2\rho U_0 Q\sin\theta=c-\frac{\rho}{2}U_0^2+\rho U_0^2\cos 2\theta-2\rho U_0 Q\sin\theta, \tag{18.2.29}$$

where c is a certain constant.

Inside the boundary layer, u_θ, u_r and p need to be obtained from the governing equations. We insert (18.2.24) into the governing equations (18.2.12), (18.2.13) and (18.2.14), subtract the equations satisfied by $u_{p\theta}$ and p_p, and obtain

$$\frac{\partial u_r}{\partial r} + \frac{u_r}{r} + \frac{1}{r}\frac{\partial u_\theta}{\partial \theta} = 0, \tag{18.2.30}$$

$$u_r \frac{\partial}{\partial r}\left(u_{p\theta} + u_\theta\right) + \frac{u_{p\theta} + u_\theta}{r}\frac{\partial u_\theta}{\partial \theta} + \frac{u_r(u_{p\theta} + u_\theta)}{r} = -\frac{1}{r\rho}\frac{\partial p}{\partial \theta} + \nu\left(\frac{\partial^2 u_\theta}{\partial r^2} + \frac{1}{r}\frac{\partial u_\theta}{\partial r} + \frac{1}{r^2}\frac{\partial^2 u_\theta}{\partial \theta^2} - \frac{u_\theta}{r^2} + \frac{2}{r^2}\frac{\partial u_r}{\partial \theta}\right), \tag{18.2.31}$$

$$u_r \frac{\partial u_r}{\partial r} + \frac{u_{p\theta} + u_\theta}{r}\frac{\partial u_r}{\partial \theta} - \frac{2u_{p\theta}u_\theta + u_\theta^2}{r} = -\frac{1}{\rho}\frac{\partial p}{\partial r} + \nu\left(\frac{\partial^2 u_r}{\partial r^2} + \frac{1}{r}\frac{\partial u_r}{\partial r} + \frac{1}{r^2}\frac{\partial^2 u_r}{\partial \theta^2} - \frac{u_r}{r^2} - \frac{2}{r^2}\frac{\partial u_\theta}{\partial \theta}\right). \tag{18.2.32}$$

18.2.5 Solution of the boundary layer flow

We solve equations (18.2.30), (18.2.31) and (18.2.32) for u_θ, u_r and p. Three boundary conditions are imposed on the velocities, u_θ, u_r at $r = a$ and u_θ at $r = a + \delta$; these are the same as in Glauert's analysis. The fourth boundary condition is that the shear stress $\tau_{r\theta}^{BL}$ evaluated using the boundary layer solution is equal to the shear stress $\tau_{r\theta}^{I}$ evaluated using the outer irrotational flow at $r = a + \delta$. The four boundary conditions are listed as follows

$$Q\frac{a+\delta}{a} + u_\theta = q \quad \text{at} \quad r = a; \tag{18.2.33}$$

$$u_r = 0 \quad \text{at} \quad r = a; \tag{18.2.34}$$

$$Q + u_\theta = Q + 2U_0 \sin\theta \quad \text{at} \quad r = a + \delta; \tag{18.2.35}$$

$$\tau_{r\theta}^{BL} = \tau_{r\theta}^{I} \quad \text{at} \quad r = a + \delta. \tag{18.2.36}$$

Because we are considering one single fluid, the viscosity is the same inside and outside the boundary layer. The continuity of the shear stress (18.2.36) is equivalent to continuity of velocity gradients. Glauert's boundary layer equations can only give solutions with continuous velocity, but our new equations can give solutions with continuous velocity and velocity gradients. We will use complex variables to solve the equations and (18.2.35) is written as

$$u_\theta = Q\alpha(-\imath)\mathrm{e}^{\imath\theta} \quad \text{at} \quad r = a + \delta. \tag{18.2.37}$$

Note that only the real part of the equation has physical significance.

We follow Glauert and expand the solution as a power series of α. A stream function can be written as

$$\psi = Q\left[\alpha f_1(r)\mathrm{e}^{\imath\theta} + \alpha^2\left(f_2(r)\mathrm{e}^{2\imath\theta} + g_2(r)\right)\ldots\right] \tag{18.2.38}$$

and the velocities are

$$u_\theta = \frac{\partial \psi}{\partial r} = Q\left[\alpha f_1'(r)\mathrm{e}^{\imath\theta} + \alpha^2\left(f_2'(r)\mathrm{e}^{2\imath\theta} + g_2'(r)\right)\ldots\right], \tag{18.2.39}$$

$$u_r = -\frac{1}{r}\frac{\partial \psi}{\partial \theta} = -\frac{Q}{r}\left[\alpha\imath f_1(r)\mathrm{e}^{\imath\theta} + \alpha^2 2\imath f_2(r)\mathrm{e}^{2\imath\theta} + \ldots\right]. \tag{18.2.40}$$

The continuity equation (18.2.30) is automatically satisfied. The pressure is assumed to be

$$p = p_c + \rho Q^2\left[\alpha s_1(r)\mathrm{e}^{\imath\theta} + \alpha^2\left(s_2(r)\mathrm{e}^{2\imath\theta} + t_2(r)\right)\ldots\right], \tag{18.2.41}$$

where p_c is a constant.

We evaluate $\tau_{r\theta}^{I}$ using the potential flow (18.2.26) and the irrotational rotary flow

$$\tau_{r\theta}^{I} = -\frac{2\mu Q}{a+\delta} + \mu Q\alpha \frac{2\imath}{a+\delta} \mathrm{e}^{\imath\theta}. \tag{18.2.42}$$

From the boundary layer solutions, we obtain

$$\begin{aligned}\tau_{r\theta}^{BL} = &-\frac{2\mu Q}{a+\delta} + \mu Q\alpha \left[f_1^{''} - \frac{f_1^{'}}{a+\delta} + \frac{f_1}{(a+\delta)^2} \right] \mathrm{e}^{\imath\theta} \\ &+ \mu Q\alpha^2 \left[\left(f_2^{''} \mathrm{e}^{2\imath\theta} + g_2^{''} \right) - \frac{1}{a+\delta} \left(f_2^{'} \mathrm{e}^{2\imath\theta} + g_2^{'} \right) + \frac{4}{(a+\delta)^2} f_2 \mathrm{e}^{2\imath\theta} \right] + \ldots . \end{aligned} \tag{18.2.43}$$

Comparing the terms in (18.2.42) and (18.2.43) linear in α, we obtain

$$\frac{2\imath}{a+\delta} = f_1^{''} - \frac{f_1^{'}}{a+\delta} + \frac{f_1}{(a+\delta)^2} \quad \text{at} \quad r = a+\delta. \tag{18.2.44}$$

Consideration of the terms quadratic in α gives

$$f_2^{''} - \frac{1}{a+\delta} f_2^{'} + \frac{4}{(a+\delta)^2} f_2 = 0 \quad \text{and} \quad g_2^{''} - \frac{1}{a+\delta} g_2^{'} = 0 \quad \text{at} \quad r = a+\delta. \tag{18.2.45}$$

In this study, one of the major objects is to determine the relation between the cylinder velocity q and the fluid circulatory velocity Q. In the expansion of the boundary layer velocities (18.2.39) and (18.2.40), Q is used as the fundamental parameter rather than q. As noted by Glauert, this approach is convenient for the study of the boundary layer equations because the velocity at the outer edge of the boundary layer is completely specified. Though Q is an unknown quantity and q is prescribed, the relationship between q and Q can be established via (18.2.33), giving Q in terms of q. We also note that the boundary layer thickness δ appears in the boundary conditions and it must be prescribed to obtain the solution. It can be expected that the boundary layer thickness is a function of θ, but we are not able to determine the shape of the boundary layer. We will assume that δ is a constant for given R_e and q/U_0; it may be viewed as the average boundary layer thickness. The choice of δ has significant effects on the solution and will be discussed later.

We insert (18.2.39), (18.2.40) and (18.2.41) into (18.2.31) and (18.2.32) and compare the coefficients of different powers of α, to obtain ordinary differential equations for $f_1(r)$, $f_2(r)$, $g_2(r)$ ... The terms linear in α in (18.2.31) and (18.2.32) satisfy respectively

$$\frac{Q(a+\delta)}{r} f_1^{'} = -Q s_1 + \frac{\nu}{\imath} \left(r f_1^{'''} + f_1^{''} - \frac{2 f_1^{'}}{r} + \frac{2 f_1}{r^2} \right), \tag{18.2.46}$$

$$\frac{Q(a+\delta)}{r^3} f_1 - \frac{2Q(a+\delta)}{r^2} f_1^{'} = -Q s_1^{'} + \frac{\nu}{\imath} \left(\frac{f_1^{''}}{r} + \frac{1}{r^2} f_1^{'} - \frac{1}{r^3} f_1 \right). \tag{18.2.47}$$

After eliminating s_1 from (18.2.46) and (18.2.47), we obtain a fourth order ordinary differential equation for f_1

$$\frac{Q(a+\delta)}{\nu} \imath \left(\frac{f_1^{''}}{r} + \frac{f_1^{'}}{r^2} - \frac{f_1}{r^3} \right) = r f_1^{''''} + 2 f_1^{'''} - \frac{3}{r} f_1^{''} + \frac{3}{r^2} f_1^{'} - \frac{3}{r^3} f_1, \tag{18.2.48}$$

where $Q(a+\delta)/\nu$ is a Reynolds number and we write

$$k = \frac{\nu}{Q(a+\delta)}. \tag{18.2.49}$$

The solution of (18.2.48) is

$$f_1(r) = \frac{c_1}{r} + c_2 r^{2-\beta} + c_3 r^{2+\beta} + c_4 r, \tag{18.2.50}$$

where c_1, c_2, c_3 and c_4 are constants to be determined by boundary conditions and

$$\beta = \sqrt{1 + \frac{\imath}{k}}. \tag{18.2.51}$$

Three boundary conditions for f_1 are obtained from (18.2.33), (18.2.34) and (18.2.37)

$$f_1(a) = 0, \quad f_1^{'}(a) = 0, \quad f_1^{'}(a+\delta) = -\imath. \tag{18.2.52}$$

The fourth condition is the continuity of the shear stress (18.2.44), which can be written as

$$\frac{\imath}{a+\delta} = f_1^{''} + \frac{f_1}{(a+\delta)^2} \quad \text{at} \quad r = a+\delta. \tag{18.2.53}$$

With these four boundary conditions, we can determine c_1, c_2, c_3 and c_4 and the function f_1. The expression for f_1 is long and will not be shown here.

After we obtain $f_1(r)$, we can compute $s_1(r)$ using equation (18.2.46)

$$s_1 = -\frac{a+\delta}{r} f_1^{'} + \frac{\nu}{Q}\zeta, \tag{18.2.54}$$

where

$$\zeta = \frac{1}{\imath}\left(r f_1^{'''} + f_1^{''} - \frac{2}{r} f_1^{'} + \frac{2}{r^2} f_1 \right). \tag{18.2.55}$$

The two parts of s_1, $\left(-\frac{a+\delta}{r} f_1^{'}\right)$ and $\frac{\nu}{Q}\zeta$ come from the inertia term and viscous stress term in the momentum equation, respectively.

Next we carry out the calculation for terms quadratic in α. As pointed out by Glauert, care should be taken when computing product of two complex numbers A and B,

$$\text{Real}(A)\text{Real}(B) = \text{Real}(A(B+\overline{B})/2), \tag{18.2.56}$$

where the overbar denotes a complex conjugate. We collect terms quadratic in α from (18.2.31) and they can be divided into two groups, terms proportional to $\mathrm{e}^{2\imath\theta}$ and terms independent of θ. The two groups of terms satisfy the following equations, respectively

$$\frac{1}{r}\frac{Q\imath}{\nu}\left(\frac{1}{2} f_1^{'2} - \frac{1}{2} f_1 f_1{}'' - \frac{1}{2r} f_1 f_1^{'} + \frac{2(a+\delta)}{r} f_2^{'} \right) = -\frac{Q\imath}{\nu}\frac{2 s_2}{r} + \left(f_2^{'''} + \frac{f_2^{''}}{r} - \frac{5 f_2^{'}}{r^2} + \frac{8 f_2}{r^3} \right), \tag{18.2.57}$$

$$-\frac{1}{2r}\frac{Q\imath}{\nu}\left(f_1 \overline{f_1^{'''}} + f_1^{'}\overline{f_1^{''}} + \frac{f_1}{r}\overline{f_1^{''}} \right) = g_2^{'''} + \frac{g_2^{''}}{r} - \frac{g_2^{'}}{r^2}. \tag{18.2.58}$$

Consideration of terms in (18.2.32) quadratic in α also yields two equations

$$\frac{1}{r}\frac{Q\imath}{\nu}\left(\frac{1}{2r^2} f_1^2 - \frac{1}{2} f_1^{'2} + \frac{4(a+\delta)}{r^2} f_2 - \frac{2(a+\delta)}{r} f_2^{'} \right) = -\frac{Q\imath}{\nu} s_2^{'} - \left(\frac{8}{r^3} f_2 - \frac{2}{r^2} f_2^{'} - \frac{2}{r} f_2^{''} \right), \tag{18.2.59}$$

$$\frac{1}{r}\left(\frac{1}{2r} f_1 \overline{f_1^{'}} + \frac{1}{2r} f_1^{'}\overline{f_1} - \frac{1}{2r^2} f_1 \overline{f_1} - \frac{1}{2} f_1^{'}\overline{f_1^{'}} - \frac{2(a+\delta)}{r} g_2^{'} \right) = -t_2^{'}. \tag{18.2.60}$$

We can first solve $g_2(r)$ from (18.2.58), then eliminate $s_2(r)$ from (18.2.57) and (18.2.59) and solve for $f_2(r)$, finally obtain $t_2(r)$ from (18.2.60).

Equation (18.2.58) is a third order ordinary differential equation for g_2. We prescribe the stream function at $r = a$ to be zero, which gives the condition

$$g_2(a) = 0. \tag{18.2.61}$$

The boundary condition (18.2.37) leads to

$$g_2^{'}(a+\delta) = 0. \tag{18.2.62}$$

The continuity of the shear stress (18.2.45) leads to

$$g_2^{''}(a+\delta) = 0. \tag{18.2.63}$$

No condition can be applied to $g_2^{'}(r{=}a)$, because it is only known that the surface velocity is independent of θ. Thus we have three boundary conditions (18.2.61), (18.2.62) and (18.2.63) for the third order ordinary

differential equation (18.2.58). Closed-form solution for $g_2(r)$ can be obtained, but it is long and tedious and will not be shown here.

We eliminate s_2 from (18.2.57) and (18.2.59) and obtain a fourth order ordinary differential equation for f_2

$$\frac{Q\imath}{\nu}\left(-\frac{1}{2}f_1f_1^{'''}+\frac{1}{2}f_1^{'}f_1^{''}-\frac{1}{2r}f_1f_1^{''}+\frac{1}{2r}f_1^{'}f_1^{'}+\frac{1}{2r^2}f_1f_1^{'}-\frac{1}{r^3}f_1^2\right)=$$
$$rf_2^{''''}+2f_2^{'''}-\frac{9}{r}f_2^{''}+\frac{9}{r^2}f_2^{'}-\frac{Q(a+\delta)\imath}{\nu}\left(\frac{2}{r}f_2^{''}+\frac{2}{r^2}f_2^{'}-\frac{8}{r^3}f_2\right). \tag{18.2.64}$$

Three boundary conditions for $f_2(r)$ are obtained from (18.2.33), (18.2.34) and (18.2.37)

$$f_2(a)=0,\quad f_2^{'}(a)=0,\quad f_2^{'}(a+\delta)=0, \tag{18.2.65}$$

and the fourth condition comes from the continuity of the shear stress (18.2.45)

$$f_2^{''}+\frac{4}{(a+\delta)^2}f_2=0\quad\text{at}\quad r=a+\delta. \tag{18.2.66}$$

Equation (18.2.64) and the boundary conditions are solved by numerical integration.

After $f_2(r)$ is obtained, we compute $s_2(r)$ using (18.2.57)

$$s_2=-\frac{1}{4}f_1^{'2}+\frac{1}{4}f_1f_1^{''}+\frac{1}{4r}f_1f_1^{'}-\frac{a+\delta}{r}f_2^{'}+\frac{\nu}{2Q}\xi, \tag{18.2.67}$$

where

$$\xi=\frac{1}{\imath}\left(rf_2^{'''}+f_2^{''}-\frac{5}{r}f_2^{'}+\frac{8}{r^2}f_2\right). \tag{18.2.68}$$

The function s_2 can be divided into two parts, the term $\frac{\nu}{2Q}\xi$ comes from the viscous stress and other terms in s_2 come from the inertia terms in the momentum equation.

The last step in the calculation of terms quadratic in α is to integrate (18.2.60) to obtain $t_2(r)$. There will be an undetermined constant in the process of integration, which can be absorbed into the pressure constant p_c.

With the functions s_1 and s_2, we can write the pressure as

$$\begin{aligned}p&=p_c+\rho Q^2\alpha s_1\mathrm{e}^{\imath\theta}+\rho Q^2\alpha^2\left(s_2\mathrm{e}^{2\imath\theta}+t_2\right)+O(\alpha^3)\\&=p_c+2\rho U_0Q\left(-\frac{a+\delta}{r}f_1^{'}+\frac{\nu}{Q}\zeta\right)\mathrm{e}^{\imath\theta}+\\&\quad 4\rho U_0^2\left[\left(-\frac{1}{4}f_1^{'2}+\frac{1}{4}f_1f_1^{''}+\frac{1}{4r}f_1f_1^{'}-\frac{a+\delta}{r}f_2^{'}+\frac{\nu}{2Q}\xi\right)\mathrm{e}^{2\imath\theta}+t_2\right]+O(\alpha^3).\end{aligned} \tag{18.2.69}$$

The pressure at the outer edge of the boundary layer is of interest, because it can be compared to the irrotational pressure (18.2.29) at $r=a+\delta$ and the difference between them gives the pressure correction. From (18.2.52) $f_1^{'}(a+\delta)=-\imath$ and (18.2.65) $f_2^{'}(a+\delta)=0$, the pressure at $r=a+\delta$ is

$$p=p_c+2\rho U_0Q\left(\imath+\frac{\nu}{Q}\zeta\right)\mathrm{e}^{\imath\theta}+\rho U_0^2\left[\left(1+f_1f_1^{''}-\frac{\imath}{a+\delta}f_1+\frac{2\nu}{Q}\xi\right)\mathrm{e}^{2\imath\theta}+4t_2\right]+O(\alpha^3). \tag{18.2.70}$$

The real part of the above equation is

$$\begin{aligned}p=&\mathrm{Real}(p_c)+4\rho U_0^2\mathrm{Real}(t_2)-2\rho U_0Q\sin\theta+\rho U_0^2\cos2\theta+\rho U_0^2\mathrm{Real}\left[\left(f_1f_1^{''}-\frac{\imath}{a+\delta}f_1\right)\mathrm{e}^{2\imath\theta}\right]\\&+2\mu U_0\left[\mathrm{Real}(\zeta)\cos\theta-\mathrm{Imag}(\zeta)\sin\theta\right]+2\mu\frac{U_0^2}{Q}\left[\mathrm{Real}(\xi)\cos2\theta-\mathrm{Imag}(\xi)\sin2\theta\right]+O(\alpha^3).\end{aligned} \tag{18.2.71}$$

Because the radial component u_r of the velocity is small in the boundary layer, we may neglect f_1, then compare (18.2.71) to the irrotational pressure (18.2.29). The terms $-2\rho U_0Q\sin\theta$ and $\rho U_0^2\cos2\theta$ are the same in the two pressure expressions, and the terms proportional to μ in (18.2.71) are the extra pressure arising in the boundary layer. This comparison demonstrates that the inertia terms in the momentum equations give rise to

the irrotational pressure and the viscous stress terms give rise to a viscous pressure correction. In general, the pressure correction can be expanded as a Fourier series

$$p_{\mathrm{v}} = \sum_{m=0}^{\infty} \left[h_m(r)\cos m\theta + j_m(r)\sin m\theta \right].$$

Here we determine the coefficients of $\sin\theta$, $\cos\theta$, $\sin 2\theta$ and $\cos 2\theta$ up to $O(\alpha^2)$ terms. These coefficients may be modified and more coefficients in the Fourier series can be obtained if calculations for $O(\alpha^3)$ terms are carried out. The $\cos\theta$ and $\sin\theta$ terms in the pressure correction contribute to the drag and lift, respectively.

Up to this point, our solutions are in terms of the fluid circulatory velocity Q. We shall solve for Q in terms of the prescribed quantities using an iterative method. There are two prescribed dimensionless parameters in this problem, the Reynolds number R_e and the speed ratio q/U_0. Our first guess of Q comes from the irrotational purely rotary flow

$$Q^{(1)} = q\frac{a}{a+\delta} \quad \Rightarrow \quad \frac{Q^{(1)}}{q} = \frac{1}{1+\delta/a},$$

where the superscript "(1)" indicates the value for Q in the first iteration. Using $Q^{(1)}/q$, the value of k is computed in equation (18.2.49) and $f_1(r)$ is subsequently obtained. Then we solve for $g_2(r)$ from equation (18.2.58) and obtain $g_2^{'}$. The velocity u_θ at $r = a$ is then

$$u_\theta = Q^{(1)}\alpha^2 \mathrm{Real}[g_2^{'}(r=a,\, Q^{(1)}/q)] + O(\alpha^3). \tag{18.2.72}$$

Inserting (18.2.72) into (18.2.33), we obtain

$$\frac{Q^{(2)}}{q}\frac{a+\delta}{a} + 4\frac{U_0^2}{q^2}\frac{q}{Q^{(1)}}\mathrm{Real}[g_2^{'}(r=a,\, Q^{(1)}/q)] = 1, \tag{18.2.73}$$

from which we can solve for $Q^{(2)}$, which is the value for Q in the second iteration. We repeat the calculation using $Q^{(2)}$ to obtain the value for Q in the next iteration, until the value of Q converges.

The functions s_1, f_2, s_2 and t_2 are computed following the procedure described above and the solution of the boundary layer equations are determined up to $O(\alpha^2)$. We can compute the pressure and shear stress at the cylinder surface and integrate to obtain the drag, lift and torque. The drag and lift by the pressure are

$$D_p = \int_A \mathbf{e}_x \cdot (-P\mathbf{1}) \cdot \mathbf{e}_r \,\mathrm{d}A = \int_0^{2\pi} (-P)\cos\theta \, a\mathrm{d}\theta = -\rho Q^2 \alpha \mathrm{Real}(s_1)\pi a, \tag{18.2.74}$$

$$L_p = \int_A \mathbf{e}_y \cdot (-P\mathbf{1}) \cdot \mathbf{e}_r \,\mathrm{d}A = \int_0^{2\pi} (-P)\sin\theta \, a\mathrm{d}\theta = \rho Q^2 \alpha \mathrm{Imag}(s_1)\pi a. \tag{18.2.75}$$

The friction drag and lift by the shear stress are

$$D_f = \int_A \mathbf{e}_x \cdot (\tau_{\theta r}\mathbf{e}_\theta\mathbf{e}_r) \cdot \mathbf{e}_r \,\mathrm{d}A = \int_0^{2\pi} \tau_{\theta r}(-\sin\theta)\, a\mathrm{d}\theta = \mu Q \alpha \mathrm{Imag}(f_1^{''})\pi a, \tag{18.2.76}$$

$$L_f = \int_A \mathbf{e}_y \cdot (\tau_{\theta r}\mathbf{e}_\theta\mathbf{e}_r) \cdot \mathbf{e}_r \,\mathrm{d}A = \int_0^{2\pi} \tau_{\theta r}\cos\theta \, a\mathrm{d}\theta = \mu Q \alpha \mathrm{Real}(f_1^{''})\pi a. \tag{18.2.77}$$

We call the readers' attention to the fact that in our problem, the drag on the cylinder is negative if it is in the uniform flow direction; the drag is positive if it is opposite to the uniform flow direction (see figure 18.4). The drag and lift coefficients are defined as

$$C_{D_p} = \frac{D_p}{\rho U_0^2 a}, \qquad C_{D_f} = \frac{D_f}{\rho U_0^2 a}, \qquad C_D = \frac{D_p + D_f}{\rho U_0^2 a}; \tag{18.2.78}$$

$$C_{L_p} = \frac{L_p}{\rho U_0^2 a}, \qquad C_{L_f} = \frac{L_f}{\rho U_0^2 a}, \qquad C_L = \frac{L_p + L_f}{\rho U_0^2 a}. \tag{18.2.79}$$

The torque is

$$T = -a^2 \int_0^{2\pi} \tau_{\theta r}\,\mathrm{d}\theta = 2\pi\mu a^2 \left(2Q\frac{a+\delta}{a^2} - Q\alpha^2 g_2^{''} + \frac{Q\alpha^2}{a} g_2^{'} \right), \tag{18.2.80}$$

with the dimensionless torque defined as

$$C_T = \frac{T}{2\rho U_0^2 a^2}. \tag{18.2.81}$$

In tables 18.5 – 18.10, we list the drag, lift and torque computed from our boundary layer solutions and compare them to the results of numerical simulation for six cases, (R_e, q/U_0)= (200, 4), (200, 5), (400, 4), (400, 5), (400, 6) and (1000, 3). The boundary layer thickness δ/a is prescribed at different values; when the value of δ/a falls into a certain range (highlighted in tables 18.5 – 18.10), our analysis gives rise to lift and torque in good agreement with the simulation results. The agreement for the drag is less good, which is partly due to the fact that the absolute value of the drag is small and the relative error is apparent. Nevertheless, good agreement for the drag is obtained in the cases (R_e, q/U_0)=(400, 5) and (400, 6), which are the ones with relatively large values of R_e and q/U_0 in the six cases. This indicates that the agreement for the drag becomes better as the prescribed parameters move toward the range in which the theory is supposed to work better. Our solution for (R_e, q/U_0) = (400, 6) using $\delta/a = 0.14$ (see table 18.9) is in excellent agreement with the results of numerical simulation .

We highlight the range of δ/a in which the lift and torque are in good agreement with the simulation results in tables 18.5 – 18.10. We choose one value from this range (typically the median) as a proper boundary layer thickness: $\delta/a = 0.25$, 0.21, 0.17, 0.15, 0.14 and 0.12 for (R_e, q/U_0)= (200, 4), (200, 5), (400, 4), (400, 5), (400, 6) and (1000, 3), respectively. As expected, the boundary layer thickness decreases with increasing Reynolds number and the relation $(\delta/a) \propto (1/\sqrt{R_e})$ seems to hold when q/U_0 is fixed. The boundary layer thickness also decreases with increasing q/U_0, because the rotary flow suppresses the boundary layer induced by the streaming flow.

The choice of δ/a is vital in our calculation. If δ/a is much smaller than the proper boundary layer thickness, the flow there cannot match the potential flow outside, which breaks the assumptions of our calculation. If δ/a is much larger than the proper boundary layer thickness, the value of Q is small and $\alpha = 2U_0/Q$ could be close to 1 or even larger than 1, which makes the power series expansion of the solutions in terms of α slow to converge or even divergent. On the other hand, there is a range of δ/a values which can lead to lift and torque in good agreement with simulation results, because there is no clear-cut boundary layer edge physically. The calculation is reasonably accurate when δ/a falls in this range.

We compare the drag, lift and torque given by our solution using the proper δ/a, by Glauert's solution, by Moore's solution and by the numerical simulation in table 18.11. Equations (18.2.3), (18.2.4) and (18.2.7) are used to compute the lift, drag and torque coefficients given by Glauert's solution. Equation (18.2.10) is used to compute the torque given by Moore's solution; the drag and lift are not computed since Moore did not give the necessary coefficients. The comparison demonstrates that Moore's torque is relatively close to the simulation results, and Glauert's solution gives reasonable approximations for the friction drag and lift but poor approximation for the torque. It also confirms that our solution is indeed an improvement of Glauert's solution, especially in the category of torque.

A key feature of this boundary layer analysis is that the variation of the pressure across the boundary layer is obtained. We integrate the drag and lift components of the pressure over circles concentric with the cylinder but with different radii, then C_{D_p} and C_{L_p} become functions of r. We compare these functions computed from our boundary layer analysis and from numerical simulation in figures 18.5 and 18.6.

The functions $C_{D_p}(r)$ for three cases, R_e=400 and q/U_0=4, 5, and 6 are shown in figures 18.5.(a), 18.5.(b) and 18.5.(c), respectively. Two curves computed from our boundary layer analysis using different values of δ/a are compared to the numerical simulation for (R_e, q/U_0)=(400, 4) in figure 18.5.(a). The dashed line gives the results using δ/a=0.17, which is the boundary layer thickness leading to the best fit for the lift and torque (see table 18.7). The dashed line correctly predicts that C_{D_p} decreases with increasing r, but the values of C_{D_p} are not close to the results of numerical simulation. The solid line gives the results using δ/a=0.2, which are much closer to the simulation results and correctly predict that C_{D_p} changes sign across the boundary layer. Figure 18.5.(b) shows the comparison for the case (R_e, q/U_0)=(400, 5). Again, the dashed line gives the results from our boundary layer analysis using the value of δ/a leading to the best fit for the lift and torque (see table

δ/a	q/Q	C_{D_p}	C_{D_f}	C_D	C_{L_p}	C_{L_f}	C_L	C_T
0.1	1.114	-13.551	-1.388	-14.939	21.563	0.414	21.978	0.277
0.15	1.221	-5.090	-1.010	-6.100	21.303	0.587	21.891	0.328
0.2	1.409	-1.669	-0.848	-2.517	20.153	0.697	20.850	0.400
0.23	1.580	-0.620	-0.788	-1.408	18.938	0.725	19.663	0.446
0.24	**1.649**	**-0.381**	**-0.770**	**-1.152**	**18.444**	**0.729**	**19.173**	**0.461**
0.25	**1.726**	**-0.188**	**-0.754**	**-0.942**	**17.907**	**0.729**	**18.636**	**0.476**
0.26	**1.812**	**-0.0351**	**-0.737**	**-0.772**	**17.329**	**0.727**	**18.056**	**0.490**
0.27	1.907	0.0815	-0.721	-0.639	16.710	0.722	17.432	0.504
0.28	2.012	0.166	-0.704	-0.538	16.055	0.714	16.769	0.517
simulation results		0.728	-0.604	0.124	16.961	0.621	17.582	0.453

Table 18.5. *The comparison of the coefficients for the drag, lift and torque with the simulation results for $R_e = 200$ and q/U_0=4. The lift and torque computed using δ/a =0.24, 0.25 or 0.26 are in reasonable agreement with the results of numerical simulation. The drag, especially the drag due to the pressure, does not agree well with the simulation results. When δ/a=0.28, the value of q/Q is such that $\alpha = 2U_0/Q > 1$, which makes the power series expansions of the solutions in terms of α divergent. The calculation can be performed but cannot be expected to converge to the true result.*

δ/a	q/Q	C_{D_p}	C_{D_f}	C_D	C_{L_p}	C_{L_f}	C_L	C_T
0.1	1.114	-13.061	-1.400	-14.461	27.039	0.517	27.556	0.346
0.15	1.218	-4.157	-1.044	-5.201	27.007	0.730	27.736	0.407
0.19	1.350	-0.988	-0.928	-1.916	26.414	0.845	27.259	0.473
0.2	**1.392**	**-0.468**	**-0.909**	**-1.377**	**26.164**	**0.866**	**27.029**	**0.490**
0.21	**1.437**	**-0.0296**	**-0.893**	**-0.922**	**25.870**	**0.883**	**26.752**	**0.507**
0.22	**1.486**	**0.337**	**-0.878**	**-0.541**	**25.531**	**0.896**	**26.428**	**0.524**
0.25	1.659	1.089	-0.841	0.248	24.243	0.920	25.163	0.574
0.3	2.072	1.531	-0.779	0.752	21.111	0.903	22.014	0.650
0.35	2.804	1.318	-0.690	0.628	16.512	0.813	17.324	0.714
simulation results		0.824	-0.835	-0.0107	26.183	0.846	27.029	0.514

Table 18.6. *The comparison of the coefficients for the drag, lift and torque with the simulation results for $R_e = 200$ and q/U_0=5. The lift and torque computed using δ/a =0.2, 0.21 or 0.22 are in excellent agreement with the results of numerical simulation. The agreement of drag, especially the drag due to the pressure, is not good. When δ/a=0.35, $\alpha = 2U_0/Q > 1$, and the power series expansions of the solutions in terms of α are divergent.*

18.8). The solid line gives the results using a larger δ/a, which are in excellent agreement with the simulation results. Figure 18.5.(c) shows the comparison for the case (R_e, q/U_0)=(400, 6). We plot only one curve from the boundary layer analysis using δ/a=0.14. This value leads to not only the best fit for the lift and torque (see table 18.9), but also excellent agreement for C_{D_p} in 18.5.(c). This comparison demonstrates that our boundary layer analysis can be used to compute the variation of the pressure drag across the boundary layer and the agreement with the numerical simulation becomes better as q/U_0 increases.

The functions $C_{L_p}(r)$ for three cases, R_e=400 and q/U_0=4, 5, and 6 are shown in figure 18.6. In all the three cases, C_{L_p} computed from our boundary layer analysis are in excellent agreement with the numerical simulation. The theory correctly predicts the variation of C_{L_p} with r inside the boundary layer, which is a significant improvement on the irrotational theory and the classical boundary layer theory of Prandtl. The lift force $L = \rho U_0 \Gamma$ from the irrotational theory is a constant at any $r \geq a$ because the circulation is a constant. In the classical boundary layer theory, the pressure is a constant across the boundary layer and the variation of $C_{L_p}(r)$ shown in figure 18.6 cannot be obtained.

δ/a	q/Q	C_{D_p}	C_{D_f}	C_D	C_{L_p}	C_{L_f}	C_L	C_T
0.1	1.155	-5.629	-0.724	-6.352	21.104	0.396	21.499	0.173
0.13	1.277	-2.249	-0.610	-2.859	20.292	0.470	20.762	0.215
0.15	1.398	-1.008	-0.565	-1.572	19.357	0.498	19.855	0.246
0.16	1.472	-0.582	-0.547	-1.129	18.766	0.506	19.272	0.261
0.17	**1.558**	**-0.258**	**-0.530**	**-0.788**	**18.094**	**0.509**	**18.603**	**0.276**
0.18	**1.657**	**-0.0178**	**-0.514**	**-0.532**	**17.343**	**0.509**	**17.852**	**0.291**
0.2	1.906	0.260	-0.483	-0.223	15.613	0.497	16.110	0.318
0.23	2.466	0.316	-0.432	-0.116	12.551	0.453	13.004	0.352
simulation results		0.534	-0.451	-0.0836	17.609	0.447	18.057	0.275

Table 18.7. *The comparison of the coefficients for the drag, lift and torque with the simulation results for $R_e = 400$ and q/U_0=4. The lift and torque computed using δ/a =0.17 or 0.18 are in excellent agreement with the results of numerical simulation. The agreement of drag, especially the drag due to the pressure, is not good. When δ/a=0.23, $\alpha = 2U_0/Q > 1$, and the power series expansions of the solutions in terms of α are divergent.*

δ/a	q/Q	C_{D_p}	C_{D_f}	C_D	C_{L_p}	C_{L_f}	C_L	C_T
0.1	1.153	-4.803	-0.746	-5.550	26.670	0.491	27.187	0.215
0.13	1.266	-1.190	-0.650	-1.840	26.140	0.582	26.722	0.263
0.14	**1.315**	**-0.457**	**-0.631**	**-1.089**	**25.816**	**0.602**	**26.419**	**0.280**
0.15	**1.370**	**0.112**	**-0.617**	**-0.504**	**25.420**	**0.618**	**26.038**	**0.297**
0.16	**1.431**	**0.548**	**-0.604**	**-0.056**	**24.952**	**0.630**	**25.582**	**0.314**
0.2	1.750	1.386	-0.565	0.821	22.366	0.641	23.007	0.374
0.25	2.502	1.313	-0.493	0.820	16.923	0.577	17.500	0.440
simulation results		0.591	-0.601	-0.010	26.415	0.597	27.011	0.297

Table 18.8. *The comparison of the coefficients for the drag, lift and torque with the simulation results for $R_e = 400$ and q/U_0=5. The lift and torque computed using δ/a =0.14 or 0.15, and the drag computed using δ/a =0.16 are in good agreement with the results of numerical simulation. When δ/a=0.25, $\alpha = 2U_0/Q > 1$, and the power series expansions of the solutions in terms of α divergent.*

18.2.6 Higher-order boundary layer theory

Glauert's analysis is a first order boundary layer approximation for the flow past a rotating cylinder. Our analysis here is intended to be an improvement of his boundary layer solution. Another possible way to improve Glauert's solution is the higher-order boundary layer theory based on the method of matched asymptotic expansions (Lagerstrom and Cole 1955, Van Dyke 1962a, 1969, Maslen 1963). We discuss the differences between our approach and the higher-order boundary layer theory.

The basic idea of the higher-order boundary layer theory is to construct outer and inner asymptotic expansions, by iterating the Navier-Stokes equations about the outer solution and about the boundary layer solution, respectively, and to match the two expansions in their overlap region of validity. Tani (1977) remarked "Higher approximations have thus been found only for flows without separation. In such cases the first term of the outer expansion is the inviscid irrotational flow, from which the first term of the inner expansion is determined by Prandtl's approximation. The second term of the outer expansion is the irrotational flow due to an apparent source distribution representing the displacement effect of Prandtl's boundary layer. This then determines a correction to the boundary-layer solution, yielding the second term of the inner expansion." The second order corrections are terms proportional to $1/\sqrt{R_e}$ and the third order terms are proportional to $1/R_e$. Since the viscous term in the Navier-Stokes equations for the outer flow is on the order of $1/R_e$, the higher-order theory needs to compute the third order corrections to account for the viscous effects of the outer flow. Van Dyke (1969) remarked "Definite results in the literature are restricted mostly to laminar boundary layer, to steady motion, to plane or axisymmetric flows, and to the second approximation." We are not aware of any third order corrections in the literature. For incompressible fluids, the first and second order terms for the outer expansion are irrotational (Panton 1984, Tani 1977); it is not clear whether the third order term is irrotational

δ/a	q/Q	C_{D_p}	C_{D_f}	C_D	C_{L_p}	C_{L_f}	C_L	C_T
0.1	1.151	-3.860	-0.773	-4.633	32.48	0.585	33.06	0.256
0.12	1.216	-1.031	-0.714	-1.744	32.48	0.660	33.14	0.290
0.13	1.254	-0.0650	-0.697	-0.762	32.42	0.690	33.11	0.308
0.135	**1.274**	**0.331**	**-0.691**	**-0.361**	**32.37**	**0.703**	**33.07**	**0.316**
0.14	**1.296**	**0.676**	**-0.686**	**-0.0105**	**32.31**	**0.714**	**33.03**	**0.325**
0.145	**1.317**	**0.975**	**-0.682**	**0.293**	**32.24**	**0.725**	**32.97**	**0.333**
0.15	1.340	1.233	-0.679	0.554	32.16	0.734	32.90	0.342
0.2	1.577	2.318	-0.678	1.641	31.31	0.788	32.10	0.408
simulation results		0.668	-0.681	-0.0136	33.09	0.682	33.77	0.316

Table 18.9. *The comparison of the coefficients for the drag, lift and torque with the simulation results for $R_e = 400$ and q/U_0=6. The drag, lift and torque computed using $\delta/a = 0.14$ are in excellent agreement with the results of numerical simulation. The calculation is reasonable accurate in the range $0.135 \leq \delta/a \leq 0.145$.*

δ/a	q/Q	C_{D_p}	C_{D_f}	C_D	C_{L_p}	C_{L_f}	C_L	C_T
0.08	1.217	-3.185	-0.362	-3.547	14.72	0.220	14.94	0.0801
0.1	1.418	-1.509	-0.310	-1.819	13.20	0.237	13.44	0.106
0.12	**1.755**	**-0.755**	**-0.273**	**-1.028**	**11.08**	**0.232**	**11.31**	**0.130**
simulation results		0.213	-0.197	0.0155	10.41	0.192	10.60	0.118

Table 18.10. *The comparison of the coefficients for the drag, lift and torque with the simulation results for $R_e = 1000$ and q/U_0=3. The lift and torque computed using $\delta/a = 0.1$ or 0.12 are close to the results of numerical simulation. However, it should be noted that $\alpha = 1.17 > 1$ when $\delta/a = 0.12$ and the power series expansions of the solutions in terms of α divergent. This is caused by the relatively low value of the speed ratio $q/U_0 = 3$. If Glauert's solution is used for this case, $\alpha = 1.064$ and Glauert's solution also diverges.*

or not. Suppose the outer flow is irrotational at all orders and the fluid is incompressible, the viscous term $\mu\nabla^2\mathbf{u}$ disappears identically, which indicates that the viscous effects of the outer potential flow do not enter the higher-order boundary layer theory if only velocity is matched but stress is not considered. Suppose the third order term for the outer flow is rotational, the viscous term is then proportional to $1/R_e$, which should give viscous effects to the inner solution at the third order.

Our new approach to boundary layer flow is different from the higher-order boundary layer theory and is not based on method of matched asymptotic expansions. The matching conditions at the outer edge of the boundary layer are for the velocity in higher-order boundary layer theory; shear stress has not been considered. We enforce the continuity of the shear stress at the outer edge of the boundary layer. Because we are considering one single fluid, the viscosity is the same inside and outside the boundary layer. The continuity of the shear stress is equivalent to continuity of velocity gradients. Since the velocity gradients for the outer flow are of order 1, our approach is not the same as the third order corrections of the higher-order boundary theory.

Glauert's analysis is a first order boundary layer approximation. He ignored the irrotational rotary flow component of the flow in the boundary layer, which is justifiable because the irrotational rotary flow is a second order effect in the boundary layer. The torque coefficient by Glauert is on the order of $1/\sqrt{R_e}$, and the torque coefficient in a purely irrotational rotary flow (without forward flow) is on the order of $1/R_e$. However, numerical simulation shows that the higher order correction is not negligible in this case. When $R_e = 400$ and $q/U_0 = 6$, the torque coefficient by Glauert is only 40% of the result of numerical simulation. It is conceivable that higher-order boundary layer theory using the method of matched asymptotic expansions can be applied to this problem and yield corrections for Glauert's solution; but this has not been done. Our analysis is compared to the numerical simulation and good to excellent agreement is observed. Admittedly, the outer flow in our analysis is a first order approximation and can be improved by higher order corrections.

The pressure across the boundary layer can no longer be taken as a constant in higher-order theory. On a curved wall centrifugal force produces a pressure gradient across the boundary layer, which is a second-order

solution	R_e	q/U_0	α	C_{D_p}	C_{D_f}	C_D	C_{L_p}	C_{L_f}	C_L	C_T
Numerical simulation	200	4	-	0.728	-0.604	0.124	16.961	0.621	17.582	0.453
This work	200	4	0.863	-0.188	-0.754	-0.942	17.907	0.729	18.636	0.476
Glauert's solution	200	4	0.625	0	-0.795	-0.795	20.102	0.795	20.897	0.215
Moore's solution	200	4	-	-	-	-	-	-	-	0.408
Numerical simulation	200	5	-	0.824	-0.835	-0.0107	26.183	0.846	27.029	0.514
This work	200	5	0.575	-0.0296	-0.893	-0.922	25.870	0.883	26.752	0.507
Glauert's solution	200	5	0.457	0	-0.929	-0.929	27.483	0.929	28.412	0.195
Moore's solution	200	5	-	-	-	-	-	-	-	0.440
Numerical simulation	400	4	-	0.534	-0.451	-0.0836	17.609	0.447	18.057	0.275
This work	400	4	0.779	-0.258	-0.530	-0.788	18.094	0.509	18.603	0.277
Glauert's solution	400	4	0.625	0	-0.562	-0.562	20.102	0.562	20.664	0.152
Moore's solution	400	4	-	-	-	-	-	-	-	0.237
Numerical simulation	400	5	-	0.591	-0.601	-0.010	26.415	0.597	27.011	0.297
This work	400	5	0.548	0.112	-0.617	-0.504	25.420	0.618	26.038	0.297
Glauert's solution	400	5	0.457	0	-0.657	-0.657	27.483	0.657	28.140	0.138
Moore's solution	400	5	-	-	-	-	-	-	-	0.246
Numerical simulation	400	6	-	0.668	-0.681	-0.0136	33.09	0.682	33.77	0.316
This work	400	6	0.432	0.676	-0.686	-0.0105	32.31	0.714	33.03	0.325
Glauert's solution	400	6	0.365	0	-0.736	-0.736	34.46	0.736	35.20	0.126
Moore's solution	400	6	-	-	-	-	-	-	-	0.263
Numerical simulation	1000	3	-	0.213	-0.197	0.0155	10.41	0.192	10.60	0.118
This work	1000	3	1.17	-0.755	-0.273	-1.028	11.08	0.232	11.31	0.130
Glauert's solution	1000	3	1.06	0	-0.273	-0.273	11.81	0.273	12.08	0.108
Moore's solution	1000	3	-	-	-	-	-	-	-	0.131

Table 18.11. *The comparison of the solution in this work, using δ/a=0.25, 0.21, 0.17, 0.15, 0.14 and 0.12 for (R_e, q/U_0)= (200, 4), (200, 5), (400, 4), (400, 5), (400, 6) and (1000, 3) respectively, with the simulation results and Glauert's and Moore's solutions. Note that in our problem, the drag on the cylinder is negative if it is in the uniform flow direction; the drag is positive if it is opposite to the uniform flow direction (see figure 18.4). We call the readers' attention to the fact that $\alpha > 1$ in our solution and in Glauert's solution when (R_e, q/U_0) = (1000, 3); the solutions are not expected to converge to the true results.*

effect. Van Dyke (1969) inserted the irrotational surface speed with a correction due to the surface curvature into Bernoulli's equation for the external flow to compute the pressure at the outer edge of the boundary layer and it has no viscous terms. The pressure inside the boundary layer can be computed using this condition and the equation

$$\frac{\partial \overline{p}_2}{\partial n} = \kappa \overline{u}_1^2, \tag{18.2.82}$$

where $\overline{p}_2$ is the second order correction for the pressure, n is normal to the surface, κ is the surface curvature and $\overline{u}_1$ is the first order velocity from Prandtl's boundary layer theory. Because $\overline{u}_1$ has viscous terms, the pressure at the wall computed from (18.2.82) should have viscous terms. But in the applications of the higher-order theory to problems of leading edges and parabola in uniform stream by Van Dyke (1962b, 1964), the second order correction for the pressure was not computed; the drag is computed only using skin friction and the pressure is not considered.

In summary, the higher-order boundary layer theory has not yet been applied to determine (1) the effect of the viscous dissipation of the outer irrotational flow; (2) the effect generated by a mismatch between the shear stress at the effective edge of the boundary layer and the irrotational shear stress there; (3) the drag and lift on the body due to normal stress associated with the viscous contribution to the pressure.

The numerical simulations show that the region in which the vortical effects are important is thick around the rotating cylinder. For example, the thickness of the vortical region determined using a 1% of the maximum vorticity magnitude criterion is 26% of the cylinder radius for $R_e = 400$ and $q/U_0 = 5$. The higher-order boundary layer theory might encounter difficulty when treating such problems. Weinbaum, Kolansky, Gluckman

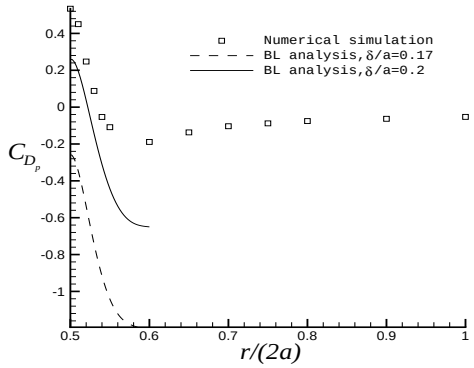

(a) R_e=400, q/U_0=4.

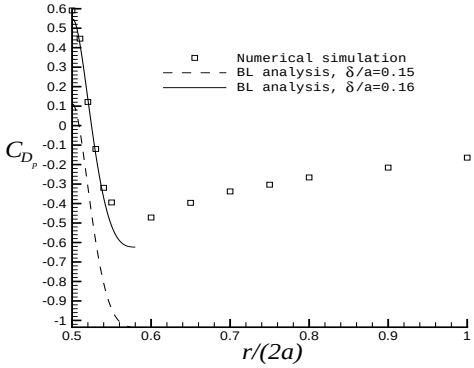

(b) R_e=400, q/U_0=5.

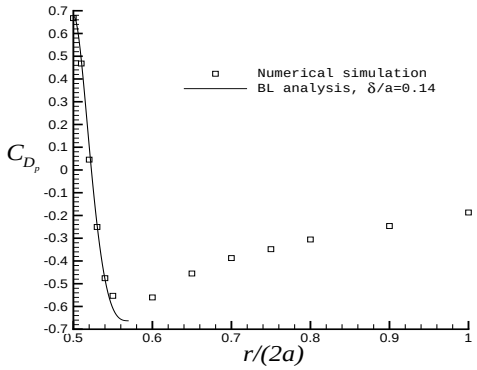

(c) R_e=400, q/U_0=6.

Fig. 18.5. Comparison of the coefficient for the pressure drag C_{D_p} as a function of the radial position. (a) R_e=400, q/U_0=4. Our boundary layer analysis: dashed line – using $\delta/a = 0.17$; solid line – using $\delta/a = 0.2$. The results of numerical simulation: □. (b) R_e=400, q/U_0=5. Our boundary layer analysis: dashed line – using $\delta/a = 0.15$; solid line – using $\delta/a = 0.16$. The results of numerical simulation: □. (c) R_e=400, q/U_0=6. Our boundary layer analysis using$\delta/a = 0.14$: solid line. The results of numerical simulation: □. C_{D_p} from our boundary layer analysis can only be computed inside the boundary layer: $a \le r \le a + \delta$; C_{D_p} from numerical simulation is plotted up to $r = 2a$.

and Pfeffer (1976) proposed an approximate method, which is not based on asymptotic analysis, to improve Prandtl's boundary layer theory. They focused on flows with the Reynolds number range $O(1) < R_e < O(10^2)$, where the boundary layer is thick and a steady laminar wake is present. They remarked "It is not surprising in view of the large changes in effective body shape which the external inviscid flow must experience at these Reynolds numbers that a theory of successive approximation which is based on the potential flow past the original body shape will converge very slowly. This would appear to be the basic difficulty encountered in extending the results of second-order boundary-layer theory (Van Dyke 1962) to flows with Reynolds numbers less than about 10^3." The method of Weinbaum *et al.* is based on a pressure hypothesis which enables one to take account of the displacement interaction and centrifugal effects in thick boundary layers using conventional first-order boundary layer equations. Weinbaum *et al.* neglected the viscous term in the pressure which we have mentioned in the discussion of equation (18.2.82). They solved the momentum integral of the boundary layer equations using the fourth-order Pohlhausen profile to obtain the displacement thickness. They treated the flows past parabolic and circular cylinders and obtained results in excellent agreement with numerical Navier-Stokes solutions. The method of Weinbaum *et al.* shares the common feature with ours that the boundary layer thickness has to be taken into account in the solution. However, like the higher-order boundary layer theory, the method of Weinbaum *et al.* does not consider the shear stress discrepancy at the effective edge of the boundary layer, or the viscous contribution to the pressure.

18.2.7 Discussion and conclusion

The dependence of the lift on R_e and q/U_0 is a key problem in the study of the flow past a rotating cylinder. Our work here and numerical simulations (Mittal and Kumar 2003, Padrino and Joseph 2006) show clearly that the lift force increases with increasing q/U_0; the major contribution to the lift is from the pressure and the friction lift is much smaller than the pressure lift. The numerical simulation results show that the influence of

the Reynolds number on the pressure lift is small; the friction lift seems to decrease with increasing Reynolds number (table 18.11). Glauert's prediction that the pressure lift is independent of R_e, is a good approximation to the results of numerical simulation; our solution which considers the viscous effects on the pressure is in even better agreement with the results of numerical simulation. Kang, Choi and Lee (1999) simulated the flows with R_e=40, 60, 100 and 160 and q/U_0 between 0 and 2.5. The temporal-averaged values of pressure lift, pressure drag, friction lift and friction drag, computed after the flow becomes fully developed, were presented in their paper. They showed that the friction lift decreases with increasing R_e and the pressure lift is nearly independent of R_e. These results are consistent with Padrino and Joseph (2004) and our work, despite the fact that most of the flows studied by Kang, Choi and Lee (1999) do not satisfy the assumptions that the separation is suppressed and steady state solution exists.

The dependence of the drag on R_e and q/U_0 is more complicated than the lift. Mittal and Kumar (2003) simulated the flows with R_e=200 and q/U_0 between 0 and 5; they presented the total drag coefficients C_D for the fully developed flows. The results show that when $q/U_0 < 1.91$, the flow is unsteady and the drag is oscillating; but the drag on the cylinder is always in the direction of the uniform flow. When $2 < q/U_0 < 4.34$ or $4.75 < q/U_0 < 5$, separation is suppressed and steady state drag coefficients are obtained. The magnitude of C_D decreases with q/U_0 first, from about 0.3 at $q/U_0 = 2$ to about 0 at $q/U_0 = 3.25$. If q/U_0 is higher than 3.25, the magnitude of C_D is very close to zero; C_D could be slightly positive or negative. Kang, Choi and Lee (1999) presented the temporal-averaged values for the total drag, pressure drag and friction drag. They showed that the magnitude of the total drag decreases with increasing q/U_0 but the total drag is in the same direction as the uniform flow for all the flows they studied. The magnitude of the pressure drag also decreases with increasing q/U_0; when $0 < q/U_0 < 2$, the pressure drag is in the same direction as the uniform flow but when $q/U_0 = 2.5$, the pressure drag becomes opposite to the uniform flow. Similar results were obtained by Padrino and Joseph (2004), who showed that the pressure drag is opposite to the uniform flow for q/U_0=3, 4, 5, 6 and it is in competition with the friction drag, resulting in a total drag which is close to zero (see tables 18.5 – 18.10). The reason for the pressure drag to become opposite to the uniform flow is not understood.

The pressure drag is a viscous effect. It cannot be studied using the classical boundary layer theory, in which the irrotational pressure is imposed on the solid. Our boundary layer solution is able to give a pressure drag. The agreement between this pressure drag and the result of numerical simulation depends on the choice of the boundary layer thickness in our calculation. When q/U_0 is not high enough (q/U_0=4 or 5), it seems that the value of δ/a which gives rise to a good agreement for the pressure drag is larger than the value of δ/a which leads to good agreements for the lift and torque (see tables 18.5 – 18.8 and figure 18.5). In the case (R_e, q/U_0) = (400, 6), we can find a single value of δ/a which leads to good agreement for all the three quantities lift, torque and drag (see table 18.9), demonstrating that the agreement between our solution and numerical simulation becomes better as q/U_0 increases.

We presented a comprehensive comparison for the drag, lift and torque on the cylinder given by our solution, by Glauert's (1957) solution, by Moore's solution (1957) and by the numerical simulation. The comparison demonstrates that Moore's torque is relatively close to the simulation results, and Glauert's solution gives reasonable approximations for the friction drag and lift but poor approximation for the torque. Our solution gives the best approximation to the numerical simulation when the value of δ/a is chosen to fit the numerical data. We also compared the profiles of the pressure drag and lift inside the boundary layer given by our solution and given by numerical simulation. The agreement of the lift profile is good (figure 18.6); the agreement of the drag profile is less good for small values of q/U_0 but improves as q/U_0 increases (figure 18.5). Such profiles are not available in Prandtl's boundary layer theory, in which the pressure is equal to the irrotational pressure throughout the boundary layer.

The accuracy of our solution is mainly affected by the values of $\alpha = 2U_0/q$ and δ/a. Since we only carried out the calculation up to terms quadratic in α, the solution can be accurate only when α is very small. From table 18.11, one can see that the smallest value of α corresponds to (R_e, q/U_0)=(400, 6); other values of α in our work are all larger than 0.5. This is one of the reasons why the agreement between our solution and the numerical simulation is best for the case (R_e, q/U_0)=(400, 6). The boundary layer thickness depends on the azimuthal angle θ, but we are not able to determine this dependence. We assume that δ is a constant for given R_e and q/U_0 and the value of δ/a used in our calculation may be viewed as an average boundary layer thickness.

Numerical simulation will be used to determine δ/a at different azimuthal angle using the criterion that the vorticity magnitude at $r = a+\delta$ is approximately 1% of the maximum magnitude of the vorticity field. Plots for δ/a as a function of θ will be shown in figure 18.14 in Section 18.3. The figure shows that the deviation of δ/a from its average is large when R_e or q/U_0 is small, and the deviation is small when R_e and q/U_0 is large. This result may explain why the agreement between our solution and numerical simulation becomes better when R_e and q/U_0 increases.

The problem confronted in this work is that there is no precise end to the boundary layer although most of the vorticity is confined to a region near to the spinning cylinder when the ratio of cylinder rotating speed to uniform stream speed q/U_0 is large. We have addressed this problem using the idea of an effective boundary layer thickness, which is determined by matching with the results of numerical simulation. The thickness depends on the choice of the quantities for the matching. We are able to match lift, drag, and torque from our boundary layer analysis for large values of q/U_0 and R_e. In Section 18.1, an effective boundary layer thickness was found which gave rise to reasonable matching for the pressure lift and torque on the cylinder computed from a simple modification of Glauert's solution (1957), and for the pressure drag computed from the method of viscous correction of viscous potential flow (VCVPF). The values of the effective thickness in Section 18.1 are about 1/2 or 1/3 of the values in this section. A method to determine the boundary layer thickness without the aid of numerical simulation needs to be developed.

18.3 Numerical study of the steady state uniform flow past a rotating cylinder

Results from the numerical simulation of the two-dimensional incompressible unsteady Navier-Stokes equations for streaming flow past a rotating circular cylinder are presented in this section. The numerical solution of the equations of motion is conducted with a commercial computational fluid dynamics package which discretizes the equations applying the control volume method. The numerical setup is validated by comparing results for a Reynolds number based on the free stream of $Re = 200$ and dimensionless peripheral speed of $\tilde{q} = 3$, 4 and 5 with results from the literature. After the validation stage, various pairs of Re and $\tilde{q}$ are specified in order to carry out the numerical experiments. These values are $Re = 200$ with $\tilde{q} = 4$ and 5; $Re = 400$ with $\tilde{q} = 4$, 5 and 6, and $Re = 1000$ with $\tilde{q} = 3$. In all these cases, gentle convergence to fully developed steady state is reached. From the numerical vorticity distribution, the position of the outer edge of the vortical region is determined as a function of the angular coordinate. This position is found by means of a reasonable criterion set to define the outmost curve around the cylinder where the vorticity magnitude reaches a certain cut off value. By considering the average value of this profile, a uniform vortical region thickness is specified for every pair of Re and $\tilde{q}$.

18.3.1 Introduction

Two aspects have drawn attention from researchers with respect to streaming flow past a rotating circular cylinder. The first aspect is the observation that the spinning action is able to suppress the separation of the boundary layer around the cylinder as well as to avoid vortex shedding from the surface of the cylinder while reaching steady state when a critical dimensionless velocity is achieved. This threshold has been reported to be a function of the Reynolds number of the free stream. The second aspect is the lift generated on the cylinder by the surrounding fluid, also named as the Magnus effect. Prandtl's famous limiting value of the lift force generated by a rotating circular cylinder has encountered contradictory evidence from theoretical studies, experiments and computations (e.g., Glauert 1957; Tokumaru & Dimotakis 1993; Mittal & Kumar 2001), thus making this problem even more attractive as the subject for improved numerical methods and experimental techniques.

The literature reveals that two relevant parameters are usually specified to describe the problem, namely, the Reynolds number $Re = 2U_0a/\nu$, based on the free stream velocity U_0, the diameter of the cylinder $2a$ and fluid kinematic viscosity ν, and the dimensionless peripheral velocity $\tilde{q}$, defined as the ratio of the velocity magnitude at the surface of the cylinder to the free stream velocity. From the point of view of the numerical simulations, setting the appropriate range for these parameters is a delicate task on which part of the success

of the numerical work relies. Another feature is the choice of the form of the governing equations to solve. For a two-dimensional problem, the vorticity and stream function form of the Navier-Stokes equations is the preferred option. However, some researchers have carried out their numerical work with the equations of motion written in terms of the primitive variables, velocity and pressure. Ingham (1983) obtained numerical solutions of the two-dimensional steady incompressible Navier-Stokes equations in terms of vorticity and stream function using finite differences for flow past a rotating circular cylinder for Reynolds numbers $Re = 5$ and 20 and dimensionless peripheral velocity $\tilde{q}$ between 0 and 0.5. Solving the same form of the governing equations but expanding the range for $\tilde{q}$, Ingham & Tang (1990) showed numerical results for $Re = 5$ and 20 and $0 \leqslant \tilde{q} \leqslant 3$. With a substantial increase in Re, Badr *et al.* (1990) studied the unsteady two-dimensional flow past a circular cylinder which translates and rotates starting impulsively from rest both numerically and experimentally for $10^3 \leqslant Re \leqslant 10^4$ and $0.5 \leqslant \tilde{q} \leqslant 3$. They solved the unsteady equations of motion in terms of vorticity and stream function. The agreement between numerical and experimental results was good except for the highest rotational velocity where they observed three-dimensional and turbulence effects. Choosing a moderate interval for Re, Tang & Ingham (1991) followed with numerical solutions of the steady two-dimensional incompressible equations of motion for $Re = 60$ and 100 and $0 \leqslant \tilde{q} \leqslant 1$. They employed a scheme that avoids the difficulties regarding the boundary conditions far from the cylinder.

Considering a moderate constant $Re = 100$, Chew, Cheng & Luo (1995) further expanded the interval for the dimensionless peripheral velocity $\tilde{q}$, such that $0 \leqslant \tilde{q} \leqslant 6$. They used a vorticity stream function formulation of the incompressible Navier-Stokes equations. The numerical method consisted of a hybrid vortex scheme, where the time integration is split into two fractional steps, namely, pure diffusion and convection. They separated the domain into two regions: the region close to the cylinder where viscous effects are important and the outer region where viscous effects are neglected and potential flow is assumed. Using the expression for the boundary layer thickness for flow past a flat plate, they estimated the thickness of the inner region. Their results indicated a critical value for $\tilde{q}$ about 2 where vortex shedding ceases and the lift and the drag coefficients tend to asymptotic values. Nair, Sengupta & Chauhan (1998) expanded their choices for the Reynolds number by selecting a moderate $Re = 200$ with $\tilde{q} = 0.5$ and 1 and two relatively high values of $Re = 1000$ and $Re = 3800$, with $\tilde{q} = 3$ and $\tilde{q} = 2$, respectively. They performed the numerical study of flow past a translating and rotating circular cylinder solving the two-dimensional unsteady Navier-Stokes equations in terms of vorticity and stream function using a third-order upwind scheme. Kang, Choi & Lee (1999) followed with the numerical solution of the unsteady governing equations in the primitive variables velocity and pressure for flows with $Re = 60$, 100 and 160 with $0 \leqslant \tilde{q} \leqslant 2.5$. Their results showed that vortex shedding vanishes when $\tilde{q}$ increases beyond a critical value which follows a logarithmic dependence on the Reynolds number (e.g., the critical dimensionless peripheral velocity $\tilde{q} = 1.9$ for $Re = 160$).

Chou (2000) worked on the ground of high Reynolds numbers by presenting a numerical study that included computations falling into two categories: $\tilde{q} \leqslant 3$ with $Re = 10^3$ and $\tilde{q} \leqslant 2$ with $Re = 10^4$. Chou solved the unsteady two-dimensional incompressible Navier-Stokes equations written in terms of vorticity and stream function. In contrast, the recent work of Mittal & Kumar (2003) performed a comprehensive numerical investigation by fixing a moderate value of $Re = 200$ while considering a wide interval for the dimensionless peripheral velocity of $0 \leqslant \tilde{q} \leqslant 5$. They used the finite element method to solve the unsteady incompressible Navier-Stokes equations in two-dimensions for the primitive variables velocity and pressure. They observed vortex shedding for $\tilde{q} < 1.91$. Steady state fully developed flow was achieved for higher rotation rates except for the narrow region $4.34 < \tilde{q} < 4.8$ where vortex shedding was again reported, perhaps, for the first time. This literature survey indicates that researchers have favored moderate Reynolds numbers $Re \leqslant 200$ in order to keep the turbulence effects away and to prevent the appearance of non-physical features in their numerical results. For similar reasons, the peripheral speed have been chosen such that $\tilde{q} \leqslant 3$ in the most of the cases, whereas few researchers have simulated beyond this value, with $\tilde{q} = 6$ as an upper bound.

Many studies have been devoted to the numerical simulation of this type of fluid motion to address the problem of presence or suppression of separation and vortex shedding. However, rather less attention has been paid to the application of numerical results to delimit and describe the region around the cylinder where vorticity effects are far from negligible. This fluid zone is named as the vortical region. Once this region is delimited, the evaluation of theoretical boundary layer-type solutions is feasible. When Re and $\tilde{q}$ are not so high, say $Re <$

1000 and $\tilde{q} < 5$, the vortical region can be relatively thick, so the classical thin boundary layer analysis may not work with acceptable accuracy; nevertheless, there is still an identifiable region where the effects of vorticity are significant. Outside this region, the potential flow theory for flow past a circular cylinder with circulation may be applied.

This section concerns two main objectives: The first objective is to simulate numerically the steady state limit of the flow past a rotating circular cylinder. The second objective is to bound the region around the rotating cylinder where the vorticity effects are mostly confined. The numerical results presented in this section are intended to test the validity of the theoretical approaches of sections 18.1 and 18.2. A value for an effective, uniform thickness of the vortical region needs to be prescribed in these models. The flow field obtained from numerical analysis represents reliable data that can be utilized to estimate the limits of the vortical region. The numerical simulations are performed by solving the two-dimensional incompressible unsteady Navier-Stokes equations utilizing the commercial package Fluent® 6.1. Tests of mesh refinement were used to select the size of the computational domain and mesh structure. Validation of the numerical setup is performed comparing our results with those from the literature for three cases.

Next, the velocity and pressure fields are computed for Reynolds numbers based on the free stream velocity $Re = 200$ and 400, with dimensionless peripheral velocity $\tilde{q} = 4$, 5 and 6. Results for $Re = 1000$ with $\tilde{q} = 3$ are also considered. The drag and lift coefficients on the rotating cylinder are presented. From the numerical vorticity distribution in the fluid domain, the position of the outer edge of the vortical region is determined as a function of the angular coordinate. This position is found by means of a reasonable criterion set to define the outmost curve around the cylinder where the vorticity magnitude reaches a certain cut off value. By considering the average value of this profile, a uniform vortical region thickness is specified for every pair of Re and $\tilde{q}$. The selection of this cut off value is somewhat arbitrary and moderate changes in this parameter may yield significant changes in the extension of the vortical region. This feature motivates the introduction of an effective vortical region thickness, which represents an alternative approach to define the position of the outer edge of the vortical region. The theoretical approach in section 18.1 and the numerical results are utilized to determine two different values of the effective vortical region thickness. Exhaustive comparisons have been presented and discussed in section 18.1 and 18.2.

18.3.2 Numerical features

The two-dimensional unsteady incompressible Navier-Stokes equations are the governing expressions for the problem at hand. In dimensionless form, these equations can be written as:

$$\frac{\partial \tilde{\mathbf{u}}}{\partial \tilde{t}} + \tilde{\mathbf{u}} \cdot \nabla \tilde{\mathbf{u}} = -\nabla \tilde{p} + \frac{1}{Re} \nabla^2 \tilde{\mathbf{u}}, \tag{18.3.1}$$

and

$$\nabla \cdot \tilde{\mathbf{u}} = 0, \tag{18.3.2}$$

on a domain Φ with boundaries Λ and subject to appropriate boundary conditions. The symbol "~" designates dimensionless variables. Unless otherwise noted, the following scales are considered to make the equations dimensionless:

$$[\, length,\, velocity,\, time,\, pressure \,] \equiv \left[2a,\, U_0,\, \frac{2a}{U_0},\, \rho U_0^2 \right]. \tag{18.3.3}$$

Three relevant parameters computed from the velocity and pressure fields are the drag, lift and torque coefficients, which represent dimensionless expressions of the forces and torque that the fluid produces on the circular cylinder. These are defined, respectively, as follows:

$$C_D = \frac{D}{\rho U_0^2 a}, \qquad C_L = \frac{L}{\rho U_0^2 a}, \qquad C_T = \frac{T}{2\rho U_0^2 a^2}, \tag{18.3.4}$$

where D is the drag force, L is the lift force and T is the torque with respect to the center of the cylinder.

The numerical solution of the governing system of partial differential equations is carried out through the computational fluid dynamics package Fluent® 6.1. This computer program applies a control-volume method to integrate the equations of motion, constructing a set of discrete algebraic equations with conservative properties. The segregated numerical scheme, which solves the discretized governing equations sequentially, is selected. An implicit scheme is applied to obtain the discretized system of equations. The sequence updates the velocity field through the solution of the momentum equations using known values for pressure and velocity. Then, it solves a "Poisson-type " pressure correction equation obtained by combining the continuity and momentum equations. A Quadratic Upwind Interpolation for Convective Kinematics (QUICK) scheme is used to discretize the convective term in the momentum equations. Pressure-Implicit with Splitting of Operators (PISO) is selected as the pressure-velocity coupling scheme. Finally, the time integration of the unsteady momentum equations is performed using a second order approximation.

Although from a mathematical point of view the problem set-up imposes boundary conditions at infinity, the numerical approach necessarily considers a finite computational domain. Hence, there is an outer boundary where inflow and outflow boundary conditions should be applied. Figure 18.7 shows the computational domain and the reference frames selected for this study. We use a modified O-type mesh similar to the one adopted by Kang *et al.* (1999). Other mesh types reported in the literature are the C-type mesh referred by Kang *et al.* (1999) and the square-type mesh used by Mittal & Kumar (2003) in their finite elements computations. An O-type mesh is expected to save computational effort as compared with a C-type mesh or a square mesh with sides of length H/a. In this study, the domain is partially delimited by two arcs of a circle, one upstream of the cylinder and the other one downstream, and both have the same radius H. The dimensionless radius of the upstream and downstream arcs is determined as $\tilde{H} \equiv H/2a$.

The boundary conditions applied in this investigation can be described as follows: The left arc Λ_1 (Figure 18.7) is the inflow section or upstream section, where a Dirichlet-type boundary condition for the cartesian velocity components, $\tilde{u} = 1$ and $\tilde{v} = 0$ is prescribed, i.e., the free stream velocity is imposed. The right arc Λ_2 represents the outflow boundary, where it is considered that the diffusion flux in the direction normal to the exit surface is zero for all variables. Therefore, extrapolation from inside the computational domain is used to compute the flow variables at the outflow plane, which do not influence the upstream conditions.‡ On the straight horizontal segments Λ_3^+ and Λ_3^- a zero normal velocity and a zero normal gradient of all variables are prescribed. As a consequence, a zero shear stress condition is imposed at these two boundaries. These relatively short segments are two chords in a circle of radius H, parallel to the horizontal x axis and are symmetric with respect to the vertical y axis. The sectors of the circle that contain these segments have a span of 10° each. The inclusion of these segments defines a transition region between the inlet and outlet sections, and can be thought to be the adaptation to an O-type mesh of the zero-shear-stress upper and lower boundaries, parallel to the free stream, that Mittal & Kumar (2003) used in their domain. Finally, the dimensionless peripheral or tangential velocity $\tilde{q}$ is prescribed on the surface of the rotating cylinder along with a no-slip boundary condition. The cylinder rotates in the counter-clockwise direction.

As initial condition in this numerical investigation the values given to the velocity components at the inflow section are extended over the interior of the computational domain. Since we are focused on the fully developed flow, as Kang *et al.* (1999) pointed out, the simulations may be started with arbitrary initial conditions. They performed a numerical study with different initial conditions, including the impulsive start-up, for $Re = 100$ and $\tilde{q} = 1.0$ and the same fully developed response of the flow motion was eventually reached in all the cases. In contrast, solving the steady version of the Navier-Stokes equations may yield multiple numerical solutions, depending on the given Re and $\tilde{q}$ and the initial guess used to start the computations, as was demonstrated from simulations carried out by Mittal & Kumar (2003). Keeping the unsteady term in the equations of motion prevents the occurrence of unrealistic predictions and permits to acknowledge and describe the unsteady behavior, which is a major feature of the process of vortex shedding, when it occurs. For instance, Tang & Ingham (1991) dropped the unsteady term of the Navier-Stokes equations and found steady state solutions for $Re = 60$ and 100 and $0 \leqslant \tilde{q} \leqslant 1$ where experimental and numerical evidence indicates that unsteady periodic flow takes place (e.g., Kang *et al.* 1999). The study of fully developed flows, where a periodic

‡ The reader is referred to the Fluent® 6.1's User's Guide for details about the numerical schemes and boundary conditions used by the package.

Mesh	Nodes	Cells	N_a	$\tilde{H}$	$\tilde{h}_a$ $\times 10^{-3}$	$\Delta\tilde{t}$
M50	22,080	21,920	160	50	2.50	0.02
M75	24,160	24,000	160	75	2.50	0.02
M100	25,760	25,600	160	100	2.50	0.02
M125	26,880	26,720	160	125	2.50	0.01/0.02
M150	28,000	27,840	160	150	2.50	0.02
M175	29,120	28,960	160	175	2.50	0.02
M125b	50,820	50,600	220	125	1.25	0.01

Table 18.12. *Properties of the meshes considered in the numerical simulations.*

unsteady state prevails, lies beyond the scope of this work. Here, the numerical experiments are focused on the steady state (i.e., fully developed non-periodic) flow motion.

In order to find a suitable position for the outer boundary, such that it appropriately approximates the real condition far from the surface of the rotating cylinder, different values of the $\tilde{H}$ parameter are considered ranging from 50 to 175 with increments of 25 units. For these grid sizes, a numerical study is performed for Re =400 and $\tilde{q}$ =5 and Re =1000 and $\tilde{q}$ =3 to determine the variation of the lift, drag and torque coefficients with the parameter $\tilde{H}$ (Figure 18.8). From this figure it is clear that beyond $\tilde{H}$ =75 the coefficients show an asymptotic behavior; then, it is selected $\tilde{H}$ =125 as the fixed radial position of the upstream and downstream arcs of circle of the outer boundary. This analysis is carried out with a dimensionless time step of $\Delta\tilde{t}$=0.02. This time step was chosen in agreement with Kang *et al.* (1999), while Mittal & Kumar (2003) used a dimensionless time step of 0.0125. Since the segregated method selected from the solver is implicit, no dependency on the time step occurs in terms of numerical stability. With respect to the spatial step size, we assign the same value recommended by Mittal & Kumar (2003) for the thickness or radial step size of the first layer of cells (i.e., cells attached to the wall), $\tilde{h}_a$=0.0025. A very fine mesh is used around the cylinder, with the size of the cells gradually increasing as the distance from the wall becomes larger. Following the approach of Chew *et al.* (1995), a rough calculation using the Blasius solution for the boundary layer thickness $\tilde{\delta}$ for flow past a flat plate but with the Reynolds number based on the peripheral velocity of the cylinder (i.e., $\tilde{\delta} \sim (\pi/\tilde{q}Re)^{1/2}$) indicates that this choice of the radial-spatial step size provides a good resolution of the boundary layer thickness. Table 18.12 gives the parameters defining the various meshes considered in this analysis; N_a is the number of nodes in the circumferential direction. Tests of the sensitivity of simulation results to mesh refinement were carried out using the meshes designated as M125 (lower $\Delta\tilde{t}$) and M125b in Table 18.12 for $Re = 400$ and $\tilde{q}$= 5 and $Re = 1000$ and $\tilde{q} = 3$. The lift and torque coefficients do not change much under mesh refinement but the drag coefficient does change. The changes in the drag coefficient seem relatively large because the coefficients are small, one or more orders of magnitude lower than the lift and torque coefficients (see Table 18.15). This issue is also addressed in the next section. As a result of this systematic study, the mesh M125 from Table 18.12 with $\Delta\tilde{t} = 0.02$ was selected for our numerical experiments. All the results presented in the forthcoming sections are computed using this mesh and time step. Figure 18.9 shows the structure of a typical mesh (for $\tilde{H} = 125$, mesh M125) which is more refined near the wall.

18.3.3 Results and dicussion

In this section we present the numerical results for streaming flow past a rotating circular cylinder for various Re and $\tilde{q}$. First, we validate our numerical setup by comparing results for selected cases with those from a previous publication. Then, the streamlines and vorticity contours are plotted and discussed. Next, the shape and extension of the vortical region around the rotating cylinder is addressed based on the vorticity field obtained from the numerical experiments. The prediction of the outer edge of the vortical region is accomplished imposing a cut off value such that the magnitude of the vorticity at this position approximates this critical value. The outmost curve that satisfy this criterion is found. We also present the drag and lift coefficients on the rotating cylinder as computed from the numerical simulations.

Re	$\tilde{q}$	Present study		Mittal & Kumar	
		C_L	C_D	C_L	C_D
200	3	-10.3400	0.0123	-10.3660	0.0350
200	4	-17.5820	-0.1240	-17.5980	-0.0550
200	5	-27.0287	0.0107	-27.0550	0.1680

Table 18.13. *Comparison between the lift and drag coefficients acting on the surface of the rotating cylinder, C_L and C_D, computed in the present study with the results of Mittal & Kumar (2003).*

18.3.3.1 Validation of the numerical approach

The first step is to validate the problem setup, the choice of numerical methods and mesh attributes by comparing results from our numerical simulations with results obtained from the literature, provided the same conditions are imposed. This comparison is performed with the numerical results of Mittal & Kumar (2003) for $Re = 200$ with $\tilde{q} = 4$ and 5 under the steady state condition. The outcomes included in the comparison are the lift and drag coefficients as defined in (18.3.4) as well as the dimensionless vorticity and pressure coefficient on the surface of the rotating circular cylinder. The dimensionless form of the vorticity is $\tilde{\omega} = 2a\omega/U_0$, while the pressure coefficient is defined as:

$$c_p = \frac{p - p_\infty}{\frac{1}{2}\rho U_0^2}, \tag{18.3.5}$$

where p_∞ represents the pressure as the radial coordinate r goes to infinity and p represents the pressure on the surface of the circular cylinder. In the numerical simulations, the reference pressure p_∞ is taken to be zero at the point where the axis $y = 0$ intercepts the upstream boundary. In our simulations, it is verified that the pressure tends closely to zero everywhere along the outer boundary of the domain. This result prevails since the free stream conditions are approached on the outer boundary.

Table 18.13 compares the lift and drag coefficients computed here with values given by Mittal & Kumar (2003). We have already noted that the agreement for the lift coefficient is good but discrepancies in the values of the drag coefficient are larger; the drag coefficients are so small that the relative errors are magnified. Figures 18.10 and 18.11 show that the dimensionless vorticity and pressure coefficient for Re = 200 with $\tilde{q} = 4$ and 5 are in good agreement with slightly less good agreement for $Re = 200$ and $\tilde{q} = 5$ where the pressure coefficient on the upper surface of the cylinder ($0° \leqslant \theta \leqslant 180°$) is slightly disturbed. This behavior may be related to the differences between our results and those of Mittal & Kumar for the drag coefficient. The pressure distribution around the surface of the cylinder contributes to the drag and the larger discrepancies are evident at large values of $\tilde{q}$. For the largest value of $\tilde{q}$ (= 5) the differences in the computational strategies used here and by Mittal & Kumar (2003) in terms of mesh shape and numerical schemes are most evident in the values of the drag. We do not know which computational approach is more accurate.

18.3.3.2 Vortical region thickness from the numerical flow field

After the evaluation of the numerical setup with results from the literature have been accomplished, we compute the flow field for flow past a rotating circular cylinder for $Re = 400$ with $\tilde{q} = 4$, $\tilde{q} = 5$ and $\tilde{q} = 6$ and for $Re = 1000$ and $\tilde{q}$ =3. In addition, the computations for $Re = 200$ with $\tilde{q}$ =4 and $\tilde{q} = 5$, already used for comparison with results presented in a previous publication, are also included in this data set. The choice of this set of Reynolds number Re and peripheral speed $\tilde{q}$ for the numerical simulations renders a gentle convergence to steady state fully developed flow when the unsteady incompressible Navier-Stokes equations are solved. For flow past a rotating circular cylinder, the boundary layer remains attached to the surface of the cylinder if the dimensionless peripheral velocity $\tilde{q}$ lies beyond a certain threshold so that separation is avoided and vortex shedding is suppressed. As mentioned above, this critical value of $\tilde{q}$ is a function of Re. Furthermore, the selected range of parameters Re and $\tilde{q}$ is likely to avoid large inertia effects that yield transition to turbulence and three dimensional effects. A reasonable assumption, based on literature review and previous computations (Chew *et al.* 1995), indicates taking $\tilde{q} \leqslant 6$ as a limiting value. However, this upper limit may be expected to be also a function of Re.

Figure 18.12 shows the streamline patterns for the various pairs of Re and $\tilde{q}$ considered in this investigation. Notice that the stagnation point lies above the cylinder, in the region where the direction of the free stream opposes the motion induced by the rotating cylinder. As the dimensionless peripheral speed at the surface of the cylinder increases, for a fixed Re, the region of close streamlines around the cylinder extends far from the wall and, as a consequence, the stagnation point moves upwards. For the lowest $\tilde{q} = 3$, the region of close streamlines become narrow and the stagnation point lies near the upper surface of the cylinder. The contours of positive and negative vorticity are presented in Figure 18.13. The positive vorticity is generated mostly in the lower half of the surface of the cylinder while the negative vorticity is generated mostly in the upper half. For the dimensionless peripheral speeds of $\tilde{q} = 3$ and 4 a zone of relative high vorticity stretch out beyond the region neighboring the rotating cylinder for $0° \leqslant \theta \leqslant 90°$, resembling "tongues" of vorticity. Increasing $\tilde{q}$, the rotating cylinder drags the vorticity so the "tongues" disappears and the contours of positive and negative vorticity appear wrapped around each other within a narrow region close to the surface. Based on the velocity and pressure fields obtained from the simulations for the various Re and $\tilde{q}$ considered, the next step in this numerical study is to identify the region where the vorticity effects are mostly confined. In a classical sense, the term boundary layer has been reserved for a narrow or thin region, attached to a solid surface, where the vorticity is non negligible. The concept of a boundary layer attached to a wall is linked to the idea of potential flow. Once the boundary layer has been delimited, the analysis follows by applying the relatively simple but still powerful theory of potential flow to approximate the external fluid motion. Nevertheless, this approximation may become inadequate when separation occurs. For flow past a stationary cylinder, separation is present near the downstream end of the cylinder even at Re as low as 5 (Panton 1984). In contrast, for flow past a rapidly rotating cylinder the separation of the boundary layer can be suppressed for a critical $\tilde{q}$ given Re. The Reynolds number based on the free stream velocity plays also an important role in the boundary layer analysis. In this investigation, a more general term, vortical region, is used to designate the region where the effects of viscosity are mostly restricted. The vortical region may extend relatively far from the surface where it is attached in opposition to the thinness implied in the classical boundary layer concept. A boundary layer is certainly a vortical region; however, a relatively thick vortical region may or may not be regarded as a boundary layer.

For the type of fluid motion considered in this investigation, the vortical region lies in the fluid zone enclosed between the surface of the rotating circular cylinder and a contour surrounding this solid cylinder, named the outer edge of the vortical region. Beyond this surface, the effect of vorticity is regarded as negligible. As a first approximation, we propose that the radial position of the outer edge of the vortical region is determined such that, for a given angular position, the vorticity magnitude is approximately 1% of the maximum value of the vorticity magnitude field. This ad hoc 1% criterion is then applied to a set of discrete angular positions around the rotating cylinder ($0° \leqslant \theta \leqslant 360°$), with a constant incremental angular step, using the flow field obtained from the numerical simulations. Therefore, the radial position of the outer edge of the vortical region as a discrete function of the azimuthal coordinate θ can be determined for every pair of Re and $\tilde{q}$. Since the 1% of the maximum vorticity magnitude criterion may be satisfied at multiple radial positions, for any given azimuthal position, the point with the largest $\tilde{r}$ among them is chosen to determine the outer edge of the vortical region. The radial position of the outer edge of the vortical region as a function of θ determines a non-constant thickness of the vortical region. Hence, a profile of this thickness as a function of the angular position can be generated.

For practical reasons, it is convenient to deal with a constant value of the radial position of the outer edge of the vortical region and then with a constant vortical region thickness. To find this uniform value, $\tilde{r}_\delta$, a straightforward choice is the average of the discrete set of radial positions that defined the edge of the vortical region as a function of θ from the previous methodology. Then, a uniform vortical region thickness, $\delta_{1\%}/a$, expressed in dimensionless fashion, is easily computed from the simple geometric formula:

$$\delta_{1\%}/a = 2\tilde{r}_\delta - 1. \tag{18.3.6}$$

Figure 18.14 shows the thickness of the vortical region as a function of the azimuthal coordinate as well as its average value for different pairs of Re and $\tilde{q}$. In all the cases considered, the vortical region is thick in the upper half of the cylinder ($0° \leqslant \theta \leqslant 180°$), where the fluid is retarded and the viscous effects are emphasized, while decreases its thickness in the lower half ($180° \leqslant \theta \leqslant 360°$), where the fluid is accelerated. For $Re = 200$ and 400 and $\tilde{q} = 4$ and $Re = 1000$ and $\tilde{q} = 3$ the graphs show a prominent peak in the region $45° \leqslant \theta \leqslant 90°$.

Re	$\tilde{q}$	$\tilde{r}_\delta$	$\delta_{1\%}/a$
200	4	0.771	0.541
200	5	0.685	0.369
400	4	0.695	0.390
400	5	0.630	0.260
400	6	0.605	0.210
1000	3	0.638	0.277

Table 18.14. *Radial position of the outer edge of the vortical region $\tilde{r}_\delta$ and thickness of the vortical region $\delta_{1\%}/a$ based on the 1% of the maximum vorticity magnitude criterion for various pairs of Re and $\tilde{q}$.*

This trend indicates that a region of vorticity magnitude higher than 1% of the maximum vorticity magnitude in the whole domain lies relatively far from the wall. For $Re = 200$ and $\tilde{q} = 5$ and $Re = 400$ and $\tilde{q} = 5$ and 6 the peak is replaced by a hump that reaches its maximum by $\theta = 90°$. This result indicates that the region of high vorticity has been wrapped around the cylinder as a consequence of the higher rotational speed. This is verified in Figure 18.13. In addition, the constant radial position of the vortical region edge $\tilde{r}_\delta$ and its corresponding vortical region thickness $\delta_{1\%}/a$ for various Re and $\tilde{q}$ are listed in Table 18.14. These results reveal that the vortical region thickness is far from negligible for all the cases. Moreover, it is shown in Table 18.14 that, as $\tilde{q}$ increases for a fixed Re, the average vortical region thickness $\delta_{1\%}/a$ decreases. By increasing the rotational speed of the cylinder, the local Reynolds number near its wall also increases and the inertia effects then become even more dominant than the viscosity effects, which turn out to be confined to a smaller region. A similar reasoning applies to the trend observed for a fixed $\tilde{q}$, where $\delta_{1\%}/a$ decreases as Re increases.

The outer edge of the vortical region from the 1% criterion as a function of the angular position θ for various pairs of Re and $\tilde{q}$ is presented in Figure 18.15 along with the vorticity contours. The corresponding outer edge of the vortical region for a uniform thickness $\delta_{1\%}/a$ is also included. Only levels of vorticity whose magnitude is greater than or equal 1% of the maximum vorticity magnitude in the fluid domain are shown. Since the position of the outer edge of the vortical region is obtained from a discrete set of angular positions, short sections of some iso-vorticity lines may lie outside the non-constant thickness vortical region. The large spikes presented in Figure 18.14 are also represented here, corresponding to the regions of vorticity magnitude greater than 1% that extend far from the cylinder in the interval $0° \leqslant \theta \leqslant 90°$.

It is recognized that the criterion set to define the outer edge of the vortical region is somewhat arbitrary. A new reasonable cut off value can be prescribed and substantial differences may be found in terms of the position of the outer edge of the vortical region, its thickness and its shape. Here, this preliminary criterion has been introduced to show that a region can be delimited where the effects of vorticity are circumscribed. This region is found to be attached to the rotating cylinder and its outer edge varies with the polar angle, for a sufficiently large rotational speed.

18.3.3.3 Drag and lift coefficients and pressure distribution from the numerical solution

The analysis of the forces that the fluid motion produces on the rotating cylinder has been a topic of major importance in aerodynamics. For streaming flow past a rotating cylinder, these forces have usually been presented in terms of two components mutually perpendicular, a component aligned with the free stream velocity vector, the drag force, and a component perpendicular to this direction, the lift force.

The numerical results for the total lift and drag coefficients corresponding to the forces that the fluid motion produces on the rotating circular cylinder are presented in Table 18.15. The contributions to these values from the pressure and the viscous shear stress are shown as well. The results for $Re = 200$ and $\tilde{q} = 4$ and 5 from Table 18.13 are included for completeness. The results in Table 18.15 indicate that the pressure lift coefficient C_{L_p} represents by far the largest contribution to the total lift C_L, in comparison with the shear stress lift coefficient C_{L_f}. The pressure and shear stress components of the lift force have the same direction of the total lift force, pointing toward the negative direction of the y axis in the current reference frame. By contrast, the pressure drag coefficient C_{D_p} and the shear stress drag coefficient C_{D_f} show a similar order of magnitude; however, these components of the total drag force point to opposite directions, with the pressure drag force pointing toward

Re	$\tilde{q}$	C_L	C_{L_p}	C_{L_f}	C_D	C_{D_p}	C_{D_f}
200	4	-17.5820	-16.9612	-0.6208	-0.1240	-0.7278	0.6038
200	5	-27.0287	-26.1826	-0.8460	0.0107	-0.8245	0.8352
400	4	-18.0567	-17.6095	-0.4472	-0.0836	-0.5341	0.4505
400	5	-27.0112	-26.4147	-0.5965	0.0100	-0.5912	0.6012
400	6	-33.7691	-33.0868	-0.6823	0.0136	-0.6677	0.6813
1000	3	-10.6005	-10.4085	-0.1920	-0.0155	-0.2129	0.1974

Table 18.15. *Numerical results for the lift and drag coefficients, C_L and C_D, corresponding to the forces acting on the cylinder. The decomposition of these values in their corresponding components from pressure (C_{L_p} and C_{D_p}) and viscous shear stress (C_{L_f} and C_{D_f}) are included.*

the upstream boundary (i.e., opposite to the direction of the free stream velocity). The net effect of the pressure and shear stress drag is a relatively small total drag coefficient whose magnitude is, in all the cases considered, within 1% of the magnitude of the total lift coefficient. For a constant value of Re, by increasing the peripheral velocity $\tilde{q}$ the magnitude of the total lift coefficient, as well as the pressure and shear stress lift coefficients increase. The same trend is observed with the magnitude of the pressure and shear stress drag coefficients. By keeping $\tilde{q}$ constant, the increase of Re yields an increase of the magnitude of the pressure lift coefficient but a decrease in the magnitude of the shear stress components of the lift and drag and the pressure drag coefficients. It is also of interest to observe and analyze the trend followed by the pressure distribution in the fluid domain, especially in the neighborhood of the rotating cylinder. Figure 18.16 shows the profiles of the pressure coefficient c_p as defined in (18.3.5) as a function of the radial coordinate for various Re and $\tilde{q}$. For every pair of Re and $\tilde{q}$, the c_p profiles for different angular positions are presented. The pressure coefficient has been computed from the pressure field obtained from the numerical simulations. The pressure coefficient as a result of the exact solution of the equations of motion for purely rotary flow due to the spinning cylinder embedded in an infinite fluid domain is presented as a reference level. The corresponding expression is

$$c_p = -\frac{\tilde{q}^2}{4\tilde{r}^2}, \tag{18.3.7}$$

independent of the angular position θ. In all the cases considered, this solution for c_p always lies inside the extreme profiles corresponding to $\theta = 90°$ and $\theta = 270°$. The graphs demonstrate that the pressure coefficient changes strongly near the wall, inside the vortical region, resembling the tendency described by the purely rotary flow solution, while becoming flat and tending slowly to zero as the radial coordinate $\tilde{r}$ approaches the outer boundaries. For a fixed peripheral speed $\tilde{q}$, it is observed that increasing Re has little effect on the pressure coefficient profiles. In contrast, for a fixed Re increasing $\tilde{q}$ expands the range of values that the pressure coefficient takes for a given radial position. For instance, this trend can be monitored on the surface of the rotating cylinder, $\tilde{r} = 0.5$, and at the outer edge of the vortical region, $\tilde{r} = \tilde{r}_\delta$, in Figure 18.16. This tendency may be addressed in the frame of the irrotational flow theory. The expression for the pressure coefficient distribution for potential flow past a circular cylinder with circulation (dimensionless) $\tilde{\Gamma}$ $(= \Gamma/2aU_0)$ is recalled here:

$$c_p = \frac{\cos 2\theta}{2\tilde{r}^2} - \frac{1}{16\tilde{r}^4} - \frac{\tilde{\Gamma}^2}{4\pi^2\tilde{r}^2} + \frac{\tilde{\Gamma}}{\pi}\sin\theta\left(\frac{1}{\tilde{r}} + \frac{1}{4\tilde{r}^3}\right). \tag{18.3.8}$$

It is clear from this expression that, for a fixed radial position, the amplitude of the $(\sin\theta)$ term increases when the circulation increases. Also, this theory predicts the decrease of the mean value of c_p when the circulation rises. The tendencies described by the classical irrotational theory for the pressure coefficient distribution are followed by the numerical solution obtained in this investigation.

The results from the numerical experiments carried out in this investigation as well as from previous publications represent reliable information that can be used to evaluate the prediction capabilities of theoretical approaches. In addition, theoretical models can be used to achieve a better understanding of the numerical results and to extract relevant information from the computations, which is not evident at first sight. For these purposes, the results from the numerical simulations have been compared to theoretical studies in sections 18.1 and 18.2.

Re	$\tilde{q}$	$\tilde{\mathcal{D}}$ from numerical simulations Inside VR	$\tilde{\mathcal{D}}$ from numerical simulations Outside VR	$\tilde{\mathcal{D}}$ from numerical simulations Total	$\tilde{\mathcal{D}}$ by WJa
200	4	1.1867	0.5594	1.7461	0.7213
200	5	1.2701	1.3000	2.5701	1.3001
400	4	0.6659	0.3881	1.0541	0.3718
400	5	0.7608	0.7191	1.4798	0.6547
400	6	0.8289	1.0533	1.8822	0.9997
1000	3	0.2322	0.1128	0.3451	0.0669

Table 18.16. *Comparison between the numerical results for the dissipation $\tilde{\mathcal{D}}$ determined through numerical integration of (18.3.10) and the predictions from (18.3.11) assuming irrotational flow of a viscous fluid in the entire domain for various Re and $\tilde{q}$. Computed contributions from inside and outside the vortical region (VR) are included. The radial position of the outer edge of the vortical region $\tilde{r}_\delta$ is determined by matching C_{D_p} given by the VCVPF analysis in §18.1 and the corresponding numerical results.*

18.3.3.4 Viscous dissipation

The dissipation represents the work done by the internal viscous stress. The dissipation may be defined by the following expression

$$\mathcal{D} \equiv \int_V 2\mu \mathbf{D} : \mathbf{D}\, dV. \tag{18.3.9}$$

In dimensionless form, this expression becomes,

$$\tilde{\mathcal{D}} \equiv \int_{\tilde{V}} \frac{2}{Re} \tilde{\mathbf{D}} : \tilde{\mathbf{D}}\, d\tilde{V}, \tag{18.3.10}$$

where $\tilde{\mathbf{D}}$ is the dimensionless rate of strain tensor. The evaluation of (18.3.10) is performed numerically using the velocity field determined from the numerical experiments. The domain is split into two zones: inside the vortical region and outside the vortical region. The dissipation values computed in each region add up to the total dissipation. In section 18.1, it is shown that the dissipation for the irrotational flow of a viscous fluid past a circular cylinder with circulation can be computed as

$$\tilde{\mathcal{D}} = \frac{8\pi}{Re}\left(1 + 2\tilde{r}_\delta^2 \tilde{Q}_\delta^2\right), \tag{18.3.11}$$

in dimensionless form.

Table 18.16 shows the computed results for the viscous dissipation obtained with (18.3.10) for the whole computational domain along with the predictions of (18.3.11). In this case, the radial position of the outer edge of the vortical region $\tilde{r}_\delta$ is determined by matching C_{D_p} computed in 18.1 with the corresponding numerical results. The results are presented for various Re and $\tilde{q}$. The contributions from inside and outside the vortical region to the dissipation as computed through (18.3.10) are included as well. The theoretical results included in Table 18.16 are closer to the viscous dissipation computed numerically in the region outside the vortical region than to the total numerical dissipation computed in the whole fluid domain. Moreover, the numerical viscous dissipation computed in the whole fluid domain is significantly greater than the theoretical prediction in all the cases. This trend may be explained by the fact that (18.3.11) is obtained by considering irrotational flow of a viscous fluid in the whole domain, thus neglecting the thickness of the vortical region. Then, the predicted values are anticipated to be lower than the computed values for the total viscous dissipation, which incorporates the contribution from the vortical region. Furthermore, for a fixed Re, the dissipation values computed from the numerical simulations and the predicted ones increase when $\tilde{q}$ increases. The trend is reversed for a fixed $\tilde{q}$ while increasing Re, yielding attenuation of the viscous effects.

18.3.4 Concluding remarks

We presented results from the numerical simulations of the two-dimensional incompressible Navier-Stokes equatios for streaming flow past a rotating circular cylinder. The numerical solution of the governing equation is accomplished by means of a commercial computational fluid dynamics package. The numerical experiments are performed for various pairs of Reynolds number based on the free stream velocity Re and dimensionless peripheral speed $\tilde{q}$, namely, $Re = 200$ with $\tilde{q} = 4$ and 5; $Re = 400$ with $\tilde{q} = 4$, 5 and 6, and $Re = 1000$ with $\tilde{q} = 3$. Based on the literature review and previous computations, these values are selected to avoid separation of the vortical region attached to the rotating cylinder, three dimensional effects and transition to turbulence. From the numerical solution, the vorticity field is computed and used to estimate, through an ad hoc criterion, the annular region with thickness $\delta_{1\%}/a$ around the cylinder where vorticity is significant.

We have shown that, with the choice of an effective thickness of the vortical layer, the simple modification of Glauert's boundary layer analysis and VCVPF lead to expressions that exhibit better general agreement with the numerical results than Glauert's original solution. This work provides a novel approach for future studies that attempt to focus on the analysis of boundary layers through computational fluid dynamics.

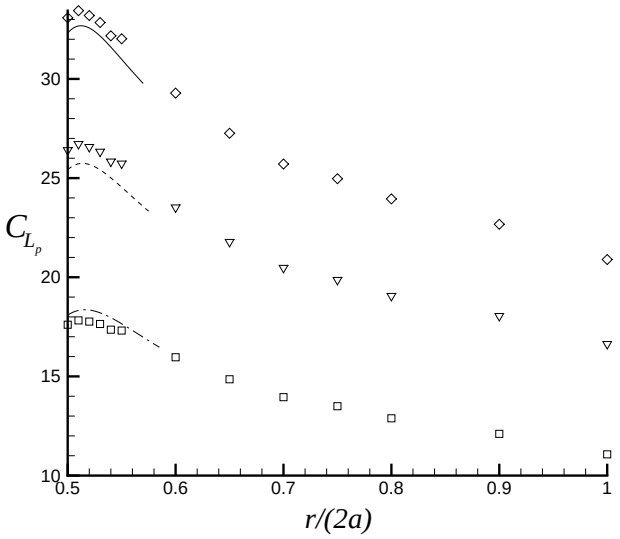

Fig. 18.6. Comparison of the coefficient for the pressure lift C_{L_p} as a function of the radial position for R_e=400. Our boundary layer analysis: dash-dotted line – q/U_0=4; dashed line – q/U_0=5; solid line – q/U_0=6. Numerical simulation: □ – q/U_0=4; ∇ – q/U_0=5; ♢ – q/U_0=6. C_{L_p} from our boundary layer analysis can only be computed inside the boundary layer: $a \leq r \leq a + \delta$; C_{L_p} from numerical simulation is plotted up to $r = 2a$.

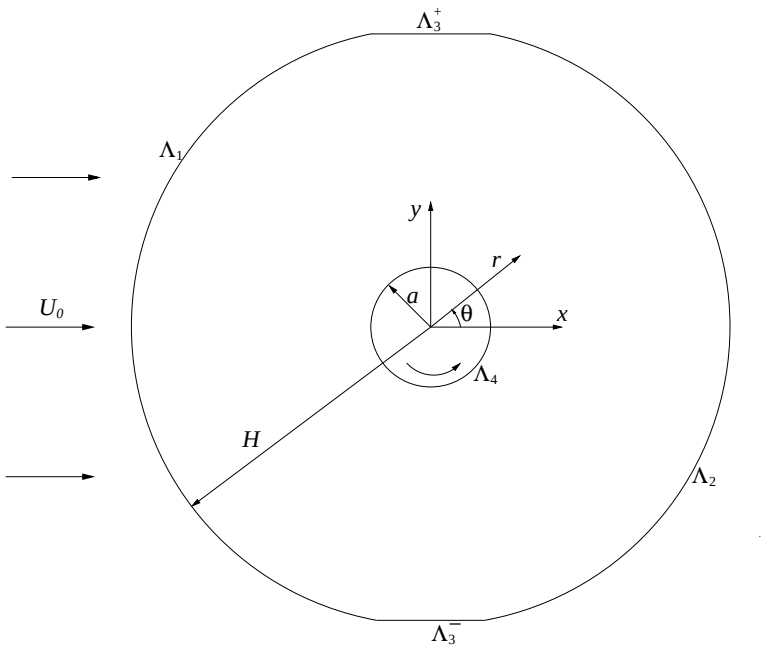

Fig. 18.7. Scheme of the computational domain showing the Cartesian and polar reference coordinate systems. The boundary conditions correspond to: Λ_1, inflow; Λ_2, outflow; Λ_3, zero-shear stress boundaries, and Λ_4, wall with prescribed velocity and no-slip condition.

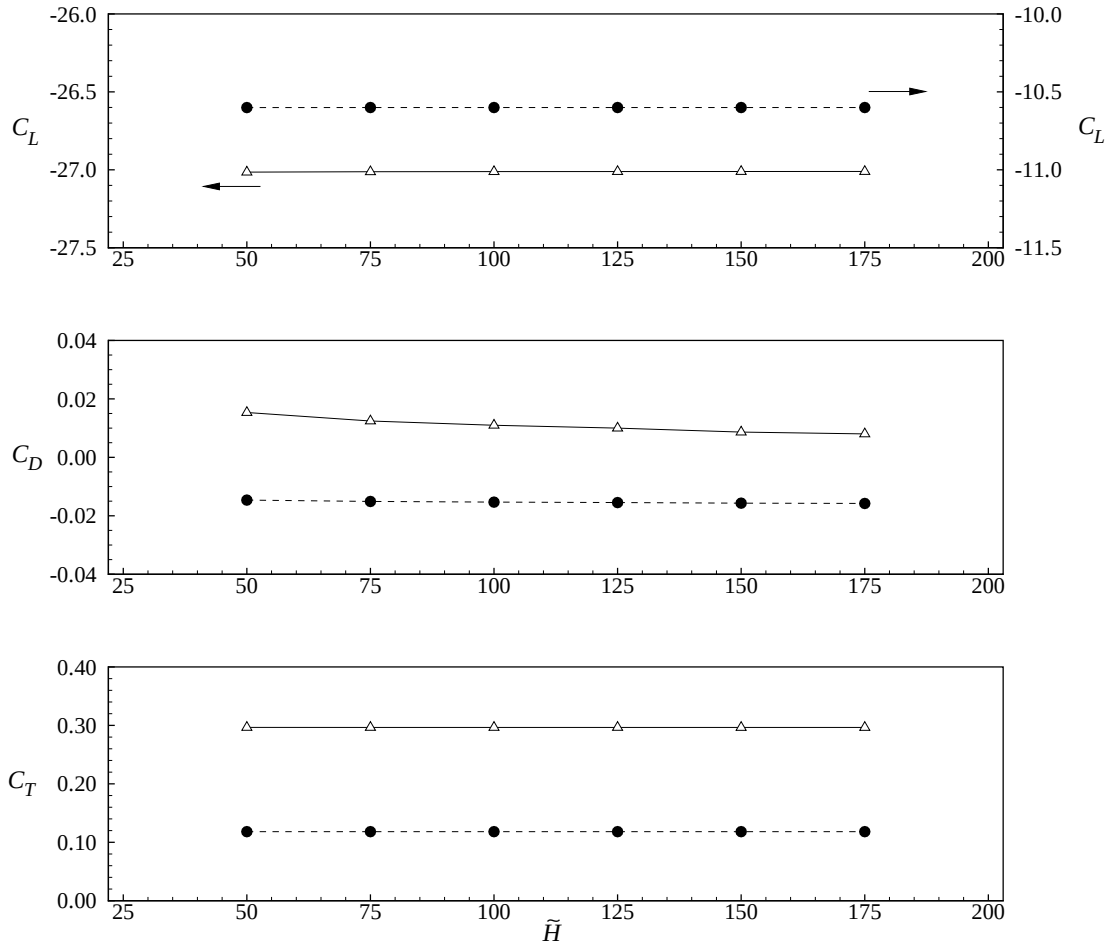

Fig. 18.8. Influence of the dimensionless position of the outer boundaries (inlet and outlet) $\tilde{H}$ on the lift, drag and torque coefficients for $Re = 400$ and $\tilde{q} = 5.0$ (solid line with $\triangle$) and $Re = 1000$ and $\tilde{q} = 3.0$ (dashed line with $\bullet$).

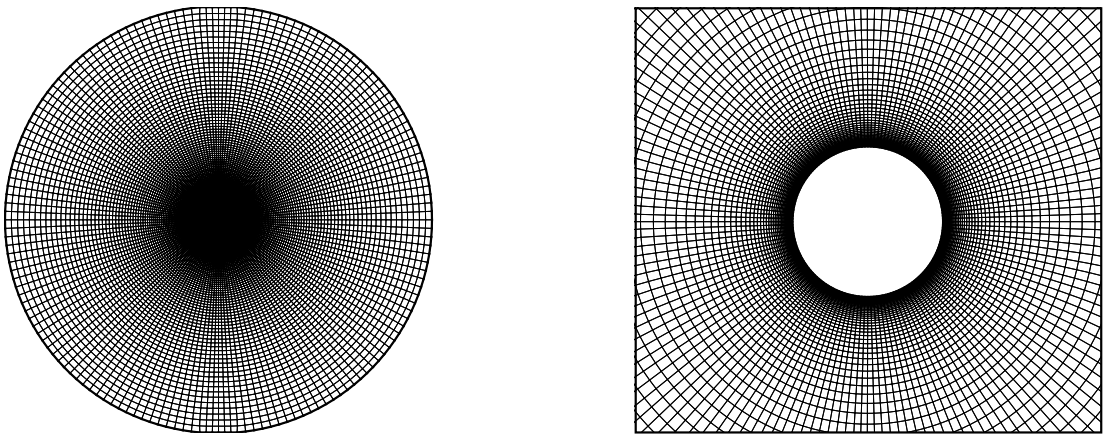

(a) Extended mesh.

(b) Close-up of the mesh around the cylinder.

Fig. 18.9. O-type mesh used in the numerical simulations (M125).

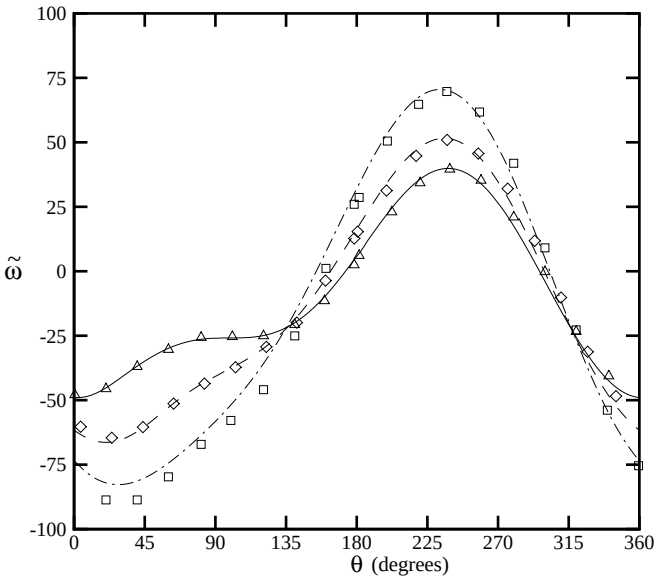

Fig. 18.10. Dimensionless vorticity profiles on the surface of the rotating cylinder for $Re = 200$. Present computations: solid line - $\tilde{q} = 3$; dashed line - $\tilde{q} = 4$; dash-dotted line - $\tilde{q} = 5$. Results of Mittal & Kumar (2003): △ - $\tilde{q} = 3$; ◇ - $\tilde{q} = 4$; □ - $\tilde{q} = 5$.

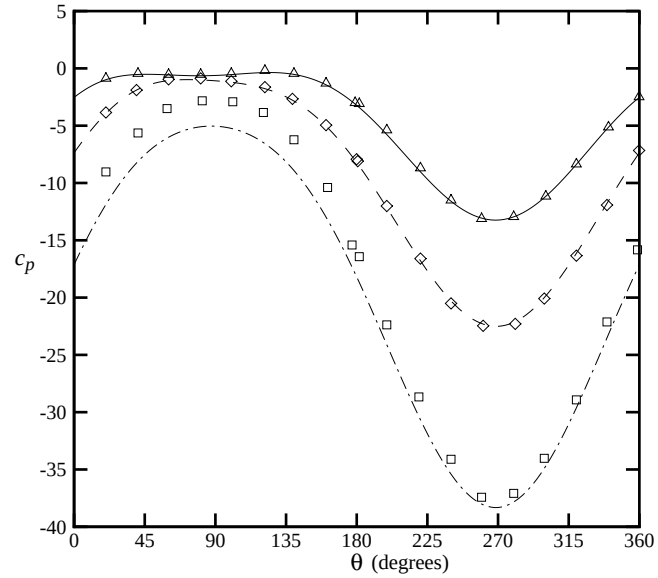

Fig. 18.11. Pressure coefficient profiles on the surface of the rotating cylinder for $Re = 200$. Present computations: solid line - $\tilde{q} = 3$; dashed line - $\tilde{q} = 4$; dash-dotted line - $\tilde{q} = 5$. Results of Mittal & Kumar (2003): △ - $\tilde{q} = 3$; ◇ - $\tilde{q} = 4$; □ - $\tilde{q} = 5$.

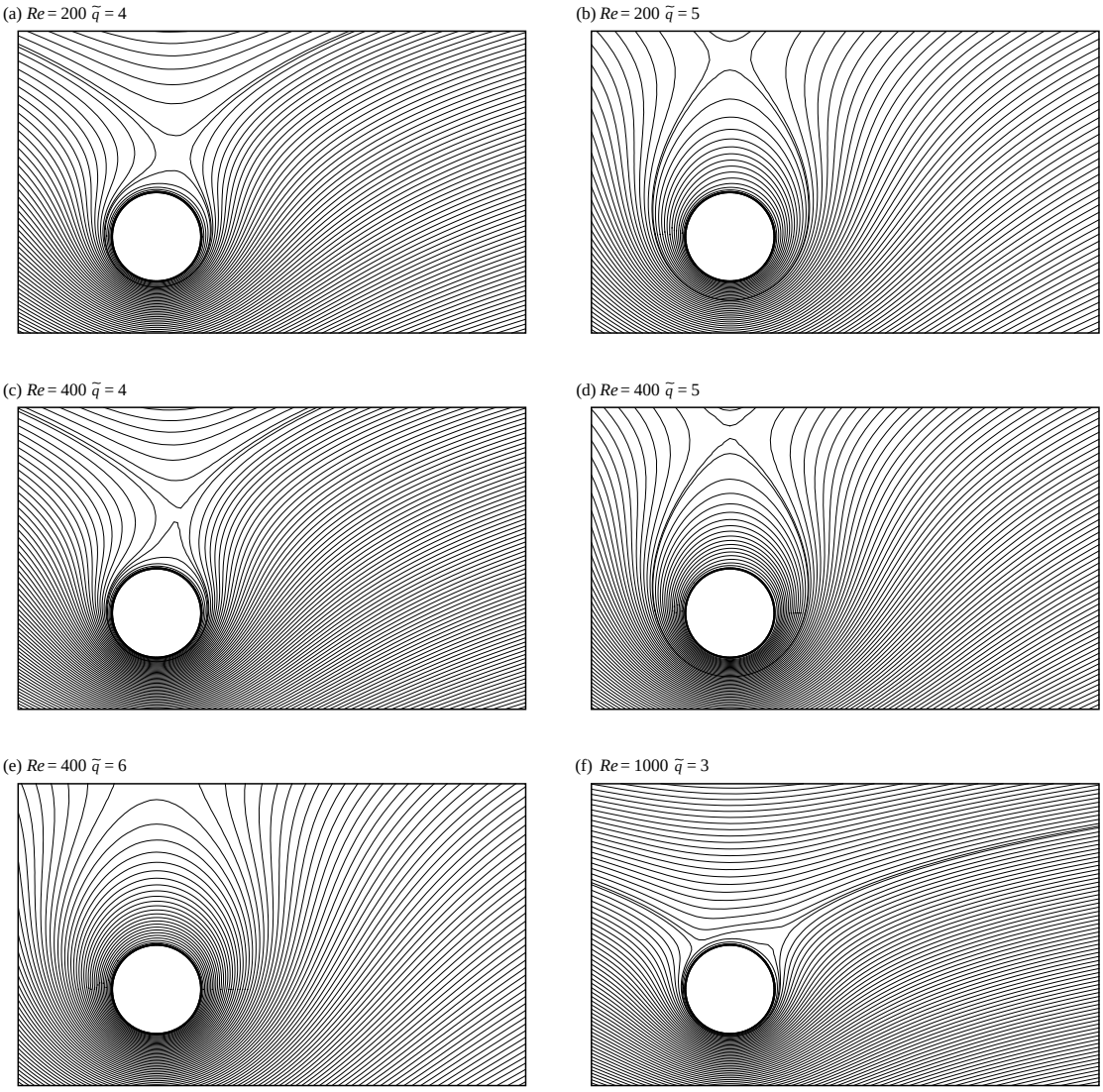

Fig. 18.12. Streamlines for various pairs of Re and $\tilde{q}$. The rotation of the cylinder is counter-clockwise while the streaming flow is from left to right. The stagnation point lies above the cylinder. The stagnation point moves upwards as the peripheral speed $\tilde{q}$ increases for a fixed Re.

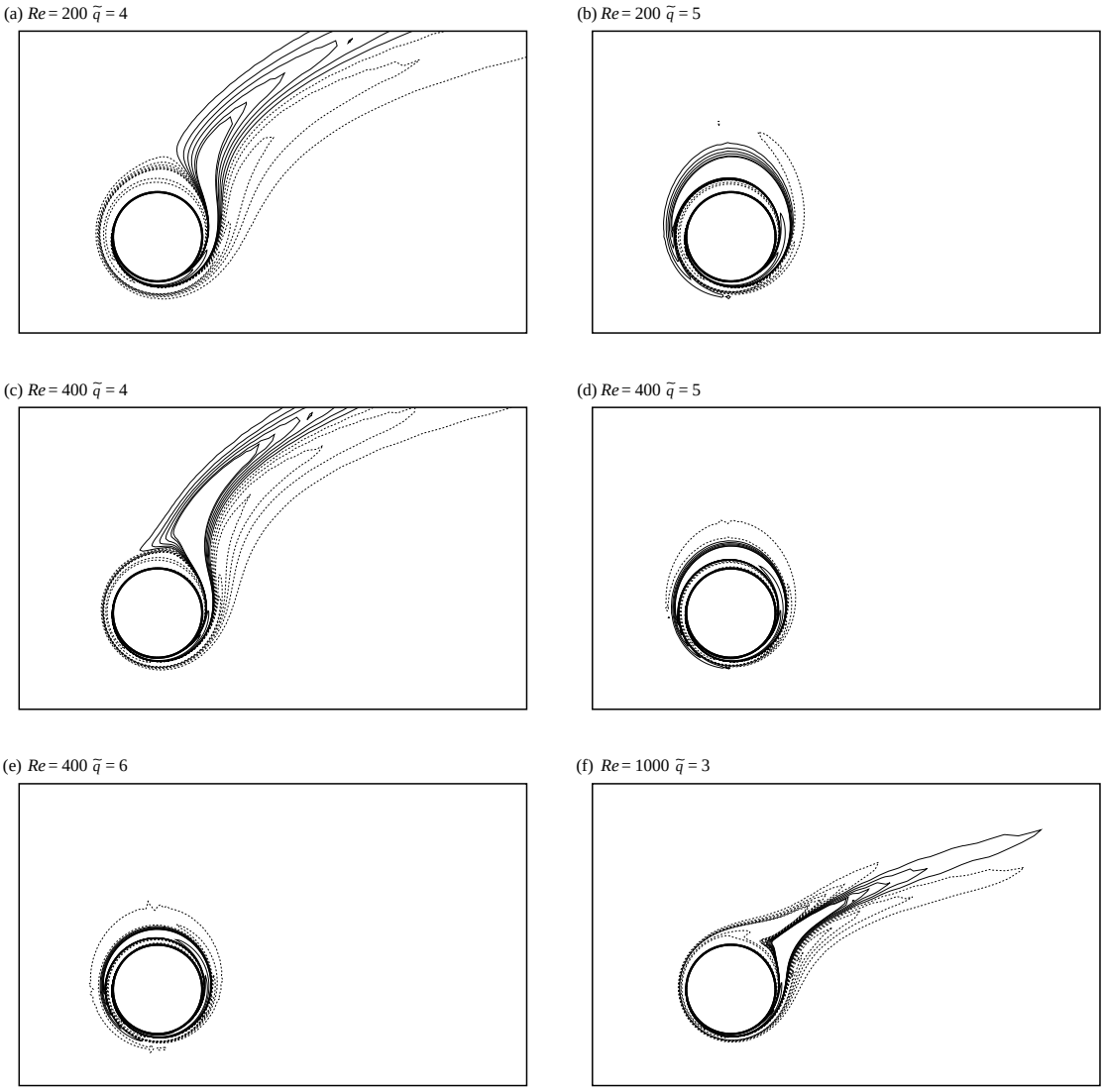

Fig. 18.13. Vorticity contours for various pairs of Re and $\tilde{q}$. The negative vorticity is shown as dashed lines. The rotation of the cylinder is counter-clockwise while the streaming flow is from left to right.

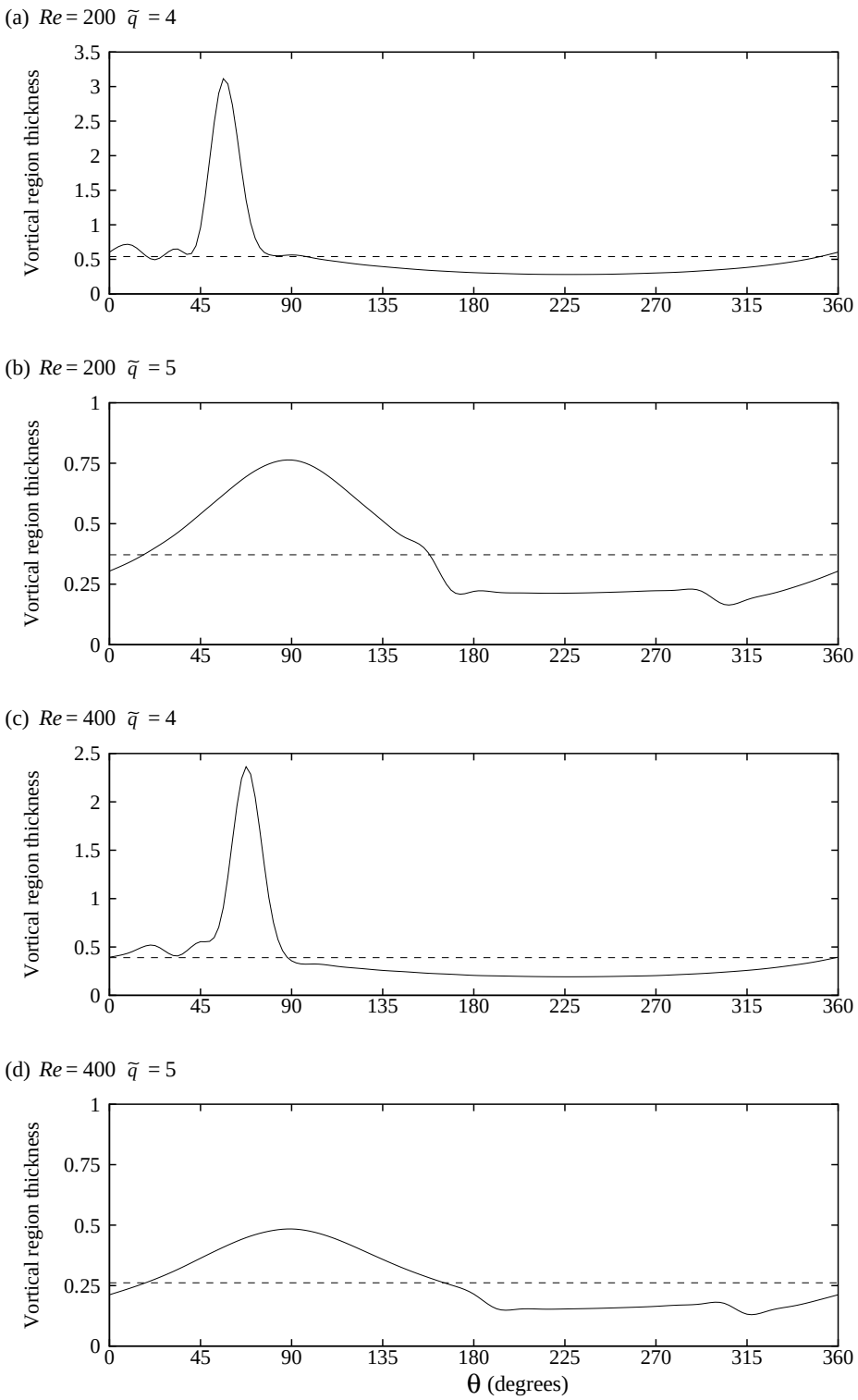

Fig. 18.14. Caption in the next page.

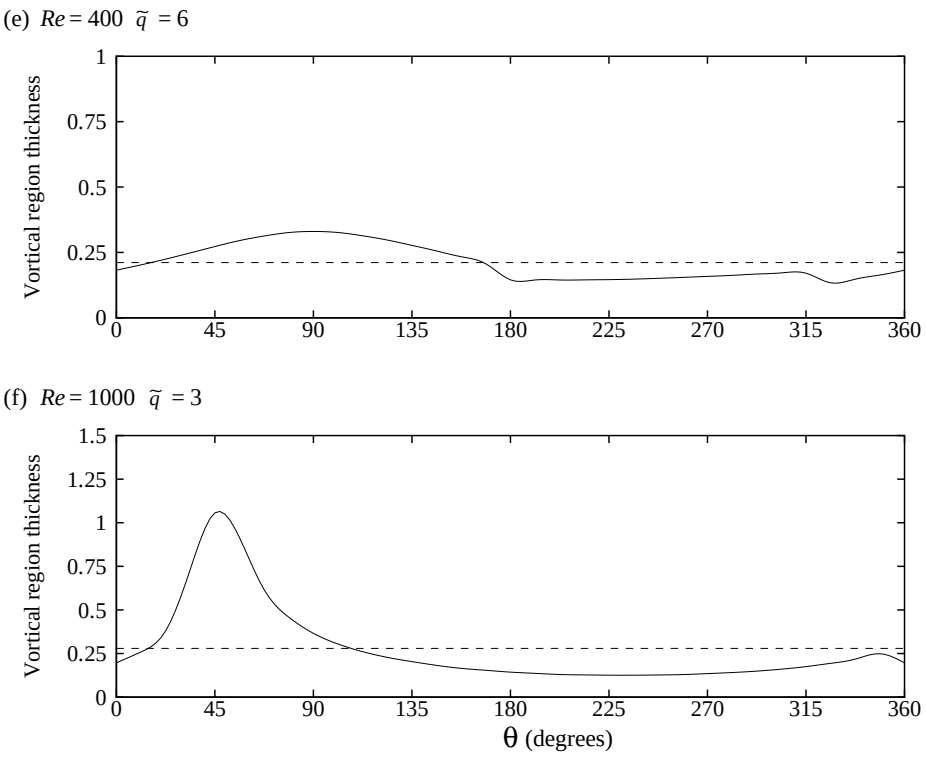

Fig. 18.14. Variable vortical region thickness as a function of the angular position θ (solid line) for various pairs of Re and $\tilde{q}$ obtained applying the 1% criterion. In addition, the uniform vortical region thickness $\delta_{1\%}/a$ (dashed line) computed as the average of the profile is included.

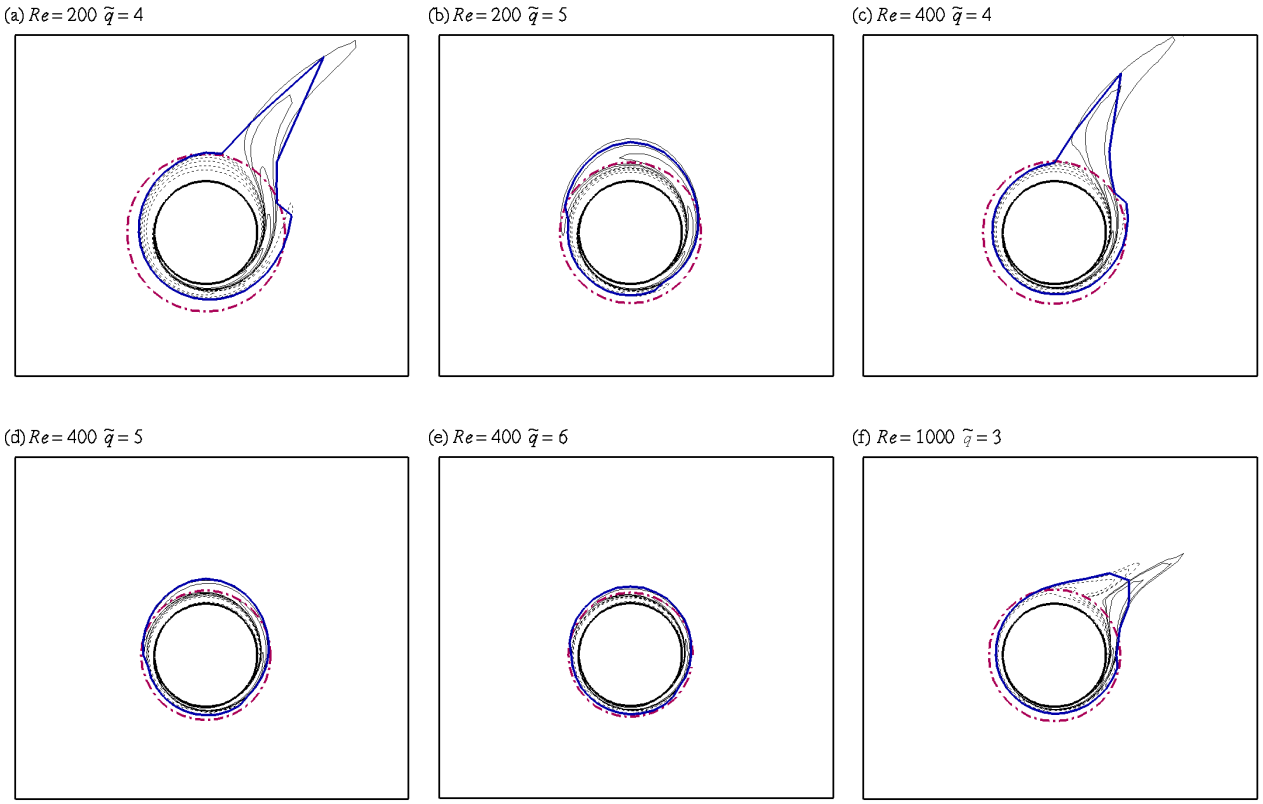

Fig. 18.15. Position of the outer edge of the vortical region based on the 1% criterion. The thick-solid line represents the edge of the vortical region with variable thickness. The thick dash-dotted line represents the edge of the vortical region with uniform thickness $\delta_{1\%}/a$. The thin-solid lines represent contours of positive vorticity while the thin-dashed lines represent contours of negative vorticity. The contours only show levels of vorticity with magnitude greater than or equal to 1% of the maximum vorticity magnitude in the fluid domain. The rotation of the cylinder is counter-clockwise while the streaming flow is from left to right.

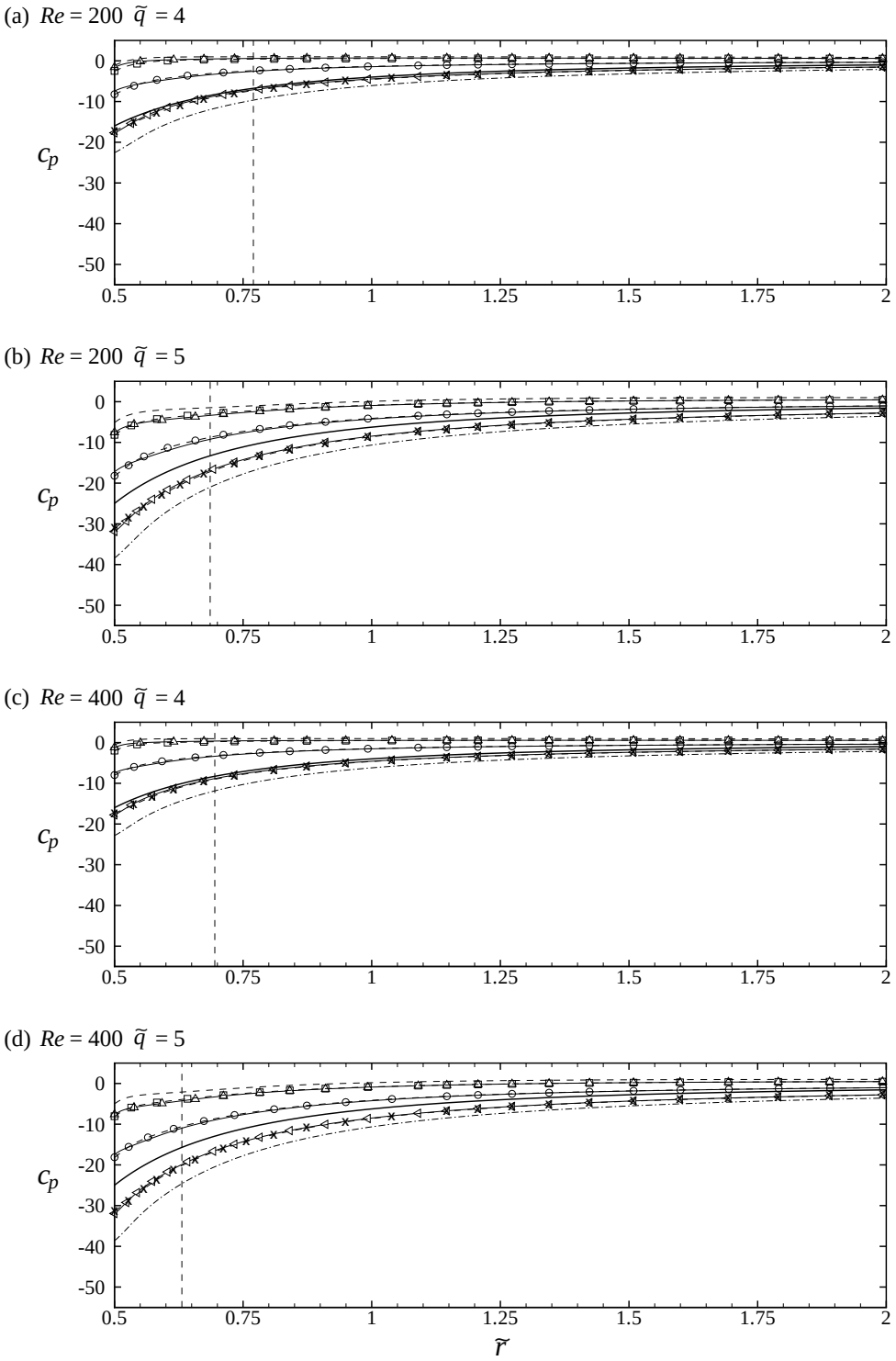

Fig. 18.16. Caption on the next page.

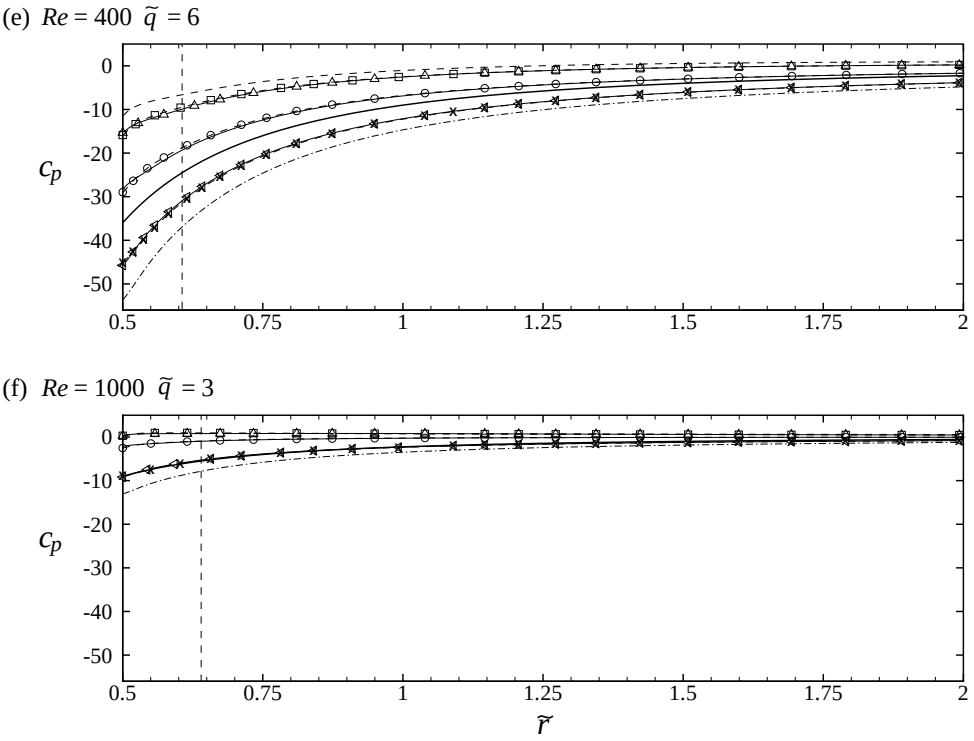

Fig. 18.16. Pressure coefficient c_p as a function of the radial position $\tilde{r}$ from the surface of the rotating cylinder for various pairs of Re and $\tilde{q}$ for a fixed angle θ: 0° - thin solid line; 45° - solid line with △; 90° - dashed line; 135° - dashed line with □; 180° - dashed line with ○; 225° - solid line with ◁; 270° - dashed-dotted line; 315° - dashed line with ×. The pressure coefficient profile given in (18.3.7) from the exact solution of the equations of motion for a purely rotary flow due to the spinning of the cylinder under the absence of the free stream is also presented (thick solid line). This pressure profile is independent of θ. The average position of the outer edge of the vortical region $\tilde{r}_\delta$ corresponding to the 1% criterion is included (vertical dashed line).

19

Irrotational flows which satisfy the compressible Navier-Sokes equations.

If one assumes that the flow is isentropic, the body force has a potential χ, the dynamic and kinematic viscosity ν are constant, then the compressible Navier Stokes equations become

$$\frac{\partial \boldsymbol{u}}{\partial t} + \boldsymbol{u} \cdot \nabla \boldsymbol{u} = \nabla \int \mathrm{d}p/\rho\,(p) + \nu \nabla \boldsymbol{u} + \frac{1}{3}\nu \nabla \mathrm{div}\boldsymbol{u} - \nabla \chi \tag{19.0.1}$$

and

$$\frac{\mathrm{d}\rho}{\mathrm{d}t} + \rho \mathrm{div}\boldsymbol{u}.$$

The vorticity equation for $\boldsymbol{\omega} = \mathrm{curl}\boldsymbol{u}$ is satisfied by $\boldsymbol{\omega} = 0$. Putting $\boldsymbol{u} = \nabla\phi$, we find that

$$\frac{\partial \phi}{\partial t} + \frac{1}{2}\left|\nabla\phi\right|^2 + \chi + \int \frac{\mathrm{d}p}{\rho} - \frac{4}{3}\nu\nabla^2\phi = 0 \tag{19.0.2}$$

and

$$\frac{\mathrm{d}\rho}{\mathrm{d}t} + \rho\nabla^2\phi = 0 \tag{19.0.3}$$

Following conventional procedures of gas dynamics, we may eliminate explicit dependence on ρ from this system

$$C^2\nabla^2\phi = \boldsymbol{u}\cdot(\boldsymbol{u}\cdot\nabla\boldsymbol{u}) + \frac{\partial}{\partial t}\left[\frac{\partial\phi}{\partial t} + \left|\boldsymbol{u}\right|^2\right] - \frac{4}{3}\nu\frac{\mathrm{d}}{\mathrm{d}t}\nabla^2\phi \tag{19.0.4}$$

where $\mathrm{d}/\mathrm{d}t$ is the substantial derivative and C is the speed of sound. The viscous term is large when $Ul/\nu = R_e$ is small, where U and l are the free stream velocity and a body diameter.

The molecular and kinematic viscosity are not constant in general flows; isentropic flow cannot be achieved because viscous dissipation generates entropy* and entropy generation generates vorticity. For gases, R_e is typically large, but if we add one more assumption, even more severe than others, that ν is the eddy viscosity of a turbulent gas flow, then we could expect to see large effects of the turbulent viscosity on the gas flow.

Equation (19.0.4) is exact when $\nu = 0$, it is exact for the acoustic wave problem described below and it is exact for the analysis of the effects of viscosity on shock structure in the one dimensional approximation. For potential flow solutions of the Navier Stokes equations it is necessary that $\mathrm{curl}\boldsymbol{u} = 0$ is a solution (see Joseph and Liao 1994a) of the vorticity equation. The gradients of density and viscosity which are spoilers for the general vorticity equation do not enter into the equations which perturb the state of rest with uniform pressure p_0 and density ρ_0.

19.1 Acoustics

The stress for a compressible viscous fluid is given by

$$T_{ij} = -\left(p + \frac{2}{3}\mu\,\mathrm{div}\,\boldsymbol{u}\right)\delta_{ij} + \mu\left(\frac{\partial u_i}{\partial x_j} + \frac{\partial u_j}{\partial x_i}\right). \tag{19.1.1}$$

Here, the second coefficient of viscosity is selected so that $T_{ii} = -3p$. (The results to follow will apply also to the case when other choices are made for the second coefficient of viscosity.)

The equations of motion are given by

$$\rho\left(\frac{\partial \boldsymbol{u}}{\partial t} + \boldsymbol{u}\cdot\nabla\boldsymbol{u}\right) = \operatorname{div}\mathbf{T} \tag{19.1.2}$$

together with

$$\frac{\partial \rho}{\partial t} + \boldsymbol{u}\cdot\nabla\rho + \rho\operatorname{div}\boldsymbol{u} = 0. \tag{19.1.3}$$

To study acoustic propagation, these equations are linearized; putting

$$[\boldsymbol{u},\ p,\ \rho] = [\boldsymbol{u}',\ p_0 + p',\ \rho_0 + \rho'] \tag{19.1.4}$$

where $\boldsymbol{u}'$, p' and ρ' are small quantities, we get

$$T_{ij} = -\left(p_0 + p' + \frac{2}{3}\mu_0\operatorname{div}\boldsymbol{u}'\right)\delta_{ij} + \mu_0\left(\frac{\partial u_i'}{\partial x_j} + \frac{\partial u_j'}{\partial x_i}\right) \tag{19.1.5}$$

$$\rho_0\frac{\partial \boldsymbol{u}'}{\partial t} = -\nabla p' + \mu_0\left(\nabla^2\boldsymbol{u}' + \frac{1}{3}\nabla\operatorname{div}\boldsymbol{u}'\right) \tag{19.1.6}$$

$$\frac{\partial \rho'}{\partial t} + \rho_0\operatorname{div}\boldsymbol{u}' = 0 \tag{19.1.7}$$

where p_0, ρ_0 and μ_0 are constants. For acoustic problems, we assume that a small change in ρ induces small changes in p by fast adiabatic processes; hence

$$p' = C_0^2\rho' \tag{19.1.8}$$

where C_0 is the speed of sound.

Forming now the curl of (19.1.6), we find that

$$\rho_0\frac{\partial \boldsymbol{\zeta}}{\partial t} = \mu_0\nabla^2\boldsymbol{\zeta}, \quad \boldsymbol{\zeta} = \operatorname{curl}\boldsymbol{u}'. \tag{19.1.9}$$

Hence $\boldsymbol{\zeta} = 0$, is a solution of the vorticity equation and we may introduce a potential

$$\boldsymbol{u}' = \nabla\phi. \tag{19.1.10}$$

Combining next (19.1.10) and (19.1.6), we get

$$\nabla\left[\rho_0\frac{\partial \phi}{\partial t} + p' - \frac{4}{3}\mu_0\nabla^2\phi\right] = 0. \tag{19.1.11}$$

The quantity in the bracket is equal to an arbitrary function of the time which may be absorbed in ϕ.

A viscosity dependent Bernoulli equation

$$\rho_0\frac{\partial \phi}{\partial t} + p' - \frac{4}{3}\mu_0\nabla^2\phi = 0 \tag{19.1.12}$$

is implied by (19.1.11). The stress (19.1.5) is given in terms of the potential ϕ by

$$T_{ij} = -\left(p_0 - \rho_0\frac{\partial \phi}{\partial t} + 2\mu_0\nabla^2\phi\right)\delta_{ij} + 2\mu_0\frac{\partial^2\phi}{\partial x_i\partial x_j}. \tag{19.1.13}$$

To obtain the equation satisfied by the potential ϕ, we eliminate ρ' in (19.1.7) with p' using (19.1.8), then eliminate $\boldsymbol{u}' = \nabla\phi$ and p' in terms of ϕ using (19.1.12) to find

$$\frac{\partial^2\phi}{\partial t^2} = \left(C_0^2 + \frac{4}{3}\,v_0\frac{\partial}{\partial t}\right)\nabla^2\phi \tag{19.1.14}$$

where the potential ϕ depends on the speed of sound and the kinematic viscosity $v_0 = \mu_0/\rho_0$.

A dimensionless form for the potential equation (19.1.14)

$$\frac{\partial^2\phi}{\partial T^2} = \left(1 + \frac{\partial}{\partial T}\right)\nabla^2\phi, \quad \nabla^2\phi = \frac{\partial^2\phi}{\partial X^2} + \frac{\partial^2\phi}{\partial Y^2} + \frac{\partial^2\phi}{\partial Z^2} \tag{19.1.15}$$

arises from a change of variables

$$t = \frac{4v_0}{3C_0^2}T, \quad \boldsymbol{x} = \frac{4}{3}\frac{v_0}{C_0}\boldsymbol{X}. \tag{19.1.16}$$

The classical theory of sound (see Landau and Lifshitz 1987, chap. VIII) is governed by a wave equation, which may be written in dimensionless form as

$$\frac{\partial^2\phi}{\partial T^2} = \nabla^2\phi. \tag{19.1.17}$$

The time derivative on the right of (19.1.15) leads to a decay of the waves not present in the classical theory. Many if not all of the results obtained with (19.1.17) may be redone, using (19.1.15).

The simplest problem in the theory of sound waves (see Landau and Lifshitz 1987, p 253) is the case of Plane monochromatic travelling waves. The one-dimensional version of (19.1.15)

$$\frac{\partial^2\phi}{\partial T^2} = \left(1 + \frac{\partial}{\partial T}\right)\frac{\partial^2\phi}{\partial X^2} \tag{19.1.18}$$

can be solved by separation of variables, $\phi = F(T)G(X)$. We obtain

$$\frac{F''}{F + F'} = \frac{G''}{G} = -k^2. \tag{19.1.19}$$

If $k^2 > 4$, the solution is

$$\phi = \left(A\mathrm{e}^{-\omega_1 T} + B\mathrm{e}^{-\omega_2 T}\right)\cos\left(-kX + \alpha\right) \tag{19.1.20}$$

where A, B and α are undetermined constants and

$$\begin{bmatrix} \omega_1 \\ \omega_2 \end{bmatrix} = \frac{k^2}{2}\begin{bmatrix} 1 \\ 1 \end{bmatrix} + \frac{1}{2}\begin{bmatrix} \sqrt{k^4 - 4k^2} \\ -\sqrt{k^4 - 4k^2} \end{bmatrix}. \tag{19.1.21}$$

The solution is a standing periodic wave with a decaying amplitude.

If $k^2 < 4$, the solution is

$$\phi = \mathrm{e}^{-\frac{k^2}{2}T}\begin{bmatrix} A\cos\left(-kX - \frac{1}{2}\left(4k^2 - k^4\right)^{1/2}T + \alpha\right) \\ +B\cos\left(-kX + \frac{1}{2}\left(4k^2 - k^4\right)^{1/2}T + \alpha\right) \end{bmatrix} \tag{19.1.22}$$

represents decaying waves propagating to the left and right. Travelling plane wave solutions which are periodic in T and grow or decay in X are also easily derived by separating variables.

19.2 Liquid jet in a high Mach number air stream

For spherically symmetric waves,

$$\frac{\partial^2\phi}{\partial T^2} = \left(1 + \frac{\partial}{\partial T}\right)\frac{1}{R^2}\frac{\partial}{\partial R}\left(R^2\frac{\partial\phi}{\partial R}\right) \tag{19.2.1}$$

and, following Landau and Lifshitz (1987, pg. 269) we note that

$$\psi(R, T) = R\phi \tag{19.2.2}$$

satisfies equation (19.1.18) for plane waves with R replacing X. It follows then that the solutions (19.1.20), (19.1.22) and (19.2.1) hold for spherically symmetric waves when X is replaced with R and $\phi(X, T)$ with $R\phi(R, T)$.

The properties of these and many other solutions to equation (19.1.15) are for future research. For the present,

we indicate in Table 19.1 representative values of physical parameters of sound waves which are suppressed in the dimensionless version of our problem. The properties of liquids may be useful in studies of cavitation of liquids due to ultrasound.

Table 19.1. *Representative dimensional parameters of sound waves.* $\frac{4v_0}{3C_0^2}$ *and* $\frac{4}{3}\frac{v_0}{C_0}$ *are time and length scales respectively (equation (19.1.16)).* $k\frac{3C_0}{4v_0}$ *is the cut-off wave number and* $w_1\frac{3C_0^2}{4v_0} = w_2\frac{3C_0^2}{4v_0}$ *is the frequency when* k *is the cut-off wave number (equation (19.2.1)).* $k_1\frac{3C_0}{4v_0}$ *and* $k_2\frac{3C_0}{4v_0}$ *are the wave numbers when the frequency of the sound wave* $w\frac{3C_0^2}{4v_0} = 10^9\ s^{-1}$ *(equation (19.2.2)). The values are calculated using the properties of the liquids at 15° C :* $\rho_{\rm w} = 1\ g/cm^3$, $\mu_{\rm w} = 0.0114\ g/cm\ sec$, $C_{\rm w} = 1.48 \times 10^5\ cm/sec$ *for water;* $\rho_{\rm w} = 1.26\ g/cm^3$, $\mu_{\rm w} = 23.3\ g/cm\ sec$, $C_{\rm w} = 1.9 \times 10^5\ cm/sec$ *for glycerin.*

	$\frac{4v_0}{3C_0^2}$ (sec)	$\frac{4}{3}\frac{v_0}{C_0}$ (cm)	$k\frac{3C_0}{4v_0}(\mathrm{cm}^{-1})$	$w_1\frac{3C_0^2}{4v_0} = w_2\frac{3C_0^2}{4v_0}(\mathrm{sec}^{-1})$	$k_1\frac{3C_0}{4v_0}(\mathrm{cm}^{-1})$	$k_2\frac{3C_0}{4v_0}(\mathrm{cm}^{-1})$
Water	6.94×10^{-13}	1.03×10^{-7}	1.95×10^7	2.88×10^{12}	2.34	6.76×10^3
Glycerin	6.83×10^{-10}	1.30×10^{-4}	1.54×10^4	2.93×10^9	1.41×10^3	4.57×10^3

19.3 Liquid jet in a high Mach number air stream

The instability of circular liquid jet immersed in a coflowing high velocity airstream is studied assuming that the flow of the viscous gas and liquid is irrotational. The basic velocity profiles are uniform and different. The instabilities are driven by Kelvin-Helmholtz instability due to a velocity difference and neckdown due to capillary instability. Capillary instabilities dominate for large Weber numbers. Kelvin-Helmholtz instability dominates for small Weber numbers. The wave length for the most unstable wave decreases strongly with the Mach number and attains a very small minimum when the Mach number is somewhat larger than one. The peak growth rates are attained for axisymmetric disturbances ($n = 0$) when the viscosity of the liquid is not too large. The peak growth rates for the first asymmetric mode ($n = 1$) and the associated wave length are very close to the $n = 0$ mode; the peak growth rate for $n = 1$ modes exceeds $n = 0$ when the viscosity of the liquid jet is large. The effects of viscosity on the irrotational instabilities are very strong. The analysis predicts that breakup fragments of liquids in high speed air streams may be exceedingly small, especially in the transonic range of Mach numbers.

19.3.1 Introduction

The problem of an inviscid liquid jet in an inviscid compressible airstream was studied by Chang & Russel (1965), Nayfeh & Saric (1973), Zhou & Lin (1992) and Li & Kelly (1992). Chawla (1975) studied the stability of a sonic gas jet submerged in a liquid. Chang & Russel (1965) and Nayfeh & Saric (1973) consider temporal instability and found that a singularity in the growth rate occurs as the Mach number tends to unity. Chawla (1975) did not find a singular growth rate but he restricted his attention to Mach number one ($M = 1$). Li & Kelly (1992) found that the growth rates reach a sharp maximum when the gas velocity is slightly larger than the one giving $M = 1$ for both axisymmetric and the first non-axisymmetric mode of instability. Lin (2003) cites Li & Kelly (1992) for the growth rate near $M = 1$ in the case of temporal stability.

Funada, Joseph, Saitoh and Yamashita (FJSY, 2006) extended the theory of viscous potential flow of a viscous compressible gas given by Joseph (2003) to the case of perturbations in a compressible gas moving with uniform velocity. We derive a dispersion relation for the perturbations which depend on all the material properties of the incompressible liquid and compressible gas. The effects of shear are neglected, consistent with the assumption that the basic flow can support a discontinuous velocity. We find a sharply peaking growth rate at slightly supersonic value of the gas Mach number under the conditions that Li & Kelly (1992) find steep changes for both axisymmetric and first asymmetric modes. The analysis of Li & Kelly (1992) differs from the one given here in the way that the isentropic flow is represented. They assume that $\mathrm{d}p/\mathrm{d}\rho = c^2$, as in isentropic flow, but

they do not account for the usual isentropic relations which tie the density, pressure and velocity together as in our equation (19.3.13).

The first application of viscous potential flow to the problem of capillary instability was done by Funada & Joseph (2002). The problem of combined Kelvin-Helmholtz and capillary instability for an incompressible liquid and gas was done by Funada *et al.* (2004) who treated also the problem of convective and absolute instability in a comprehensive manner.

The effects of compressibility are very important for transonic and supersonic flow as has already been noted by Lin (2003). These effects include very great increases in growth rates and very sharp decreases in the wave length for maximum growth. This feature may possibly play a role in the breakup of liquid droplets into fine drops must observed in shock tube and wind tunnel experiments (Engel (1958), Joseph *et al.* (1999), Joseph *et al.* (2002), Theofanous *et al.* (2003), Varga, Lasheras & Hopfinger 2003).

Chen & Li (1999) did a linear stability analysis for a viscous liquid jet issued into an inviscid moving compressible gas medium. Their analysis differs from ours; they do not assume that motion of the liquid is irrotational; they give results only for the case in which the gas is at rest so that the effects of the basic flow gas velocity is not connected to the basic flow density and pressure as in the case of isotropic flow considered here. They do not compute growth rates for temporal instabilities for supersonic values $M > 1$. Their growth rate curves do not exhibit the same great increases in transonic and supersonic flow found by other authors and here.

The assumption that the gas is inviscid is not justified for jets of liquids into air especially when the air velocity is large. What matters here is the ratios of kinematic viscosities (see equation (4.2) in Funada *et al.* (2004) and figure 4 in Funada & Joseph (2001)) and the kinematic viscosity of high speed air in isentropic flow can be much greater than the kinematic viscosity of water.

Experimental results on liquid jets in high speed gas suitable for comparison with this and other analytical studies are not available. The coaxial jet experiments of Varga, Lasheras & Hopfinger 2003 discussed in section 19.3.12 is suitable, but they do not present data for transonic and supersonic conditions. Dunne & Cassen (Dunne & Cassen (1954), Dunne & Cassen (1956)) did some experiments on supersonic liquid jets. They injected high speed jets into air with a spring-loaded injector (1954) and by subjecting the liquid reservoir to a shock wave pressure (1956). These jets are transients and they appear to give rise to Rayleigh-Taylor instabilities on the front face of the jet as in the problem of drop breakup in high speed air and to Kelvin-Helmholtz wave at sides of the jets where the velocity is discontinuous. The data presented by them is not suitable for comparison on the analysis given here.

19.3.2 Basic partial differential equations

For isentropic compressible fluids, the equation of continuity, the viscous stress tensor $\mathbf{T}$ and the equation of motion are expressed, in usual notation with the velocity potential ϕ for which $\boldsymbol{v} = \nabla\phi$ and $\nabla \times \boldsymbol{v} = \mathbf{0}$, as

$$\frac{\partial \rho}{\partial t} + \nabla \cdot (\rho \boldsymbol{v}) = 0, \quad \text{hence} \quad \frac{\partial \rho}{\partial t} + (\nabla\phi \cdot \nabla)\,\rho + \rho \nabla^2 \phi = 0, \tag{19.3.1}$$

$$T_{ij} = \mu \left(\frac{\partial v_i}{\partial x_j} + \frac{\partial v_j}{\partial x_i} \right) - \frac{2\mu}{3} (\nabla \cdot \boldsymbol{v})\, \delta_{ij} = 2\mu \frac{\partial^2 \phi}{\partial x_i \partial x_j} - \frac{2\mu}{3} \left(\nabla^2 \phi \right) \delta_{ij}, \tag{19.3.2}$$

$$\frac{\partial \boldsymbol{v}}{\partial t} + (\boldsymbol{v} \cdot \nabla)\, \boldsymbol{v} = -\frac{1}{\rho} \nabla p + \frac{1}{\rho} \nabla \cdot \mathbf{T} \quad \rightarrow \quad \frac{\partial \phi}{\partial t} + \frac{1}{2} |\nabla \phi|^2 + \frac{\gamma}{\gamma - 1} \frac{p}{\rho} - \frac{4}{3} \frac{\mu}{\rho} \nabla^2 \phi = B(t). \tag{19.3.3}$$

The isentropic relation is given by

$$p \rho^{-\gamma} = \text{constant} \equiv A, \quad \text{hence} \quad p = A \rho^{\gamma} \tag{19.3.4}$$

with the adiabatic exponent γ and the sound velocity c

$$c^2 = \frac{\mathrm{d}p}{\mathrm{d}\rho} = \gamma \frac{p}{\rho}. \tag{19.3.5}$$

These are used for viscous potential flow (VPF), which reduces to the inviscid potential flow (IPF) when the viscosity vanishes.

19.3.3 Cylindrical liquid jet in a compressible gas

A cylindrical liquid jet is surrounded by a compressible gas and is addressed in $0 \le r < a$ (where a is the radius of the cylindrical jet in an undisturbed state) and $-\infty < z < \infty$ in the cylindrical frame (r, θ, z). The equation of continuity, the viscous stress tensor and Bernoulli function are given for the compressible gas

$$\left.\begin{aligned} \frac{\partial \rho_a}{\partial t} + (\nabla \phi_a \cdot \nabla)\, \rho_a + \rho_a \nabla^2 \phi_a = 0, \\ T_{ij}^{(a)} = 2\mu_a \frac{\partial^2 \phi_a}{\partial x_i \partial x_j} - \frac{2\mu_a}{3} \left(\nabla^2 \phi_a\right) \delta_{ij}, \\ \frac{\partial \phi_a}{\partial t} + \frac{1}{2} |\nabla \phi_a|^2 + \frac{\gamma}{\gamma - 1} \frac{p_a}{\rho_a} - \frac{4}{3} \frac{\mu_a}{\rho_a} \nabla^2 \phi_a = B_a(t), \\ p_a = A \rho_a^\gamma \quad \rightarrow \quad \frac{\mathrm{d}p_a}{\mathrm{d}\rho_a} = \gamma A \rho_a^{\gamma - 1} = \gamma \frac{p_a}{\rho_a} = c_a^2, \end{aligned}\right\} \tag{19.3.6}$$

and for the liquid

$$\left.\begin{aligned} \rho_\ell = \text{constant}, \quad \nabla^2 \phi_\ell = 0, \quad T_{ij}^{(\ell)} = 2\mu_\ell \frac{\partial^2 \phi_\ell}{\partial x_i \partial x_j}, \\ \frac{\partial \phi_\ell}{\partial t} + \frac{1}{2} |\nabla \phi_\ell|^2 + \frac{p_\ell}{\rho_\ell} = B_\ell(t). \end{aligned}\right\} \tag{19.3.7}$$

Boundary conditions at the interface $r = a + \eta$ (where $\eta = \eta(\theta, z, t)$ is the interface displacement) are the kinematic conditions:

$$\frac{\partial \eta}{\partial t} + (\nabla \phi_a \cdot \nabla)\, \eta = \boldsymbol{n} \cdot \nabla \phi_a, \quad \frac{\partial \eta}{\partial t} + (\nabla \phi_\ell \cdot \nabla)\, \eta = \boldsymbol{n} \cdot \nabla \phi_\ell \tag{19.3.8}$$

with the outer normal vector $\boldsymbol{n}$

$$\boldsymbol{n} = \left(1, \ \frac{-1}{a + \eta} \frac{\partial \eta}{\partial \theta}, \ -\frac{\partial \eta}{\partial z}\right) \Big/ \sqrt{1 + \left(\frac{1}{a + \eta} \frac{\partial \eta}{\partial \theta}\right)^2 + \left(\frac{\partial \eta}{\partial z}\right)^2}, \tag{19.3.9}$$

and the normal stress balance:

$$p_\ell - p_a + \left(n_i T_{ij}^{(a)} n_j\right) - \left(n_i T_{ij}^{(\ell)} n_j\right) = \sigma \nabla \cdot \boldsymbol{n}, \tag{19.3.10}$$

where σ is the interfacial tension coefficient.

19.3.4 Basic isentropic relations

A basic state of the gas is with a uniform flow $\bar{\boldsymbol{v}}_a = \nabla \bar{\phi}_a = (0, 0, U_a)$ in the frame (r, θ, z) and with the constant density ρ_{a1} and pressure p_{a1}, and a basic state of the liquid is with a uniform flow $\bar{\boldsymbol{v}}_\ell = \nabla \bar{\phi}_\ell = (0, 0, U_\ell)$ and with the constant density $\rho_{\ell 1}$ and pressure $p_{\ell 1}$. The isentropic relation and the Bernoulli function lead for the gas to

$$\left.\begin{aligned} p_{a1} = A \rho_{a1}^\gamma = p_{a0} \left(\frac{\rho_{a1}}{\rho_{a0}}\right)^\gamma, \quad \frac{\mathrm{d}p_{a1}}{\mathrm{d}\rho_{a1}} = \gamma A \rho_{a1}^{\gamma - 1} = \gamma \frac{p_{a1}}{\rho_{a1}} = c_a^2, \\ \frac{1}{2} U_a^2 + \frac{\gamma}{\gamma - 1} \frac{p_{a1}}{\rho_{a1}} = \frac{1}{2} U_a^2 + \frac{c_a^2}{\gamma - 1} = \frac{c_{a0}^2}{\gamma - 1} = B_a, \ \text{ hence } \ \left[\frac{\gamma - 1}{2} M_a^2 + 1\right] \frac{\gamma p_{a1}}{\rho_{a1}} = \frac{\gamma p_{a0}}{\rho_{a0}}, \end{aligned}\right\} \tag{19.3.11}$$

where the Mach number M_a is defined as

$$M_a = \frac{U_a}{c_a}, \tag{19.3.12}$$

and ρ_{a0}, p_{a0} and c_{a0} ($c_{a0}^2 = \gamma p_{a0}/\rho_{a0}$) are defined when $M_a = 0$.

Using (19.3.11), we have

$$\left.\begin{aligned} \bar{\rho}_a = \frac{\rho_{a1}}{\rho_{a0}} = \left[\frac{\gamma-1}{2}M_a^2 + 1\right]^{-1/(\gamma-1)}, \quad \bar{p}_a = \frac{p_{a1}}{p_{a0}} = \left(\frac{\rho_{a1}}{\rho_{a0}}\right)^{\gamma}, \\ \frac{c_a^2}{c_{a0}^2} = \left[\frac{\gamma-1}{2}M_a^2 + 1\right]^{-1} \quad \text{or} \quad c_a^2 = c_{a0}^2 - \frac{\gamma-1}{2}U_a^2, \end{aligned}\right\} \tag{19.3.13}$$

in which the sound velocity c_a is given as a function of U_a. The thermodynamic properties of the ambient gas depend on the Mach number and the reference state when $M_a = 0$. For air of $\rho_{a0} = 1.2$ kg/m^3, $p_{a0} = 1$ atm$= 1.013 \times 10^5$ Pa, $c_{a0} = 340$ m/sec, and $\gamma = 1.4$. When $M_a = 1$, (19.3.13) gives $c_a^2 = 2c_{a0}^2/(\gamma+1)$ for which $c_a = 310.38$ m/sec. The third equation in (19.3.13) shows that $c_a = 0$ m/sec when $M_a \to \infty$. Then $U_a^2 = U_{am}^2 = 2c_{a0}^2/(\gamma-1)$ where $U_{am} = 760.26$ m/sec is the maximum air velocity.

The Bernoulli function for the liquid leads to

$$\frac{1}{2}U_\ell^2 + \frac{p_{\ell 1}}{\rho_{\ell 1}} = B_\ell. \tag{19.3.14}$$

The kinematic conditions are satisfied for the unidirectional flows and the interface given by $r = a$. The normal stress balance is given by

$$p_{\ell 1} - p_{a1} = \frac{\sigma}{a}, \tag{19.3.15}$$

where σ/a denotes the capillary pressure.

19.3.5 Linear stability of the cylindrical liquid jet in a compressible gas; dispersion equation

On the basic flows, small disturbances are superimposed as

$$\left.\begin{aligned} \phi_\ell = U_\ell z + \tilde{\phi}_\ell, \quad \rho_\ell = \rho_{\ell 1} \text{ (no perturbation)}, \quad p_\ell = p_{\ell 1} + \tilde{p}_\ell, \\ \phi_a = U_a z + \tilde{\phi}_a, \quad \rho_a = \rho_{a1} + \tilde{\rho}_a, \quad p_a = p_{a1} + \tilde{p}_a. \end{aligned}\right\} \tag{19.3.16}$$

The isentropic relation gives

$$p_a = A\rho_a^\gamma, \quad \text{hence} \quad p_{a1} = A\rho_{a1}^\gamma, \quad \tilde{p}_a \approx A\rho_{a1}^\gamma \gamma \frac{\tilde{\rho}_a}{\rho_{a1}} = c_a^2 \tilde{\rho}_a, \tag{19.3.17}$$

$$\frac{\gamma}{\gamma-1}\frac{p_a}{\rho_a} = \frac{c_a^2}{\gamma-1} + c_a^2\frac{\tilde{\rho}_a}{\rho_{a1}} = \frac{c_a^2}{\gamma-1} + \frac{\tilde{p}_a}{\rho_{a1}}. \tag{19.3.18}$$

For the gas, we have the equations for the disturbance:

$$\left(\frac{\partial}{\partial t} + U_a\frac{\partial}{\partial z}\right)\tilde{\rho}_a + \rho_{a1}\nabla^2\tilde{\phi}_a = 0, \quad \left(\frac{\partial}{\partial t} + U_a\frac{\partial}{\partial z}\right)\tilde{\phi}_a + c_a^2\frac{\tilde{\rho}_a}{\rho_{a1}} - \frac{4}{3}\frac{\mu_a}{\rho_{a1}}\nabla^2\tilde{\phi}_a = 0, \tag{19.3.19}$$

hence

$$\left(\frac{\partial}{\partial t} + U_a\frac{\partial}{\partial z}\right)^2\tilde{\phi}_a = \left[c_a^2 + \frac{4}{3}\frac{\mu_a}{\rho_{a1}}\left(\frac{\partial}{\partial t} + U_a\frac{\partial}{\partial z}\right)\right]\nabla^2\tilde{\phi}_a. \tag{19.3.20}$$

For the liquid, we have the equations for the disturbance:

$$\nabla^2\tilde{\phi}_\ell = 0, \quad \left(\frac{\partial}{\partial t} + U_\ell\frac{\partial}{\partial z}\right)\tilde{\phi}_\ell + \frac{\tilde{p}_\ell}{\rho_{\ell 1}} = 0. \tag{19.3.21}$$

At the interface $r = a + \tilde{\eta} \approx a$ where $\tilde{\eta} \equiv \tilde{\eta}(\theta, z, t)$ is the interface displacement, the kinematic conditions are given by

$$\frac{\partial \tilde{\eta}}{\partial t} + U_\ell \frac{\partial \tilde{\eta}}{\partial z} = \frac{\partial \tilde{\phi}_\ell}{\partial r}, \quad \frac{\partial \tilde{\eta}}{\partial t} + U_a \frac{\partial \tilde{\eta}}{\partial z} = \frac{\partial \tilde{\phi}_a}{\partial r}, \tag{19.3.22}$$

and the normal stress balance is given, on eliminating the pressures by using the Bernoulli functions, by

$$\begin{aligned} -\rho_{a1}\left(\frac{\partial}{\partial t} + U_a \frac{\partial}{\partial z}\right)\tilde{\phi}_a + 2\mu_a\left[\nabla^2 \tilde{\phi}_a - \frac{\partial^2 \tilde{\phi}_a}{\partial r^2}\right] + \rho_{\ell 1}\left(\frac{\partial}{\partial t} + U_\ell \frac{\partial}{\partial z}\right)\tilde{\phi}_\ell + 2\mu_\ell \frac{\partial^2 \tilde{\phi}_\ell}{\partial r^2} \\ = \sigma\left(\frac{\partial^2 \tilde{\eta}}{\partial z^2} + \frac{1}{a^2}\frac{\partial^2 \tilde{\eta}}{\partial \theta^2} + \frac{\tilde{\eta}}{a^2}\right). \end{aligned} \tag{19.3.23}$$

The solution to the stability problem above formulated is expressed by normal modes

$$\left.\begin{aligned} \tilde{\phi}_\ell = -\imath \frac{\omega - kU_\ell}{kI_n'(ka)} H I_n(kr) E + c.c., \quad \tilde{\phi}_a = -\imath \frac{\omega - kU_a}{\kappa K_n'(\kappa a)} H K_n(\kappa r) E + c.c., \\ \tilde{\eta} = HE + c.c., \end{aligned}\right\} \tag{19.3.24}$$

where $E \equiv \exp(\imath kz + \imath n\theta - \imath \omega t)$ with the complex angular frequency $\omega = \omega_R + \imath \omega_I$ and the real wavenumber k, n denotes the azimuthal mode. $I_n(kr)$ and $K_n(\kappa r)$ are the modified Bessel functions, where the prime denotes the derivative $I_n'(ka) = \mathrm{d}I_n(ka)/\mathrm{d}(ka)$. The Bessel functions satisfy the equations

$$\left.\begin{aligned} \nabla^2 \tilde{\phi}_\ell = \frac{\partial^2 \tilde{\phi}_\ell}{\partial r^2} + \frac{1}{r}\frac{\partial \tilde{\phi}_\ell}{\partial r} + \frac{1}{r^2}\frac{\partial^2 \tilde{\phi}_\ell}{\partial \theta^2} + \frac{\partial^2 \tilde{\phi}_\ell}{\partial z^2} = \frac{\partial^2 \tilde{\phi}_\ell}{\partial r^2} + \frac{1}{r}\frac{\partial \tilde{\phi}_\ell}{\partial r} - \frac{n^2}{r^2}\tilde{\phi}_\ell - k^2 \tilde{\phi}_\ell = 0, \\ \nabla^2 \tilde{\phi}_a - \left(\kappa^2 - k^2\right)\tilde{\phi}_a = \frac{\partial^2 \tilde{\phi}_a}{\partial r^2} + \frac{1}{r}\frac{\partial \tilde{\phi}_a}{\partial r} - \frac{n^2}{r^2}\tilde{\phi}_a - \kappa^2 \tilde{\phi}_a = 0, \end{aligned}\right\} \tag{19.3.25}$$

with

$$\kappa = \sqrt{k^2 - \frac{(\omega - kU_a)^2}{c_a^2 - \dfrac{4\imath\mu_a}{3\rho_{a1}}(\omega - kU_a)}}, \tag{19.3.26}$$

which arise from (19.3.20) and (19.3.21). Substituting (19.3.24) into (19.3.22) and (19.3.23), we find the dispersion relation

$$\begin{aligned} \left[\rho_{a1}(\omega - kU_a)^2 - 2\imath\mu_a\left(\kappa^2 - k^2\right)(\omega - kU_a)\right]\frac{kK_n(\kappa a)}{\kappa K_n'(\kappa a)} - \rho_{\ell 1}(\omega - kU_\ell)^2 \frac{I_n(ka)}{I_n'(ka)} \\ +2\imath\mu_a k\kappa(\omega - kU_a)\frac{K_n''(\kappa a)}{K_n'(\kappa a)} - 2\imath\mu_\ell k^2(\omega - kU_\ell)\frac{I_n''(ka)}{I_n'(ka)} + \sigma\left(k^2 - \frac{1 - n^2}{a^2}\right)k = 0. \end{aligned} \tag{19.3.27}$$

The wave number k_m and maximum growth rate ω_{Im} given by $\omega_{Im} = max\omega_I(k) = \omega_I(k_m)$ define the disturbance which is expected to appear in experiments. A typical dispersion relation is shown in figure 19.1. The cut-off wave number is the border of instability $\omega_I(k_c) = 0$.

19.3.6 Stability problem in dimensionless form

The scaling is made as

$$[\text{length},\ \text{velocity},\ \text{time}] = [d,\ c_a,\ d/c_a], \tag{19.3.28}$$

with $d = 2a$. The dimensionless variables are

$$(\hat{r}, \theta, \hat{z}) = \left(\frac{r}{d}, \theta, \frac{z}{d}\right), \quad \hat{t} = \frac{c_a}{d}t. \tag{19.3.29}$$

The hat on the independent variables are omitted for brevity. Then we may scale as

$$\left.\begin{aligned} \frac{\phi_\ell}{c_a d} = \frac{U_\ell}{c_a}\hat{z} + \frac{\tilde{\phi}_\ell}{c_a d} = M_\ell \hat{z} + \hat{\phi}_\ell, \quad \frac{\rho_\ell}{\rho_{\ell 1}} = 1, \quad \frac{p_\ell}{\rho_{\ell 1} c_a^2} = \bar{p}_{\ell 1} + \frac{\tilde{p}_\ell}{\rho_{\ell 1} c_a^2} = \bar{p}_{\ell 1} + \hat{p}_\ell, \\ \frac{\phi_a}{c_a d} = \frac{U_a}{c_a}\hat{z} + \frac{\tilde{\phi}_a}{c_a d} = M_a \hat{z} + \hat{\phi}_a, \quad \frac{\rho_a}{\rho_{a1}} = \frac{\rho_{a1}}{\rho_{a1}} + \frac{\tilde{\rho}_a}{\rho_{a1}} = 1 + \hat{\rho}_a, \quad \hat{p}_a = \frac{\tilde{p}_a}{\rho_{\ell 1} c_a^2} = \frac{\tilde{\rho}_a}{\rho_{\ell 1}} = \ell \hat{\rho}_a, \end{aligned}\right\} \tag{19.3.30}$$

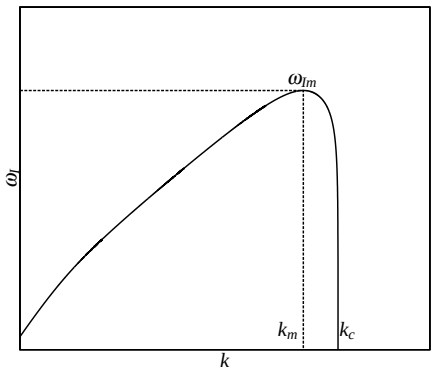

Fig. 19.1. The form of a typical graph of the growth rate ω_I versus k. ω_{Im} is the maximum growth, $\lambda_m = 2\pi/k_m$ is the wavelength of the fastest growing wave. k_c is the cut-off wavenumber. ω_{Im} and k_m are called peak values.

where $\bar{}$ denotes the normalized basic flow and $\hat{}$ denotes the normalized disturbances, and the parameters are defined as

$$\ell = \frac{\rho_{a1}}{\rho_{\ell 1}}, \quad m = \frac{\mu_a}{\mu_\ell}, \quad \nu = \frac{\mu_a}{\mu_\ell}\frac{\rho_{\ell 1}}{\rho_{a1}} = \frac{m}{\ell}, \quad M_\ell = \frac{U_\ell}{c_a}, \quad M_a = \frac{U_a}{c_a}, \quad R = \frac{\rho_{\ell 1} c_a d}{\mu_\ell}, \quad W = \frac{\sigma}{\rho_{\ell 1} d c_a^2}, \tag{19.3.31}$$

where the basic state of the gas is the function of the Mach number, with

$$\left.\begin{aligned}
&\frac{\rho_{a1}}{\rho_{a0}} = Q(M_a)^{-1/(\gamma-1)} \ \text{ where } Q(M_a) \equiv \frac{\gamma-1}{2}M_a^2 + 1, \\
&\ell = \ell_0 Q(M_a)^{-1/(\gamma-1)}, \quad \ell_0 = \rho_{a0}/\rho_{\ell 1}, \quad \frac{p_{a1}}{p_{a0}} = \left(\frac{\rho_{a1}}{\rho_{a0}}\right)^\gamma, \quad \frac{c_a^2}{c_{a0}^2} = \frac{1}{Q(M_a)}, \\
&R = R_0/Q(M_a), \quad R_0 = \frac{\rho_{\ell 1} c_{a0} d}{\mu_\ell}, \quad W = W_0 Q(M_a), \quad W_0 = \frac{\sigma}{\rho_{\ell 1} d c_{a0}^2}, \\
&\frac{1}{2}M_\ell^2 + \bar{p}_{\ell 1} = \text{constant}.
\end{aligned}\right\} \tag{19.3.32}$$

For the gas,

$$\left(\frac{\partial}{\partial t} + M_a\frac{\partial}{\partial z}\right)\hat{\rho}_a + \nabla^2\hat{\phi}_a = 0, \quad \ell\left(\frac{\partial}{\partial t} + M_a\frac{\partial}{\partial z}\right)\hat{\phi}_a + \hat{p}_a - \frac{4m}{3R}\nabla^2\hat{\phi}_a = 0. \tag{19.3.33}$$

The combination leads to

$$\left(\frac{\partial}{\partial t} + M_a\frac{\partial}{\partial z}\right)^2\hat{\phi}_a = \left[1 + \frac{4m}{3\ell R}\left(\frac{\partial}{\partial t} + M_a\frac{\partial}{\partial z}\right)\right]\nabla^2\hat{\phi}_a. \tag{19.3.34}$$

For the liquid,

$$\nabla^2\hat{\phi}_\ell = 0, \quad \left(\frac{\partial}{\partial t} + M_\ell\frac{\partial}{\partial z}\right)\hat{\phi}_\ell + \hat{p}_\ell = 0. \tag{19.3.35}$$

At the interface $r = 1/2 + \hat{\eta} \approx 1/2$ where $\hat{\eta} \equiv \hat{\eta}(\theta, z, t)$ is the interface displacement, the kinematic conditions are given by

$$\frac{\partial\hat{\eta}}{\partial t} + M_\ell\frac{\partial\hat{\eta}}{\partial z} = \frac{\partial\hat{\phi}_\ell}{\partial r}, \quad \frac{\partial\hat{\eta}}{\partial t} + M_a\frac{\partial\hat{\eta}}{\partial z} = \frac{\partial\hat{\phi}_a}{\partial r}, \tag{19.3.36}$$

and the normal stress balance is given by

$$-\ell\left(\frac{\partial}{\partial t} + M_a\frac{\partial}{\partial z}\right)\hat{\phi}_a + \frac{2m}{R}\left(\nabla^2\hat{\phi}_a - \frac{\partial^2\hat{\phi}_a}{\partial r^2}\right) + \left(\frac{\partial}{\partial t} + M_\ell\frac{\partial}{\partial z}\right)\hat{\phi}_\ell + \frac{2}{R}\frac{\partial^2\hat{\phi}_\ell}{\partial r^2} = W\left(\frac{\partial^2\hat{\eta}}{\partial z^2} + \frac{\partial^2\hat{\eta}}{\partial\theta^2} + \hat{\eta}\right) \tag{19.3.37}$$

The solution to the stability problem above formulated is expressed as

$$\left.\begin{aligned}
\hat{\phi}_\ell = -\imath\frac{\omega - kM_\ell}{kI_n'(k/2)}\hat{H}I_n(kr)E + c.c., \quad \hat{\phi}_a = -\imath\frac{\omega - kM_a}{\kappa K_n'(\kappa/2)}\hat{H}K_n(\kappa r)E + c.c., \\
\hat{\eta} = \hat{H}E + c.c.,
\end{aligned}\right\} \tag{19.3.38}$$

Table 19.2. *Properties of air-water.*

Diameter of liquid jet, d	0.001 m
Air viscosity μ_a	1.8×10^{-5} N.s/m^2
Air density ρ_{a0}	1.2 kg/m^3
Water density $\rho_{\ell 1}$	1000 kg/m^3
Surface tension coefficient σ	0.075 N/m
Ratio of the specific heats γ (air)	1.4

where $E \equiv \exp(\imath kz + \imath n\theta - \imath\omega t)$ with the complex angular frequency $\omega = \omega_R + \imath\omega_I$ and the real wavenumber k, $I_n(kr)$ and $K_n(\kappa r)$ are the modified Bessel functions, the prime denotes the derivative: $I_n'(k/2) = \mathrm{d}I_n(k/2)/\mathrm{d}(k/2)$, κ is defined as

$$\kappa = \sqrt{k^2 - \frac{\theta^2}{1 - \dfrac{4\imath m}{\ell R}\theta}}, \tag{19.3.39}$$

where

$$\theta = \omega - kM_a, \quad \theta_\ell = \omega - kM_\ell. \tag{19.3.40}$$

Therefore the dispersion relation is expressed as

$$\left[\ell\theta^2 - \frac{2\imath m}{R}\left(\kappa^2 - k^2\right)\theta\right]\frac{k}{\kappa}\alpha_{an} + \theta_\ell^2\alpha_n + \frac{2\imath mk\kappa}{R}\theta\beta_{an} + \frac{2\imath k^2}{R}\theta_\ell\beta_n = W\left(k^2 + 4n^2 - 4\right)k, \tag{19.3.41}$$

with

$$\alpha_{\ell n} = \frac{I_n(k/2)}{I_n'(k/2)}, \quad \alpha_{an} = -\frac{K_n(\kappa/2)}{K_n'(\kappa/2)}, \quad \beta_{n\ell} = \frac{I_n''(k/2)}{I_n'(k/2)}, \quad \beta_{an} = -\frac{K_n''(\kappa/2)}{K_n'(\kappa/2)}, \tag{19.3.42}$$

and $\ell = \ell_0 Q(M_a)^{-1/(\gamma-1)}$, $R = R_0/Q(M_a)$, $W = W_0 Q(M_a)$ defined under (19.3.32).

It is sometimes convenient to change the frame of the analysis to one moving with the liquid velocity U_ℓ. In this frame the undisturbed liquid jet is at rest and the gas moves with velocity $U_A = U_a - U_\ell$. This is a Gallilean change of frame in which the new coordinates are

$$z' = z + U_\ell t \tag{19.3.43}$$

and

$$E = \exp(\imath kz + \imath n\theta - \imath\omega_R t + \omega_I t) = \exp(\imath kz' + \imath n\theta - \imath\Omega_R t + \omega_I t) \tag{19.3.44}$$

where

$$\Omega_R = \omega_R + U_\ell k \tag{19.3.45}$$

in a new frequency. However, the density, pressure and sound speed of the gas are determined by the ambient conditions and gas velocity, as in (19.3.13), and these quantities do not change in a Galilean change of frame. For this reason, problems of stability of liquid jets in which U_a and U_ℓ are given, as in the experiments of Varga, Lasheras & Hopfinger 2003 discussed in section 19.3.12, are not simplified by a Galilean change of frame. In the analysis given in sections 19.3.7-19.3.11 we put $M_\ell = 0$ and $M_a = M$. This is the case of a static liquid cylinder in a moving gas.

In nearly all the computations to follow, ℓ_0, R_0 and W_0 are evaluated under standard conditions for air-water given in table 19.2. In section 19.3.11 we allow W_0 to vary; this can be thought to be the effect of changing surface tension.

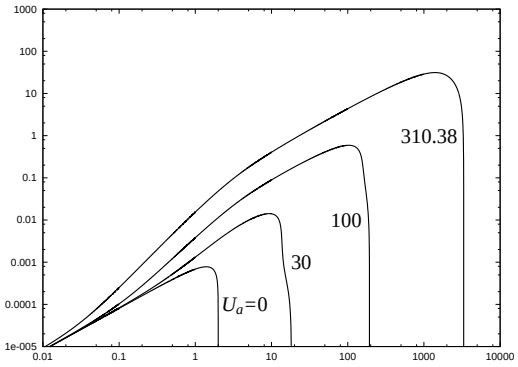

Fig. 19.2. The growth rate ω_I versus k in the axisymmetric $n = 0$ mode for IPF, using the material parameters (table 19.2) for stationary water and air with $U_a = 0$, 30, 100 and 310.38 m/sec. The values can be converted into dimensionless form (M, W) using table 19.3.

19.3.7 Inviscid potential flow (IPF)

The problem of an inviscid liquid jet moving in an inviscid compressible gas was considered by Li & Kelly (1992). The dispersion relation for this problem is (19.3.41) with $R \to \infty$ and $m/R = 0$,

$$\kappa = \sqrt{k^2 - (\omega - kM)^2}, \quad \ell\,(\omega - kM)^2\,\frac{k}{\kappa}\alpha_{an} + \omega^2\alpha_{\ell n} = W\left(k^2 + 4n^2 - 4\right)k, \tag{19.3.46}$$

The parameters of this problem are ℓ, n, M and W.

Pure capillary instability arises in the axisymmetric $n = 0$ mode for large W and in the inviscid case is independent of the gas. The case $W = 0$ is associated with pure Kelvin-Helmholtz instability for every n mode and it cannot occur in a vacuum ($\ell \neq 0$). The variation of ω_I versus k for an inviscid water in air is given in figure 19.2 with the $n = 0$ mode.

The variation of growth rates with M for particular values of k, σ, U_a was given by Li & Kelly (1992); they did not present graphs of peak growth rates $\omega_{Im}(k_m)$ and k_m as a function of M. At very high values of the Mach number

$$\ell = \ell_0/Q^{2.5} \quad \to \quad \ell_0/M^5 \tag{19.3.47}$$

and the first term of (19.3.46) may be neglective. Growth rate curves for IPF under standard condition and different Mach numbers are shown in figure 19.2.

19.3.8 Growth rate parameters as a function of M for different viscosities

In this section the data for stability computations is assembled in the table 19.3. In the table, we list the parameters for air under standard conditions and the liquid density, surface tension coefficient and the jet radius used in all the computations. Using the parameters of table 19.2, the viscosity ratio is evaluated as $m = 1.8 \times 10^{-2}$ and the other basic nondimensional parameters which depends on U_a are shown in table 19.3. Negative values $\omega_I < 0$ in Tab. 19.4 arise for non-axisymmetric $n = 1$ disturbances when U_a is small. The entries in the columns $n = 1$ in tables are left blanks.

Table 19.4 gives the values ω_{Im}, k_m and k_c of the growth rate curves like figure 19.1 for $\mu_\ell = 0$, 1 cP, 300 cP and 8000 cP. In figure 19.4 we blow up the sharply peaking growth rate curves ω_I versus k for stationary liquid jets of small viscosity in high speed transonic air. The Mach numbers for the seven curves are [1, 2, 3, 4, 5, 6, 7]=[0.92, 0.96, 0.98, 1.01, 1.05, 1.08, 1.25] when $\mu_\ell = 0.15$ cP and $\mu_\ell = 0.175$ cP and for the nine curves [1, 2, 3, 4, 5, 6, 7, 8, 9]=[0.92, 0.96, 1.00, 1.05, 1.06, 1.12, 1.15, 1.20, 1.25] when $\mu_\ell = 0.5$ cP.

Table 19.3. *Typical values and nondimensional parameters for various U_a ($U_\ell = 0$).*

U_a m/s	c_a	p_{a1}	ρ_{a1}	ℓ	M	R	W
0.00	3.400e+02	1.013e+05	1.200e+0	1.200e-03	0.000e+0	3.400e+05	6.488e-07
0.10	3.400e+02	1.013e+05	1.200e+0	1.200e-03	2.941e-04	3.400e+05	6.488e-07
0.20	3.400e+02	1.013e+05	1.200e+0	1.200e-03	5.882e-04	3.400e+05	6.488e-07
0.50	3.400e+02	1.013e+05	1.200e+0	1.200e-03	1.471e-03	3.400e+05	6.488e-07
1.00	3.400e+02	1.013e+05	1.200e+0	1.200e-03	2.941e-03	3.400e+05	6.488e-07
5.00	3.400e+02	1.013e+05	1.200e+0	1.200e-03	1.471e-02	3.400e+05	6.488e-07
10.00	3.400e+02	1.012e+05	1.199e+0	1.199e-03	2.941e-02	3.400e+05	6.489e-07
20.00	3.399e+02	1.011e+05	1.198e+0	1.198e-03	5.884e-02	3.399e+05	6.492e-07
50.00	3.393e+02	9.977e+04	1.187e+0	1.187e-03	1.474e-01	3.393e+05	6.516e-07
70.00	3.386e+02	9.833e+04	1.175e+0	1.175e-03	2.068e-01	3.386e+05	6.543e-07
100.00	3.370e+02	9.530e+04	1.149e+0	1.149e-03	2.967e-01	3.370e+05	6.602e-07
150.00	3.333e+02	8.816e+04	1.087e+0	1.087e-03	4.500e-01	3.333e+05	6.751e-07
200.00	3.280e+02	7.881e+04	1.003e+0	1.003e-03	6.097e-01	3.280e+05	6.970e-07
250.00	3.211e+02	6.787e+04	9.014e-01	9.014e-04	7.786e-01	3.211e+05	7.274e-07
300.00	3.124e+02	5.602e+04	7.860e-01	7.860e-04	9.603e-01	3.124e+05	7.684e-07
310.38	3.104e+02	5.351e+04	7.607e-01	7.607e-04	1.000e+0	3.104e+05	7.786e-07
350.00	3.018e+02	4.401e+04	6.616e-01	6.616e-04	1.160e+0	3.018e+05	8.233e-07
400.00	2.891e+02	3.258e+04	5.337e-01	5.337e-04	1.383e+0	2.891e+05	8.971e-07
450.00	2.740e+02	2.239e+04	4.082e-01	4.082e-04	1.642e+0	2.740e+05	9.987e-07
500.00	2.561e+02	1.395e+04	2.911e-01	2.911e-04	1.952e+0	2.561e+05	1.143e-06
550.00	2.347e+02	7.573e+03	1.882e-01	1.882e-04	2.343e+0	2.347e+05	1.361e-06
600.00	2.088e+02	3.338e+03	1.048e-01	1.048e-04	2.873e+0	2.088e+05	1.720e-06
650.00	1.764e+02	1.023e+03	4.505e-02	4.505e-05	3.686e+0	1.764e+05	2.412e-06
700.00	1.327e+02	1.395e+02	1.085e-02	1.085e-05	5.276e+0	1.327e+05	4.261e-06
750.00	5.568e+01	3.199e-01	1.413e-04	1.413e-07	1.347e+01	5.568e+04	2.419e-05
760.00	8.944e+0	8.832e-07	1.512e-08	1.512e-11	8.497e+01	8.944e+03	9.375e-04
760.20	4.381e+0	5.973e-09	4.262e-10	4.262e-13	1.735e+02	4.381e+03	3.908e-03

Table 19.4. *Maximum growth rate parameters (figure 19.2) for different values of M: (a) IPF; (b) $\mu_\ell = 1$ cP, $m = 1.8 \times 10^{-2}$; (c) $\mu_\ell = 300$ cP, $m = 6 \times 10^{-5}$; (d) $\mu_\ell = 8000$ cP, $m = 2.25 \times 10^{-6}$.*

a	$n=0$			$n=1$		
M	ω_{Im}	k_m	k_c	ω_{Im}	k_m	k_c
0.00	7.821e-04	1.396e+00	2.008e+00	-	-	-
0.50	3.000e+00	2.989e+02	4.483e+02	3.000e+00	2.989e+02	4.483e+02
0.75	1.149e+01	7.192e+02	1.081e+03	1.149e+01	7.147e+02	1.081e+03
1.00	7.853e+01	3.169e+03	4.933e+03	7.853e+01	3.169e+03	4.933e+03
1.10	2.302e+02	1.540e+04	2.107e+04	2.302e+02	1.540e+04	2.107e+04
1.50	1.120e+03	2.656e+05	2.755e+05	1.120e+03	2.656e+05	2.755e+05
2.00	1.576e+03	8.560e+05	8.632e+05	1.576e+03	8.560e+05	8.632e+05

b	$n=0$			$n=1$		
M	ω_{Im}	k_m	k_c	ω_{Im}	k_m	k_c
0.00	7.790e-04	1.387e+00	2.008e+00	-	-	-
0.50	2.759e+00	2.845e+02	5.869e+02	2.759e+00	2.845e+02	5.869e+02
0.75	1.007e+01	6.670e+02	1.666e+03	1.007e+01	6.670e+02	1.666e+03
1.00	3.033e+01	1.432e+03	3.799e+03	3.033e+01	1.432e+03	3.799e+03
1.10	2.673e+01	1.621e+03	3.871e+03	2.673e+01	1.621e+03	3.871e+03
1.50	1.161e+01	1.297e+03	2.998e+03	1.161e+01	1.297e+03	2.998e+03
2.00	6.363e+00	9.703e+02	2.314e+03	6.363e+00	9.703e+02	2.314e+03

c	$n=0$			$n=1$		
M	ω_{Im}	k_m	k_c	ω_{Im}	k_m	k_c
0.00	3.711e-04	9.325e-01	2.008e+00	-	-	-
0.50	1.457e-01	4.123e+01	4.492e+02	1.453e-01	4.186e+01	4.492e+02
0.75	3.735e-01	7.651e+01	1.072e+03	3.731e-01	7.723e+01	1.072e+03
1.00	1.515e+00	1.657e+02	1.531e+03	1.515e+00	1.657e+02	1.531e+03
1.10	3.803e-01	2.458e+01	1.603e+02	3.897e-01	2.413e+01	1.603e+02
1.50	1.497e-01	1.495e+01	6.733e+01	1.501e-01	1.477e+01	6.733e+01
2.00	8.965e-02	1.117e+01	4.492e+01	8.934e-02	1.090e+01	4.483e+01

d	$n=0$			$n=1$		
M	ω_{Im}	k_m	k_c	ω_{Im}	k_m	k_c
0.00	2.656e-05	2.431e-01	2.008e+00	-	-	-
0.50	6.081e-03	1.153e+01	4.492e+02	5.959e-03	1.666e+01	4.492e+02
0.75	1.507e-02	2.260e+01	1.072e+03	1.494e-02	2.989e+01	1.072e+03
1.00	1.096e-01	5.113e+01	1.522e+03	1.095e-01	5.338e+01	1.522e+03
1.10	1.485e-02	3.511e+00	9.685e+01	2.818e-02	3.268e+00	9.712e+01
1.50	4.978e-03	2.251e+00	3.223e+01	2.056e-02	1.270e+00	2.989e+01
2.00	2.301e-03	1.801e+00	2.080e+01	1.604e-02	8.641e-01	1.927e+01

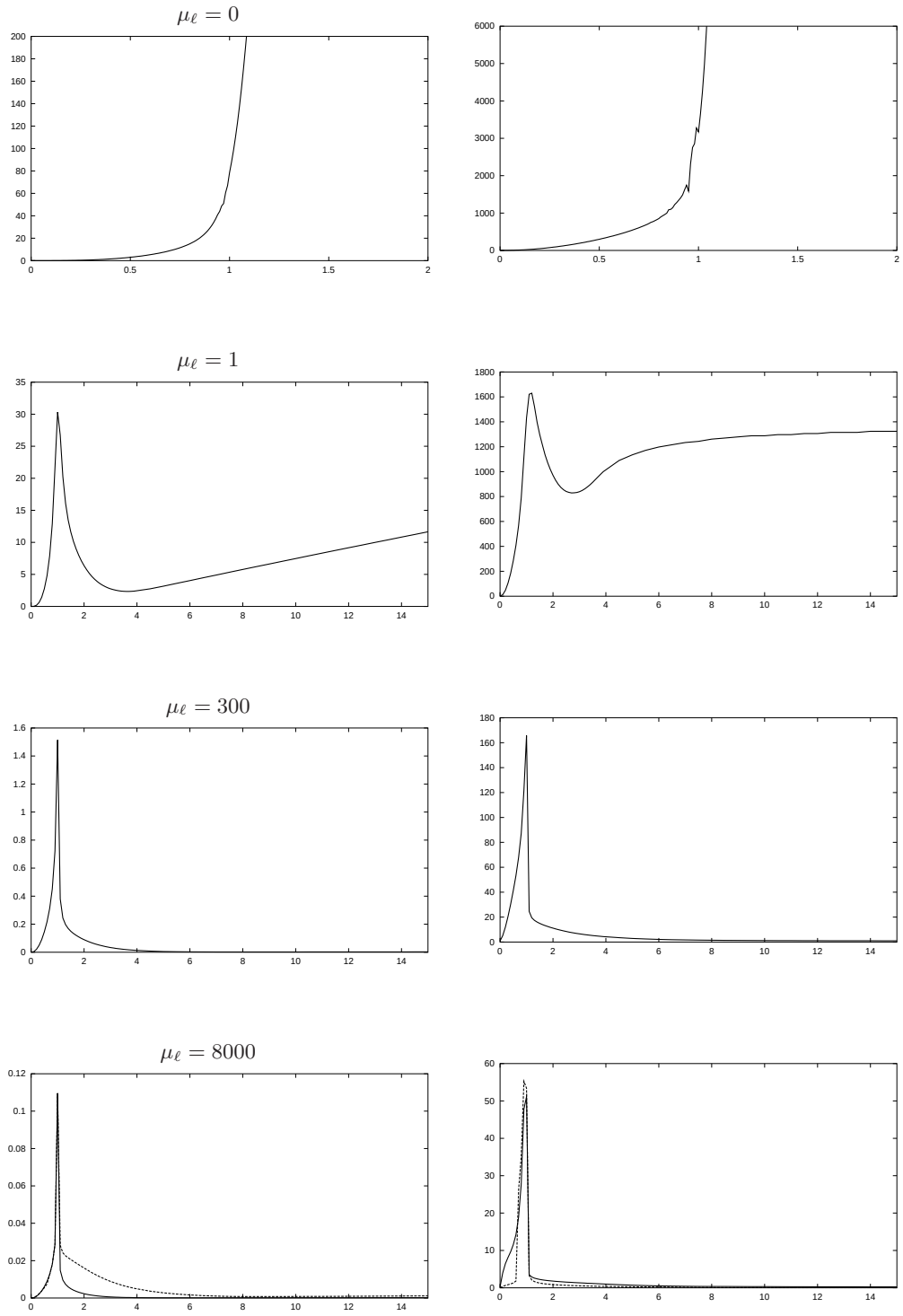

Fig. 19.3. Maximum growth rate ω_{Im} and the associated wavenumber k_m as a function of M for $\mu_\ell = 0$, 1 cP, 300 cP, 8000 cP. The solid line denotes the axisymmetric case ($n = 0$), and the dashed line in figures for μ_ℓ =8000 cP denotes $n = 1$.

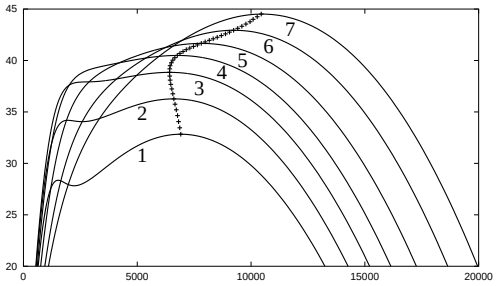

(a) ω_I versus k for $\mu_\ell = 0.15$ cP.

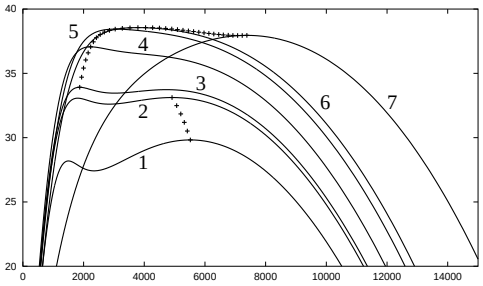

(b) ω_I versus k for $\mu_\ell = 0.175$ cP.

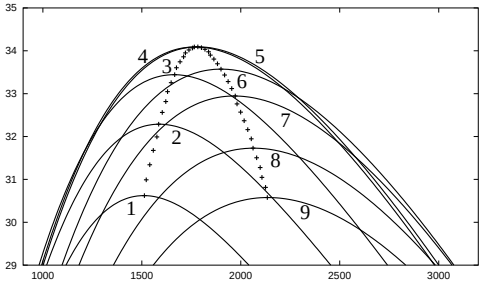

(c) ω_I versus k for $\mu_\ell = 0.5$ cP.

Fig. 19.4. Growth rate versus wavenumber for stationary liquid jet ($U_\ell = 0$) in transonic air. U_a =[1, 2, 3, 4, 5, 6, 7] = [290.08, 302.08, 314.08, 326.08, 340.08, 356.08, 370.08] m/s. (a) $\mu_\ell = 0.15$ cP: as U_a increases, the maximum growth rate marked by + increases monotonically without limit. (b) $\mu_\ell = 0.175$ cP: as U_a increases, the maximum growth rate marked by + increases, changes to another peak, attains the maximun near $U_a = 310.38$ m/sec ($M = 1$), and then decreases. (c) $\mu_\ell = 0.5$ cP: as U_a increases, the maximum growth rate marked by + increases, attains the maximun near $U_a = 310.38$ m/sec ($M = 1$), and then decreases.

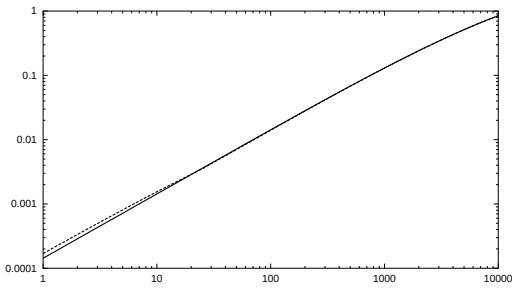

(a)The maximum growth rate ω_{Im} versus R.

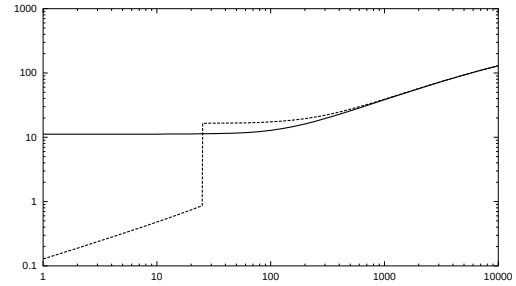

(b) k_m versus R. The growth rate curve ω_I vs. k which is shown in figure 19.5 (c) has two relative maxima ; the absolute maxima changes for R_0 between 25 and 26; this is seen as a jump in k in 19.5 (b).

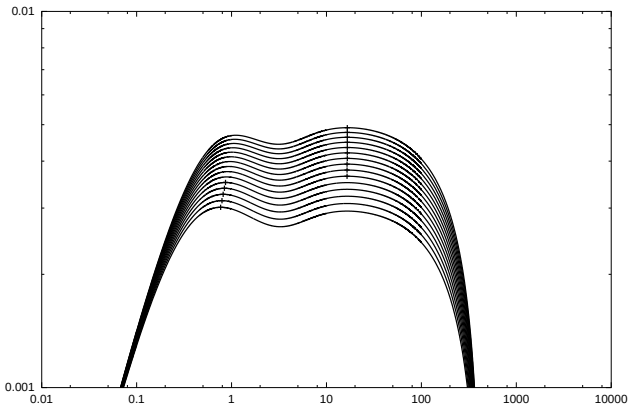

(c) ω_I vs. k.

Fig. 19.5. (a) The maximum growth rate ω_{Im} versus R and (b) k_m versus R, for $M = 0.5$; $n = 0$ in compressible gas (solid line) and $n = 1$ in compressible gas (dashed line).

19.3.9 Azimuthal periodicity of the most dangerous disturbance

Batchelor & Gill (1962) argued that the conditions at the origin of a cylinder are such as to make the axisymmetric ($n = 0$) mode and the $n = 1$ mode of azimuthal periodicity most dangerous; all the modes except $n = 1$ require that the radial and azimuthal components of the disturbance velocity vanish. The axial component of the disturbance velocity is single-valued only when $n = 0$ (see Joseph (1976), pages 73, 74). Typical graphs showing the variation of these quantities with the Reynolds number for $M = 0.5$ and $M = 2$ are shown as figures (19.5 and 19.6). Only the axisymmetric ($n = 0$) mode gives rise to insatability when $M = 0$. Inspection of figures 19.5 and 19.6 show that the most dangerous mode is $n = 1$ only for Reynolds numbers smaller than a number near 100; for larger Reynolds numbers the maximum growth rate and the most dangerous wave number are nearly the same for $n = 0$ and $n = 1$.

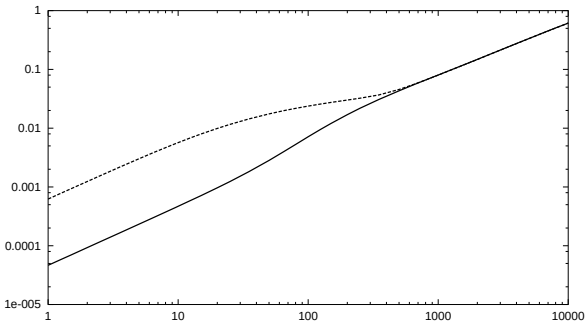

(a)The maximum growth rate ω_{Im} versus R.

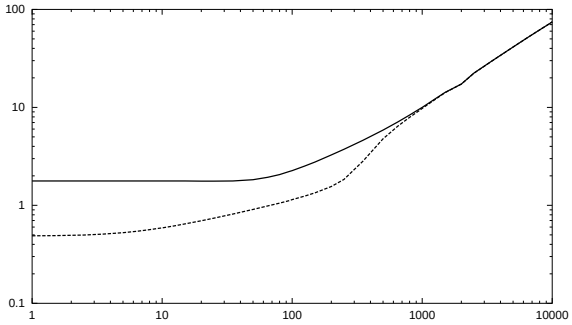

(b) k_m versus R.

Fig. 19.6. (a)The maximum growth rate ω_{Im} versus R and (b) k_m versus R, for $M = 2$; $n = 0$ in compressible gas (solid line) and $n = 1$ in compressible gas (dashed line).

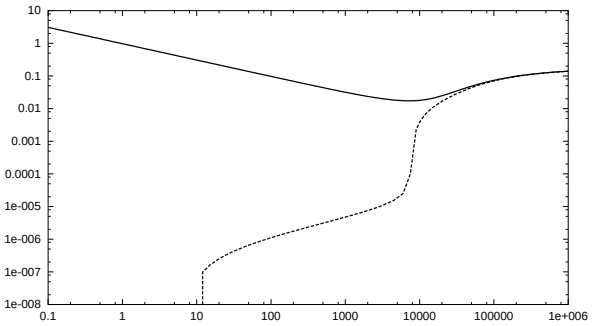

(a) The maximum growth rate ω_{Im} versus W^{-1}.

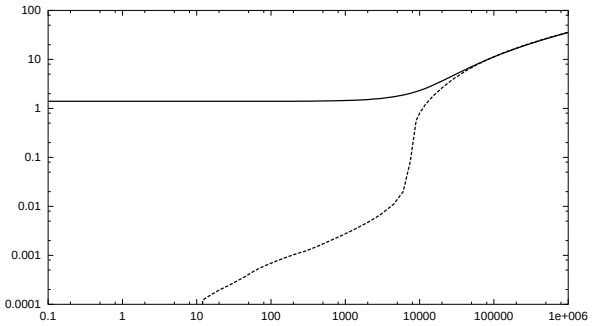

(b) k_m versus W^{-1}.

Fig. 19.7. (a) The maximum growth rate ω_{Im} versus W^{-1},(b) k_m versus W^{-1}. VPF, $M = 0.5$ for $\mu_\ell = 300$ cP; $n = 0$ in compressible gas (solid line) and $n = 1$ in compressible gas (dashed line).

19.3.10 Variation of the growth rate parameters with the Weber number

Graphs of ω_{Im} and k_m versus W^{-1} are displayed for typical cases in figure 19.7. When W is large, the instability is dominated by capillarity; when W is small Kelvin-Helmholtz instability dominates. This behavior is characteristic also for the liquid jet in an incompressible gas which was studied by Funada *et al.* (2004); they used W^{-1} rather than W following earlier literature.

We have shown in section 19.3.9 that the most dangerous mode is typically axisymmetric when the Reynolds number is larger than about 100 as is true for the cases considered here. The graphs are all similar; for small values of W^{-1} in which capillarity dominates the values of $\log \omega_{Im}$ decrease linearly with $\log W^{-1}$ giving rise to a power law $\omega_{Im} = a\left(W^{-1}\right)^p$ where a and p may be determined from the graphs. The most dangerous wave number $k_m = 1.396$ is a universal value which maximizes ω_I when surface tension dominates. All the growth rate curves have a minimum value which marks the place where Kelvin-Helmholtz instability starts to be important, after this minimum ω_{Im} and k_m increase with W^{-1}. In all case $k_m \to \infty$ as $W^{-1} \to \infty$, but ω_{Im} is lowered as $W^{-1} \to \infty$ when the liquid viscosity is not zero.

19.3.11 Convective/absolute (C/A) instability

C/A instability is used to determine when the spatial theory of instability makes sense. Practically, this comes down to a determination of the conditions under which a disturbance from a localized source will propagate downstream without corrupting the source. The disturbance may grow as it propagates but after it passes over

a fixed point it leaves the flow undisturbed. This is the case for convectively unstable flows, but absolutely unstable flows propagate both upstream and downstream. Propagation of disturbances from a vibrating ribbon in a boundary layer or Poiseuille flow are examples. For such propagation these flows must be convectively and not absolutely unstable.

The study of stability of disturbances issuing from a fixed source, leading to C/A theory, is not a complete stability theory; the traditional temporal theory of instability needs also to be considered. The temporal theory determines the conditions under which disturbances at a fixed point will grow or decay. If these conditions are such that all disturbances decay is stable, then disturbances from a fixed point will decay. Disturbances which are convectively or absolutely unstable are also temporally unstable. The propagation of impulses from a source in a convectively unstable flow can be realized provided the growth rates and amplitudes of temporally unstable flows do not corrupt the flow first. This is why experiments with vibrating ribbons are always done with care to suppress background noise which may amplify in time a fixed point.

Li & Kelly (1992) considered the convective and absolute instability of an inviscid liquid jet in an air stream of an inviscid compressible gas. They motivated their study by experiments on the instability and breakup of liquid fuel jets in crossflow. They note that

"... the breakup of the jet, however, does not seem to proceed in the gradual manner typical of the capillary instability of a liquid jet issuing into air at rest. Here the jet gradually bends over toward the direction of the free stream so that both tangential and cross-flow components of the gas flow are seen by the jet. When the jet is at an angle of about 30° form the normal to the free stream, the jet breaks into large columns in a manner so sudden that Schetz and co-workers (Sherman & Schetz (1971), Schetz *et al.* (1980)) have used the phrase "fracture" to describe the phenomenon. At this angle, the component of the gas velocity parallel to the jet's direction is approximately sonic ..."

Li & Kelly (1992) did not study a jet in crossflow; they studied a liquid in a coflowing air stream. They also considered the convective and absolute instability of a plane jet and found transition to absolute instability in the transonic region. They speculate that fracture coincides with the transition to absolute instability.

The problem considered by Li & Kelly (1992), C/A instability of a plane jet, is rather far from experiments on cross flow of Sherman & Schetz (1971) and it could be considered in the frame of temporal combined Rayleigh-Taylor, Kelvin-Helmholtz instability which should show rather exceptional behavior in transonic flow. This kind of explanation of rapid breakup of a coflowing jet was given by Varga, Lasheras & Hopfinger 2003 and it is based on a secondary RT istability not associated with absolute instability. An analysis using VPF of KH instability in the coaxial jet studied by Varga *et al.* has been given by FJSY 2006.

19.3.12 Conclusions

We studied the temporal instability of a liquid jet in a high speed compressible air stream using viscous potential flow. Since the shear stress is ignored in viscous potential flow, the analysis is compatible with the discontinuous profile used in all studies of Kelvin-Helmholtz instability. This discontinuity is not allowable for real viscous fluids where shear layers develop. Disturbances with high wavenumbers might see the details of the shear layer and alter the stability results in ways which are presently unknown.

In our analysis, which neglect shear layers, this instability is dominated by capillarity when the Weber number is large and by Kelvin-Helmholtz instability when the Weber number is small. The peak growth rates and the associated wave lengths depend strongly on the Mach number and on the viscosity of the liquid. The growth rates are dramatically larger in the transonic region and the wave lengths of the peak values are much smaller. Viscosity reduces the magnitude of the growth. The growth rate for inviscid potential flow monotonically increases as Mach number increases. For $0 < \mu_\ell < 0.168$ cP, the growth rate for viscous potential flow monotonically increases as Mach number increases. For 0.168 cP$< \mu_\ell$, the growth rate for viscous potential flow has a peak value when Mach number is nearly one. For more viscous liquids, the growth rate for viscous potential flow has a peak value when Mach number is nearly one. The peak value decreases as the viscosity μ_ℓ increases. The growth rates are very sharply peaked near $M_a = 1$ when the viscosity is larger than some

value near 0.2 cP. The dramatic change in stability of liquid jets in transonic flow predicted by analysis is possibly related to the dramatic increases in the drag coefficient of spheres and disks in transonic flow observed in experiments (Howarth (1953), p.724). It is not known if jet breakup in transonic and supersonic flow is caused directly by KH instability or through a secondary RT instability. In either case, this analysis suggests that the drop fragments would be very small.

20

Irrotational flows of viscoelastic fluids

The coupling of rotational and irrotational flows is more complicated than in Newtonian fluids because in most models of a viscoelastic fluid the stress is not linear. The equation of motion of an incompressible fluid with velocity $\boldsymbol{u} = \boldsymbol{v} + \nabla\phi$, where $\mathrm{curl}\boldsymbol{u} = \mathrm{curl}\boldsymbol{v}$ can be expressed

$$\nabla\left\{\rho\frac{\partial\phi}{\partial t} + \frac{\rho}{2}\left|\nabla\phi\right|^2 + p\right\} + \rho\mathrm{div}\left\{\boldsymbol{v}\otimes\nabla\phi + \nabla\phi\otimes\boldsymbol{v} + \boldsymbol{v}\otimes\boldsymbol{v}\right\} = \mathrm{div}\boldsymbol{\tau}\left[\boldsymbol{v} + \nabla\phi\right] \tag{20.0.1}$$

where $\boldsymbol{\tau}\left[\boldsymbol{u}\right] = \boldsymbol{\tau}\left[\boldsymbol{v} + \nabla\phi\right]$ is modeled by a constitutive equation. The "pressure" p is an unknown; together with three components of $\boldsymbol{u}$, it is the fourth unknown for three components of the momentum equation and $\mathrm{div}\boldsymbol{u} = 0$. In the decomposed equations, ϕ is an additional unknown and $\nabla^2\phi = 0$ an additional equation. The "pressure" p has no thermodynamic significance. If $\mathrm{trace}\boldsymbol{\tau} = 0$, then p is the average stress.

Many models of non-Newtonian fluids have been proposed. No model works for every kind of flow. Intelligent choices for models tune the model to the application.

20.1 Oldroyd B model

The Oldroyd B model is very often used to describe the response of viscoelastic fluids. Like other models, it has features which restrict its applicability (see Tanner 1985, p 222) but it appears to combine effects of relaxation and nonlinearity with relative ease of execution better than many other models. The stress $\boldsymbol{\tau}$ in the Oldroyd B model is governed by a rate equation

$$\lambda\overset{\nabla}{\boldsymbol{\tau}} + \boldsymbol{\tau} = \mu\left(\mathbf{A} + \tilde{\lambda}\overset{\nabla}{\mathbf{A}}\right) \tag{20.1.1}$$

where

$$\overset{\nabla}{\boldsymbol{\tau}} = \frac{\mathrm{d}\boldsymbol{\tau}}{\mathrm{d}t} - \mathbf{L}\boldsymbol{\tau} - \boldsymbol{\tau}\mathbf{L}^T \tag{20.1.2}$$

is an upper convected derivative and

$$\frac{\mathrm{d}\boldsymbol{\tau}}{\mathrm{d}t} = \frac{\partial\boldsymbol{\tau}}{\partial t} + \boldsymbol{u}\cdot\nabla\boldsymbol{\tau},$$

$$\mathbf{L}\left[\boldsymbol{u}\right] = \nabla\boldsymbol{u}, \quad L_{ij} = \frac{\partial u_i}{\partial x_j}, \quad \mathbf{A} = \mathbf{L} + \mathbf{L}^T, \quad A_{ij} = L_{ij} + L_{ij}^T, \tag{20.1.3}$$

λ is a relaxation time, $\tilde{\lambda}$ is a retardation time. The Oldroyd B model reduces to a Newtonian fluid when $\lambda = \tilde{\lambda}$ and Upper-Convected Maxwell (UCM) model when $\tilde{\lambda} = 0$. Usually $0 < \tilde{\lambda} < \lambda$.

The term $\mathrm{div}\boldsymbol{\tau}\left[\boldsymbol{v} + \nabla\phi\right]$ is much more complicated than for a Newtonian fluid; the term $\mathrm{div}\mathbf{A}\left[\boldsymbol{u}\right] = \mathrm{div}\mathbf{A}\left[\boldsymbol{v} + \nabla\phi\right] = \nabla^2\boldsymbol{v}$, but the other terms in (20.1.1) and (20.1.2) retain a strong dependence on the potential ϕ.

It can be said that the flow of viscoelastic fluids modeled as Oldroyd B have a strong irrotational component but that effective procedures to extract the irrotational component are not yet known.

20.2 Asymptotic form of the constitutive equations

The retarded motion expansion can be applied if the flow is slow and slowly varying. The antisymmetric part of the velocity gradient tensor $\mathbf{L}$ is defined as

$$\mathbf{W} = \frac{1}{2}\left(\mathbf{L} - \mathbf{L}^T\right). \tag{20.2.1}$$

The substantial, upper-convected, and corotational derivatives are defined as

$$\dot{\mathbf{A}} = \frac{\partial \mathbf{A}}{\partial t} + \boldsymbol{u}\cdot\nabla\mathbf{A}, \tag{20.2.2}$$

$$\overset{\triangledown}{\mathbf{A}} = \dot{\mathbf{A}} - \mathbf{L}\cdot\mathbf{A} - \mathbf{A}\cdot\mathbf{L}^T, \tag{20.2.3}$$

$$\overset{\circ}{\mathbf{A}} = \dot{\mathbf{A}} - \mathbf{W}\cdot\mathbf{A} + \mathbf{A}\cdot\mathbf{W}. \tag{20.2.4}$$

It can be shown that the relation between $\overset{\triangledown}{\mathbf{A}}$ and $\overset{\circ}{\mathbf{A}}$ is

$$\overset{\circ}{\mathbf{A}} = \overset{\triangledown}{\mathbf{A}} + \mathbf{A}^2. \tag{20.2.5}$$

20.2.1 Retarded motion expansion for the UCM model

The upper-convected Maxwell (UCM) model is

$$\lambda\,\overset{\triangledown}{\boldsymbol{\tau}} + \boldsymbol{\tau} = \mu\mathbf{A}. \tag{20.2.6}$$

Following Larson, we ignore $\lambda\,\overset{\triangledown}{\boldsymbol{\tau}}$ and obtain at first order

$$\boldsymbol{\tau}^{(1)} = \mu\mathbf{A}. \tag{20.2.7}$$

It follows that

$$\overset{\triangledown}{\boldsymbol{\tau}}^{(1)} = \mu\,\overset{\triangledown}{\mathbf{A}}. \tag{20.2.8}$$

Then the stress tensor can be obtained to second order in λ by substituting (20.2.8) into (20.2.6)

$$\boldsymbol{\tau}^{(2)} = \mu\mathbf{A} - \lambda\mu\,\overset{\triangledown}{\mathbf{A}} = \mu\mathbf{A} - \lambda\mu\,\overset{\circ}{\mathbf{A}} + \lambda\mu\mathbf{A}^2, \tag{20.2.9}$$

$$= \mu\mathbf{A} - \lambda\mu(\dot{\mathbf{A}} - \mathbf{W}\cdot\mathbf{A} + \mathbf{A}\cdot\mathbf{W}) + \lambda\mu\mathbf{A}^2. \tag{20.2.10}$$

This can be compared to the second order fluid model

$$\boldsymbol{\tau} = \mu\mathbf{A} + \alpha_1(\dot{\mathbf{A}} + \mathbf{L}\cdot\mathbf{A} + \mathbf{A}\cdot\mathbf{L}^T) + \alpha_2\mathbf{A}^2. \tag{20.2.11}$$

The same tensors appear with different coefficients.

20.2.2 The expanded UCM model in potential flow

In potential flows, $\nabla\boldsymbol{u} = \dfrac{\partial^2\phi}{\partial x_i \partial x_j}$. Therefore,

$$\mathbf{L} = \mathbf{L}^T = \frac{1}{2}\mathbf{A}, \qquad \mathbf{W} = 0. \tag{20.2.12}$$

The expanded UCM model reduces to

$$\boldsymbol{\tau} = \mu\mathbf{A} - \lambda\mu\dot{\mathbf{A}} + \lambda\mu\mathbf{A}^2. \tag{20.2.13}$$

The momentum equation is

$$\rho\left[\partial\boldsymbol{u}/\partial t + (\boldsymbol{u}\cdot\nabla)\boldsymbol{u}\right] = -\nabla p + \nabla\cdot\boldsymbol{\tau}. \tag{20.2.14}$$

When $\boldsymbol{u} = \nabla\phi$ (see Joseph 1992),

$$\mathrm{div}(\boldsymbol{u}\cdot\nabla\mathbf{A}) = \mathrm{grad}\chi, \quad \mathrm{div}\mathbf{A}^2 = 2\mathrm{grad}\chi \;\Rightarrow\; \nabla\cdot\boldsymbol{\tau} = \lambda\mu\mathrm{grad}\chi \tag{20.2.15}$$

where

$$\chi = \frac{\partial^2\phi}{\partial x_i\partial x_j}\frac{\partial^2\phi}{\partial x_j\partial x_i} = \frac{1}{4}\mathrm{tr}\mathbf{A}^2, \quad A_{ij} = 2\frac{\partial^2\phi}{\partial x_i\partial x_j}.$$

Combining (20.2.14) and (20.2.15) we find a Bernoulli equation

$$\rho\frac{\partial\phi}{\partial t} + \frac{\rho}{2}\left|\nabla\phi\right|^2 + p - \lambda\mu\chi = C(t). \tag{20.2.16}$$

Now the total stress can be written as,

$$\boldsymbol{T} = -\left[C + \lambda\mu\chi - \rho\frac{\partial\phi}{\partial t} - \frac{\rho}{2}\left|\nabla\phi\right|^2\right]\mathbf{1} + \mu\mathbf{A} - \lambda\mu\left(\frac{\partial}{\partial t} + \boldsymbol{u}\cdot\nabla\right)\mathbf{A} + \lambda\mu\mathbf{A}^2. \tag{20.2.17}$$

20.2.3 Potential flow past a sphere calculated using the expanded UCM model

The potential of a uniform flow past a sphere is given by

$$\phi = -Ur\cos\theta\left(1 + \frac{a^3}{2r^3}\right) \tag{20.2.18}$$

where U is the velocity of the uniform stream and a is the radius of the sphere. The velocities are

$$u_r = -U\left(1 - \frac{a^3}{r^3}\right)\cos\theta, \quad u_\theta = U\left(1 + \frac{a^3}{2r^3}\right)\cos\theta. \tag{20.2.19}$$

The tensor $\mathbf{A}$ can be evaluated

$$\mathbf{A} = \frac{3a^3U}{r^4}\begin{bmatrix} -2\cos\theta & -\sin\theta & 0 \\ -\sin\theta & \cos\theta & 0 \\ 0 & 0 & \cos\theta \end{bmatrix}. \tag{20.2.20}$$

Then the Bernoulli's equation (20.2.16) is used to obtain the pressure at the surface of the sphere

$$p = p_\infty + \lambda\mu\frac{9U^2}{2a^2}\left(1 + 2\cos^2\theta\right) + \frac{\rho}{2}U^2\left(1 - \frac{9}{4}\sin^2\theta\right), \tag{20.2.21}$$

where p_∞ is the pressure at infinity. The normal stress T_{rr} at the surface of the sphere is calculated from (20.2.17) and expressed in a dimensionless form

$$T^*_{rr} = \frac{T_{rr} + p_\infty}{\rho U^2/2} = \left(\frac{9}{4}\sin^2\theta - 1\right) - \frac{12}{R_e}\cos\theta + \frac{\lambda\mu}{\rho a^2}\left(45 - 72\sin^2\theta\right), \tag{20.2.22}$$

where $R_e = \rho Ua/\mu$ is the Reynolds number. At the stagnation points of a sphere [$r = a,\ \theta = 0$ or π], the normal stresses are, respectively

$$\frac{T_{rr} + p_\infty}{\rho U^2/2} = \left[-1 + \frac{45\lambda\mu}{\rho a^2}\right] \mp \frac{12}{R_e}. \tag{20.2.23}$$

The viscous contribution gives rise to compression – $12/R_e$ at the front stagnation point and to tension $12/R_e$ at the rear. The stress due to inertia and viscoelasticity is the same at $\theta = 0$ and $\theta = \pi$ and is a tension when $45\lambda\mu > \rho a^2$. This condition represents a competition between the inertia and the viscoelasticity. If ρa^2 is not too large the stress at the stagnation points is a tension, reversing the compression due to inertia.

Coleman and Noll 1960 developed a theory for a general stress functional for incompressible fluids which depend only on the history of the first spatial gradient of the deformation. Fluids of this type are called simple; they are rather too general to be applied. Useful forms of a simple fluid can be obtained in certain special asymptotic limits in which the range of fluid response is severely limited.

One such limit is defined for small amplitude, but possibly high frequency (Joseph 1990, p 539) motions. In this limit, the present value of stress at a point $\boldsymbol{x}$

$$\boldsymbol{\tau}(x,t) = \int_0^\infty G(s)\mathbf{A}\left[\boldsymbol{u}(x,t-s)\right] \mathrm{d}s \tag{20.2.24}$$

is determined by the history of strain rate $\mathbf{A}$. The relaxation function is assumed to be rapidly decaying, say proportional to $\exp(-\lambda s)$, this weights the present value of the stain more strongly in the recent history than in the past history.

Fluids satisfying (20.2.24) are called linear viscoelastic with fading memory. For these fluids, the force density

$$\mathrm{div}\boldsymbol{\tau} = \int_0^\infty G(s)\nabla^2\boldsymbol{v}(x,t-s)\ \mathrm{d}s \tag{20.2.25}$$

does not depend on the irrotational flow.

20.3 Second order fluids

Another general class of models, namely the second-order fluid model, introduced by Coleman and Noll 1960 arises from an expansion of the general stress functional for slow and slowly varying motions (Rivlin & Ericksen 1955; Bird, Armstrong & Hassager 1987; Joseph 1990). It has been used in many studies of viscoelastic behaviour with varying degrees of success; the predictions of fluid mechanic response to rapidly varying motions in which fluid memory is important have not been satisfactory, but the predictions for slow steady motions are excellent. We regard the results of analysis using the second-order fluid model as tentative and subject to ultimate validation by experiment and by comparison with direct numerical simulation using other constitutive equations.

If slow motions are defined as those for which $\boldsymbol{u} = \varepsilon\hat{\boldsymbol{u}}$ for finite $\hat{\boldsymbol{u}}$ as ε tends to zero, then slowly vary flows are such that

$$\frac{\partial}{\partial t} = \varepsilon\frac{\partial}{\partial \hat{t}}$$

are nearly steady in the sense

$$\frac{\mathrm{d}}{\mathrm{d}t}(\cdot) = \varepsilon^2\left[\frac{\partial}{\partial \hat{t}}(\cdot) + \hat{\boldsymbol{u}}\cdot\nabla(\cdot)\right]$$

Nearly steady flows are not useful for the description of relaxation effects.

The asymptotic form of the constitutive equation for a viscoelastic fluid in slow, slowly varying motion, is a Newtonian fluid at order ε and a second order fluid at order ε^2. Higher order approximations can be derived; they have unknown coefficients and are rarely used.

At first order

$$\boldsymbol{\tau} = \mu\mathbf{A}[\boldsymbol{u}]. \tag{20.3.1}$$

At second order

$$\boldsymbol{\tau} = \mu\mathbf{A}[\boldsymbol{u}] + \alpha_1\mathbf{B}[\boldsymbol{u}] + \alpha_2\mathbf{A}^2[\boldsymbol{u}] \tag{20.3.2}$$

where

$$\mathbf{B} = \frac{\partial\mathbf{A}}{\partial t} + (\boldsymbol{u}\cdot\nabla)\mathbf{A} + \mathbf{A}\mathbf{L} + \mathbf{L}^T\mathbf{A}, \tag{20.3.3}$$

$\alpha_1 = -n_1/2$ and $\alpha_2 = n_1 + n_2$ where $[n_1, n_2] = \left[N_1\left(\overset{o}{\gamma^2}\right),\ N_2\left(\overset{o}{\gamma^2}\right)\right] / \overset{o}{\gamma^2}$ as $\overset{o}{\gamma} \to 0$ are constants obtained from the first and second normal stress differences. The first normal stress difference is generally positive; the second normal stress difference N_2 can be negative but much smaller than N_1. For a typical liquid M1 (Hu et al. 1990), $\rho = 0.895$ g/cm^3,

$$[\alpha_1,\ \alpha_2] = [-3,\ 5.34]\ \text{g/cm}.$$

The equations of motion for a second order incompressible fluid are

$$\rho\left[\frac{\partial \boldsymbol{u}}{\partial t}+\boldsymbol{u}\cdot\nabla\boldsymbol{u}\right]=-\nabla p+\mu\nabla^2\boldsymbol{u}+\operatorname{div}\left[\alpha_1\mathbf{B}+\alpha_2\mathbf{A}^2\right] \tag{20.3.4}$$

or

$$\operatorname{div}\boldsymbol{\tau}\left[\boldsymbol{u}\right]=\operatorname{div}\boldsymbol{\tau}\left[\boldsymbol{v}+\nabla\phi\right]=\mu\nabla^2\boldsymbol{v}+\operatorname{div}\left[\alpha_1\mathbf{B}+\alpha_2\mathbf{A}^2\right] \tag{20.3.5}$$

The nonlinear tensors $\mathbf{B}$ and $\mathbf{A}^2$ depend both on $\boldsymbol{v}$ and ϕ.

The second order fluid form of viscoelastic models can also be obtained by the method of successive approximations. Consider the Oldroyd B model. The first approximation is $\overset{\nabla}{\boldsymbol{\tau}}=\mu\overset{\nabla}{\mathbf{A}}$ may be inserted into (20.1.1) which becomes

$$\left(\lambda-\tilde{\lambda}\right)\mu\overset{\nabla}{\mathbf{A}}\left[\boldsymbol{u}\right]+\boldsymbol{\tau}=\mu\mathbf{A} \tag{20.3.6}$$

Equation (20.3.6) may be expressed corotational model

$$\boldsymbol{\tau}=\mu\mathbf{A}-\left(\lambda-\tilde{\lambda}\right)\mu\left[\frac{\mathrm{d}\mathbf{A}}{\mathrm{d}t}-\mathbf{W}\mathbf{A}+\mathbf{A}\mathbf{W}-\mathbf{A}^2\right] \tag{20.3.7}$$

$$\tau_{ij}=\mu A_{ij}-\left(\lambda-\tilde{\lambda}\right)\mu\left[\frac{\mathrm{d}A_{ij}}{\mathrm{d}t}-W_{il}A_{lj}+A_{il}W_{lj}-A_{il}A_{lj}\right], \tag{20.3.8}$$

where $\mathbf{W}$ vanishes for potential flow.

20.4 Purely irrotational flows

A sufficient condition for a purely irrotational flow is that every flow given by a potential $\boldsymbol{u}=\nabla\phi$, $\boldsymbol{v}=0$, is compatible with solutions of the equations of motion (20.0.1); that is

$$\operatorname{curl}\left(\nabla\cdot\boldsymbol{\tau}\left[\nabla\phi\right]\right)=0, \tag{20.4.1}$$

$$\varepsilon_{lmn}\frac{\partial^2\tau_{lm}}{\partial x_l\partial x_m}\left[\nabla\phi\right]=0. \tag{20.4.2}$$

Though this condition is not satisfied for $\boldsymbol{u}=\nabla\phi$ by most constitutive equation (Joseph and Liao 1994 a,b), it is satisfied for invicid fluid, for viscous fluids with constant properties, for linear viscoelastic and second-order fluids.

20.5 Purely irrotational flows of a second order fluid

When $\boldsymbol{u}=\nabla\phi$ (see Joseph 1992a),

$$\operatorname{div}\left(\boldsymbol{u}\cdot\nabla\mathbf{A}\right)=\operatorname{grad}\chi,\quad \operatorname{div}\left(\mathbf{A}\mathbf{L}\right)=\operatorname{grad}\chi,\quad \operatorname{div}\mathbf{A}^2=2\operatorname{grad}\chi \tag{20.5.1}$$

$$\Rightarrow\operatorname{div}\left[\alpha_1\mathbf{B}+\alpha_2\mathbf{A}^2\right]=\operatorname{grad}\left(3\alpha_1+2\alpha_2\right)\chi, \tag{20.5.2}$$

where

$$\chi=\frac{\partial^2\phi}{\partial x_i\partial x_j}\frac{\partial^2}{\partial x_j\partial x_i}=\frac{1}{4}\operatorname{tr}\mathbf{A}^2,\quad A_{ij}=2\frac{\partial^2\phi}{\partial x_i\partial x_j}. \tag{20.5.3}$$

Combining (20.2.14) and (20.5.2) we find a Bernoulli equation

$$\rho\frac{\partial\phi}{\partial t}+\frac{1}{2}\rho\left|\nabla\phi\right|^2+p-\hat{\beta}\chi=C(t), \tag{20.5.4}$$

where $\hat{\beta}=3\alpha_1+2\alpha_2\geq 0$ is the climbing constant. Returning now to the stress with the pressure (20.5.4), we obtain

$$T=-\left[C+\hat{\beta}\chi-\rho\frac{\partial\phi}{\partial t}-\frac{1}{2}\rho\left|\nabla\phi\right|^2\right]\mathbf{1}+\left[\mu+\alpha_1\left(\frac{\partial}{\partial t}+\boldsymbol{u}\cdot\nabla\right)\right]\mathbf{A}+\left(\alpha_1+\alpha_2\right)\mathbf{A}^2. \tag{20.5.5}$$

20.6 Reversal of the sign of the normal stress at a point of stagnation

The Cartesian components of the stress (20.5.5) are given by

$$\begin{aligned} T_{ij} &= -\left[C+\hat{\beta}\phi_{,il}\phi_{,il}-\rho\phi_{,t}-\rho\left|\boldsymbol{u}\right|^2/2\right]\delta_{ij}+2\left[\mu+\alpha_1\left(\partial_t+\boldsymbol{u}\cdot\nabla\right)\right]\phi_{ij} \\ &\quad +4\left(\alpha_1+\alpha_2\right)\phi_{,il}\phi_{,lj}, \end{aligned} \tag{20.6.1}$$

In the diagonal coordinates x_1, x_2, x_3 of the frame in which $\phi_{,ij}$ is diagonal

$$\left[\phi_{,ij}\right]=\begin{bmatrix}\lambda_1 & 0 & 0\\ 0 & \lambda_2 & 0\\ 0 & 0 & \lambda_3\end{bmatrix}, \tag{20.6.2}$$

we have

$$\begin{aligned} \begin{bmatrix}\sigma_{11} & 0 & 0\\ 0 & \sigma_{22} & 0\\ 0 & 0 & \sigma_{33}\end{bmatrix} &= -\left[C-\rho\phi_t-\rho\left|\boldsymbol{u}\right|^2/2+\hat{\beta}\left(\lambda_1^2+\lambda_2^2+\lambda_3^2\right)\right]\begin{bmatrix}1 & 0 & 0\\ 0 & 1 & 0\\ 0 & 0 & 1\end{bmatrix} \\ &\quad +2\left[\mu+\alpha_1\left(\partial_t+\nabla\phi\cdot\nabla\right)\right]\begin{bmatrix}\lambda_1 & 0 & 0\\ 0 & \lambda_2 & 0\\ 0 & 0 & \lambda_3\end{bmatrix}+4\left(\alpha_1+\alpha_2\right)\begin{bmatrix}\lambda_1^2 & 0 & 0\\ 0 & \lambda_2^2 & 0\\ 0 & 0 & \lambda_3^2\end{bmatrix} \end{aligned} \tag{20.6.3}$$

The case of flow at the stagnation points of a body in steady flow, in an arbitrary direction is of special interest. The steady streaming past a stationary body is equivalent, under a Galilean transformation, to the steady motion of a body in an otherwise quiet fluid. The potential flow of a fluid near a point $(x_1,x_2,x_3)=(0,0,0)$ of stagnation is a purely extensional motion with

$$\left[\lambda_1,\lambda_2,\lambda_3\right]=\frac{U}{L}\dot{S}\left[2,-1,-1\right], \tag{20.6.4}$$

where $\dot{S}$ is the dimensionless rate of stretching in the direction x_1, L is the scale of length and

$$\left[u_1,u_2,u_3\right]=\frac{U}{L}\dot{S}\left[2x_1,-x_2,-x_3\right]. \tag{20.6.5}$$

In this case

$$\begin{aligned} \begin{bmatrix}T_{11} & 0 & 0\\ 0 & T_{22} & 0\\ 0 & 0 & T_{33}\end{bmatrix} &= \frac{\rho}{2}\left[\frac{U^2}{L^2}\dot{S}^2\left(4x_1^2+x_2^2+x_3^2\right)-U^2\right]\begin{bmatrix}1 & 0 & 0\\ 0 & 1 & 0\\ 0 & 0 & 1\end{bmatrix} \\ &\quad +\mu\frac{U}{L}\dot{S}\begin{bmatrix}2 & 0 & 0\\ 0 & -1 & 0\\ 0 & 0 & -1\end{bmatrix}+2\frac{U^2}{L^2}\dot{S}^2\begin{bmatrix}-\alpha_1+2\alpha_2 & 0 & 0\\ 0 & -7\alpha_1-4\alpha_2 & 0\\ 0 & 0 & -7\alpha_1-4\alpha_2\end{bmatrix} \end{aligned} \tag{20.6.6}$$

At the stagnation point itself

$$\sigma_{11}=-\frac{\rho}{2}U^2+2\mu\dot{S}+2(2\alpha_2-\alpha_1)\frac{U^2}{L^2}\dot{S}^2. \tag{20.6.7}$$

Since $\alpha_1<0$, $2\alpha_2-\alpha_1=\dfrac{5}{2}n_1+2n_2>0$, the normal stress term in (20.6.7) is positive, independent of the sign of $\dot{S}$, but $2\mu\dot{S}$ is negative at the front side of a falling body and is positive at the rear.

The motion of bodies in viscoelastic fluids can be said to be maximally different than the motion of the same bodies in a Newtonian fluid. As a rule of thumb, contrary thinking is appropriate. This difference is perfectly correlated with a change in the sign of the normal stress, from compression to tension, in the particulate flows described below.

20.7 Fluid forces near stagnation points on solid bodies

20.7.1 Turning couples on long bodies

It is surprising that turning couples on long bodies determine the stable configurations of suspensions of spherical bodies. A long body is an ellipsoid or a cylinder; a broad body is a flat plate. When such bodies are dropped in Newtonian fluids, they put their broadside perpendicular to the stream. This is an effect of inertia which is usually explained by turning couples at points of stagnation. The mechanism is the same one that causes an aircraft at a high angle of attack to stall.

The settling orientation of long particles is indeterminate in Stokes flow; however, no matter how small the Reynolds number may be, the body will turn its broadside to the stream; inertia will eventually have its way. When the same long bodies fall slowly in a viscoelastic liquid, they do not put their broadside perpendicular to the stream; they do the opposite, aligning the long side parallel to the stream.

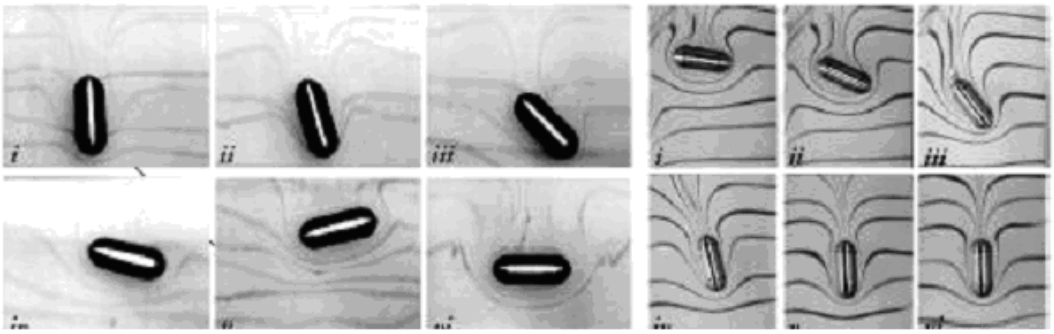

(a) (b)

Fig. 20.1. Cylinders falling in (a) Newtonian fluid (glycerin), and (b) viscoelastic fluid (2% aqueous PEO solution). In (a), the cylinder is turned horizontal by inertia; in (b), it is turned vertical by viscoelastic pressures

20.7.2 Particle-particle interactions

The flow-induced anisotropy of a sedimenting or fluidized suspension of spheres is determined by the pair interactions between neighboring spheres. These pair interactions are largely determined by normal stresses at points of stagnation on the spheres which are compressive in Newtonian fluids and tensile in viscoelastic fluid; the stagnation points are on side between spheres falling side by side and are pushed apart by compression and pulled together by tension. The principal interactions can be described as drafting, kissing and tumbling in Newtonian liquids and as drafting, kissing and chaining in viscoelastic liquids. The drafting and kissing scenarios are surely different, despite appearances. Kissing spheres align with the stream; they are then momentarily long bodies.

The long bodies momentarily formed by kissing spheres are unstable in Newtonian liquids to the same turning couples that turn long bodies broadside-on. Therefore, they tumble. This is a local mechanism which implies that globally, the only stable configuration is the one in which the most probable orientation between any pair of neighboring spheres is across the stream. The consequence of this microstructural property is a flow-induced anisotropy, which leads ubiquitously to lines of spheres across the stream; these are always in evidence in two-dimensional fluidized beds of finite size spheres. Though they are less stable, planes of spheres in three-dimensional beds can also be found by anyone who cares to look.

If two touching spheres are launched side-by-side in a Newtonian fluid, they will be pushed apart until a stable separation distance between centers across the stream is established; then the spheres fall together without further lateral migration (see Figure 20.3.a1).

On the other hand, if the same two spheres are launched in a viscoelastic fluid from an initial side-by-

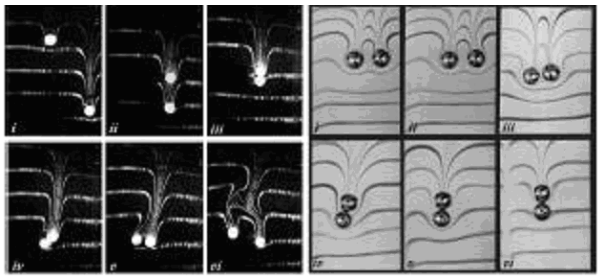

(a) (b)

Fig. 20.2. (a) Spheres in Newtonian Fluids. Spheres settling in glycerin draft (i-ii), kiss (iii), and tumble (iv-vi). They tumble because a pair of kissing spheres acts like a long body, which is unstable when its long axis is parallel to the stream. The forces in a Newtonian fluid are dispersive; the tumbling spheres are pushed apart by pressures at stagnation points between the spheres (v-vi). (b) Spheres in non-Newtonian Fluids. Spheres falling in a 2% aqueous PEO solution draft, kiss, and chain. They chain because the forces in a viscoelastic fluid are aggregative. A chain of spheres turn just like the solid cylinder in Figure 20.1.b (i-vi). Reversing time, we see that chaining, kissing, and drafting in b(vi-i) are like drafting, kissing, and tumbling in a(i-vi).

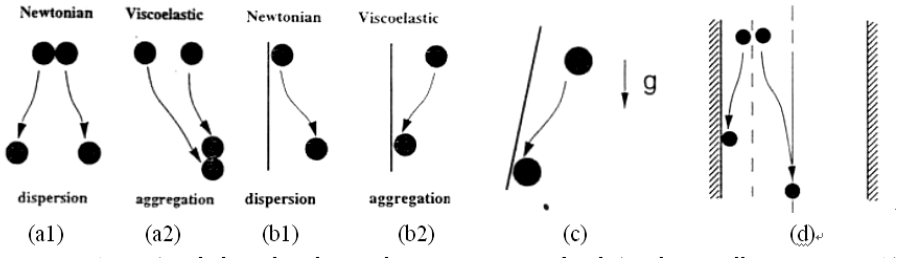

Fig. 20.3. (a1, a2) Side-by-side sphere-sphere interactions; (b1, b2) Sphere-wall interactions; (c) A sphere in a viscoelastic liquid is sucked to a tilted wall; (d) Spheres dropped between widely-spaced walls. The dotted line is the critical distance d_{cr} for wall-sphere interaction. When $d < d_{cr}$, the sphere goes to the wall. When $d > d_{cr}$, the sphere seeks the center.

side configuration in which the two spheres are separated by a smaller than critical gap, as in Figure 20.3.a2, the spheres will attract, turn and chain. One might say that we get dispersion in the Newtonian liquid and aggregation in the viscoelastic liquid.

20.7.3 Sphere-wall interactions

If a sphere is launched near a vertical wall in a Newtonian liquid, it will be forced away from the wall to an equilibrium distance at which lateral migration stops (see Figure 20.3.b1); in the course of its migration it will acquire a counter-clockwise rotation which appears to stop when the sphere stops migrating. The rotation is anomalous in that clockwise rotation would be induced from shear at the wall. The anomalous rotation seems to be generated by blockage in which high stagnation pressures force the fluid to flow around the outside of the spheres. If the same sphere is launched near a vertical wall in a viscoelastic liquid, it will be sucked all the way to the wall (see Figure 20.3.b2). It rotates anomalously as it falls. This is very strange since the sphere appears to touch the wall where friction would make it rotate in the other sense. Closer consideration shows that there is a gap between the sphere and the wall. The anomalous rotation is again due to blocking which forces liquid to flow around the outside of the sphere. The pulling action of the wall can be so strong that even if the wall is slightly tilted from the vertical so that the sphere would fall away, it will still be sucked to the wall (see Figure 20.3.c).

If the launching distance between a sphere and a vertical wall is large enough, the wall will not attract a sphere falling in a viscoelastic fluid. This means that there is a critical distance d_{cr} for attraction. Of course, this distance is smaller when the wall is tilted as in Figure 20.3.c. In this case, if the sphere is launched at a distance greater than the critical one, it will fall away from the wall.

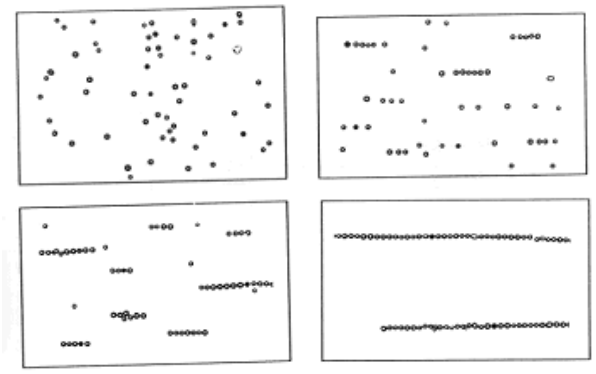

Fig. 20.4. A 2% suspension of glass spheres (60-70 μm in size) in a highly viscoelastic polymer solution of 0.5% polyacrylamide in deionized water. (a) After loading - the particles are randomly distributed. (b) After a sideways movement on the top plate of about 3 cm. (c) After the top plate had been moved back and forth several times. (d) After further and faster movement of the top plate. (From Michele et al. 1977)

20.7.4 Flow induced microstructure.

The tendency to aggregate into tight chains of particles all in a row is omnipresent. It is definitely a property of viscoelastic fluids; the same particles disperse rather than chain in Newtonian fluids. This tendency is encountered for particles of all sizes (from nanometers to centimeters) and in different kinds of motion (listed below). We regard chaining of particles as a form of self-assembly generated by flow stresses in a fluid in motion.

(1) Shear flow (Michele et al. 1977, Petit and Noetinger 1988)

(2) Shear flows of 28 nanometer SiO_2 particles in solutions of hydroxypropycellulose and polyethylene oxide in water (Scirocco et al. 2005)

(3) Extensional flow (Michele et al. 1977)

(4) Sedimentation (Liu and Joseph 1993)

(5) Fluidization

The experiments by Michele et al. demonstrated that chains of small spheres may be created and aligned in the direction of the motion in shear flows. A droplet of a suspension of glass spheres was placed between two glass plates which were then pushed together as close as possible. The aggregation of the particles was then accomplished by moving the top plate sideways parallel to the bottom plate to generate an approximate planar shear flow.

The chains of particles shown in Figures 20.4 and 20.5 occurred when the distance between the glass was 1 mm. Shear-induced structures in macroscopic dispersions were also reported by in Petit and Noetinger 1988. A suspension of glass spheres of diameter 40 μm in silicon oil or in highly viscoelastic polyisobuty-lene was sandwiched between two parallel glass plates with gaps ranging between 200 μm and 800 μm and oscillated by shear from the in-plane oscillation of the top plate. The spheres lined up across the velocity direction in the Newtonian silicon solution and with the velocity direction in the viscoelastic solution.

The robust tendency of small particles from nanometers to centimeters to chain in all kinds of motions must be associated with a powerful and local feature of particle-fluid interactions. We argue that the chaining of spherical particles is a consequence of the same dynamics that controls the orientation of long bodies moving relative to the stream, across the stream in Newtonian fluids and along the stream in viscoelasatic fluids. This dynamics is mainly controlled by a reversal of the normal stress at a point of stagnation.

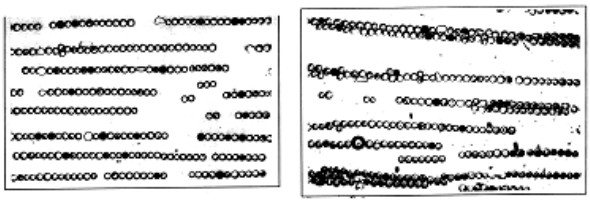

Fig. 20.5. 10% suspension of glass spheres (60-70 μm) in a polyisobutylene solution. (a) After movement on the top plate back and forth. (b) After further movement. The lines of spheres in (a) are more or less equally spaced. Further association is observed in (b) where two lines come together. (Michele et al. 1977)

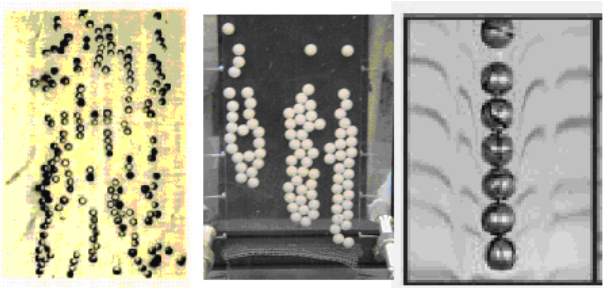

Fig. 20.6. Flow induced microstructure. Spheres line up in the direction of flow (a) Extensional flow, (60-70 μm spheres) (b) fluidization (3 cm spheres) and (c) sedimentation (3 cm spheres) in a 1% aqueous PEO solution.

20.8 Potential flow over a sphere for a second order fluid

We consider the potential of a uniform flow of a second order fluid past a sphere. The calculation is similar to that in Section 20.2.3. Bernoulli's Equation (20.5.4) is used to obtain the pressure at the surface of the sphere

$$p = p_\infty + \left(\frac{27}{2}\alpha_1 + 9\alpha_2\right)\frac{U^2}{a^2}\left(1 + 2\cos^2\theta\right) + \frac{\rho}{2}U^2\left(1 - \frac{9}{4}\sin^2\theta\right), \tag{20.8.1}$$

where p_∞ is the pressure at infinity. The normal stress T_{rr} at the surface of the sphere is calculated from (20.5.5) and expressed in a dimensionless form

$$T^*_{rr} = \frac{T_{rr} + p_\infty}{\rho U^2/2} = \left(\frac{9}{4}\sin^2\theta - 1\right) - \frac{12}{R_e}\cos\theta + \frac{\alpha_1}{\rho a^2}\left(36\sin^2\theta - 9\right) + 18\frac{\alpha_2}{\rho a^2}\cos^2\theta, \tag{20.8.2}$$

where $R_e = \rho U a/\mu$ is the Reynolds number. The viscous normal stress should be zero at a solid boundary in a Newtonian fluid or an Oldroyd-B fluid; the viscous effect on the normal stress is hidden in the pressure. The viscous contribution to the pressure at the surface of a sphere in a Stokes flow of Newtonian fluid is (Panton 1984, p. 646)

$$\frac{p - p_\infty}{\rho U^2/2} = \frac{3}{R_e}\cos\theta. \tag{20.8.3}$$

In (20.8.2) we have a viscous contribution to the normal stress $(12/R_e)\cos\theta$ which is four times the Stokes value $(3/R_e)\cos\theta$.

We compute the normal stress (20.8.2) for the liquid M1 with a density $\rho = 0.895$ g/cm^3, $\alpha_1 = -3$ and $\alpha_2 = 5.34$ g/cm (Hu *et al.* 1990) as an example. We plot the dimensionless normal stress T^*_{rr} as a function of the angle θ in Fig. 20.7.

At the stagnation points of a sphere [$r = a,\ \theta = 0$ or π], the normal stresses are, respectively

$$\frac{T_{rr} + p_\infty}{\rho U^2/2} = \left[-1 + \frac{9\left(2\alpha_2 - \alpha_1\right)}{\rho a^2}\right] \mp \frac{12}{R_e}. \tag{20.8.4}$$

The viscous contribution gives rise to compression $-12/R_e$ at front stagnation point and to tension $12/R_e$ at the rear. The stress due to inertia and viscoelasticity is the same at $\theta = 0$ and $\theta = \pi$ and is a tension when

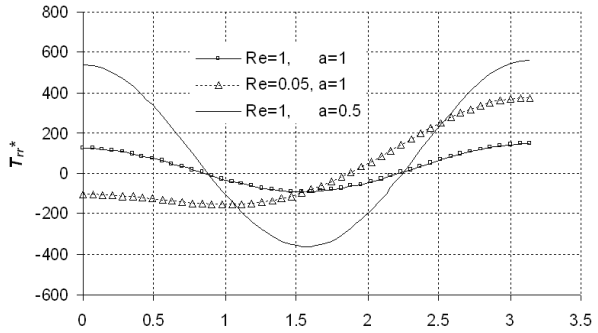

Fig. 20.7. The dimensionless normal stress T_{rr}^* as a function of the angle θ. Parameters of the liquid M1 are used in the calculation: $\rho = 0.895$ g/cm^3, $\alpha_1 = -3$ and $\alpha_2 = 5.34$ g/cm. The three curves in the figure correspond to $R_e = 1$, $a = 1$ cm; $R_e = 0.05$, $a = 1$ cm; and $R_e = 1$, $a = 0.5$ cm, respectively.

$9\,(2\alpha_2 - \alpha_1) > \rho a^2$. The quantity $2\alpha_2 - \alpha_1$ is strongly positive; for example, $2\alpha_2 - \alpha_1 = 13.68$ (g/cm) for the liquid M1. Hence, if a^2 is not too large the stress at the stagnation points is a tension, reversing the compression due to inertia.

Figure 20.7 shows that when viscous effects are dominant ($R_e = 0.05$, $a = 1$ cm), the stress is compression at the leading edge and tension at the trailing edge. When the viscoelastic effects are important ($R_e = 1$, $a = 1$ cm and $R_e = 1$, $a = 0.5$ cm), the stress is tension at both stagnation points. The normal stress on the sphere with $a = 0.5$ cm is much stronger than that on the sphere with $a = 1$ cm, because the viscoelastic effects are proportional to $1/a^2$. The distribution of normal stresses, especially the tension at the trailing edge, shown in Fig. 20.7 is compatible with the cusp shape of gas bubbles rising in viscoelastic fluids (see Section 20.11).

A point of stagnation on a stationary body in potential flow is a unique point at the end of a dividing streamline at which the velocity vanishes. In a viscous fluid all the points on the boundary of a stationary body have a zero velocity but the dividing streamline can be found and it marks the place of zero shear stress near which the velocity is small. The stagnation pressure makes sense even in a viscous fluid where the high pressure of the potential flow outside the boundary layer is transmitted right through the boundary layer to the body. It is a good idea to look for the dividing streamlines where the shear stress vanishes in any analysis of the flow pattern around the body.

20.9 Potential flow over an ellipse

Potential flow over an ellipse is a classical problem in airfoil theory. The solutions are most easily expressed in terms of complex functions of a complex variable (Lamb 1932, Milne-Thomson 1968). Hence, we shall use this potential flow solution and obtain the pressure and the normal stress for a second order fluid as a composition of derivatives of that solution. Two-dimensional potential flows around bodies admit the addition of circulation which we have here put to zero.

The complex potential for the flow over an ellipse given by

$$\frac{x^2}{a^2} + \frac{y^2}{b^2} = 1 \tag{20.9.1}$$

is (Milne-Thomson 1968, §6.31)

$$\omega = -\frac{1}{2}U(a+b)\left[\frac{\mathrm{e}^{-\mathrm{i}\alpha}\left(z+\sqrt{z^2-c^2}\right)}{a+b} + \frac{\mathrm{e}^{\mathrm{i}\alpha}\left(z-\sqrt{z^2-c^2}\right)}{a-b}\right] \tag{20.9.2}$$

where z is the complex variable, α is the angle of attack, a and b are the semi-axes of the ellipse and $c^2 = a^2 - b^2$. We plot the streamlines of the flow with the angle of attack $\alpha = 0°$ and $60°$ in Fig. 20.8.

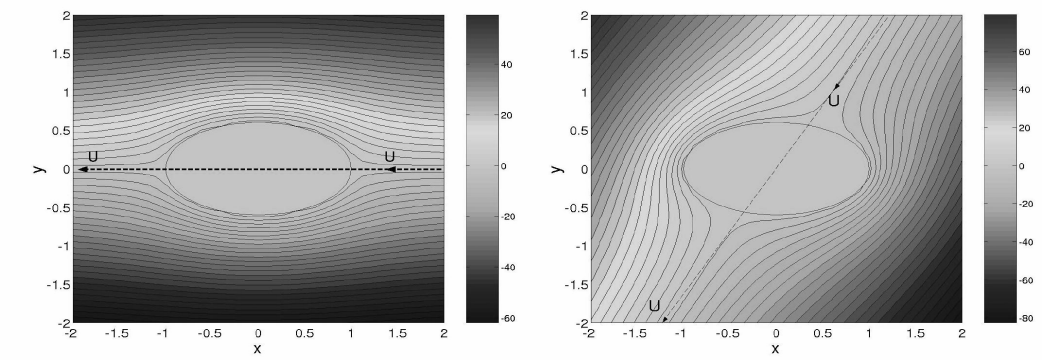

(a) (b)

Fig. 20.8. The streamlines of the flow over an ellipse. (a) The angle of attack $\alpha = 0°$; (b) $\alpha = 60°$.

The velocities are

$$u = \frac{1}{2}\left(\frac{\mathrm{d}\omega}{\mathrm{d}z} + \frac{\mathrm{d}\bar{\omega}}{\mathrm{d}\bar{z}}\right), \quad v = \frac{i}{2}\left(\frac{\mathrm{d}\omega}{\mathrm{d}z} - \frac{\mathrm{d}\bar{\omega}}{\mathrm{d}\bar{z}}\right). \tag{20.9.3}$$

$$\mathbf{L} = \nabla \boldsymbol{u} = \begin{bmatrix} \partial u/\partial x & \partial v/\partial x \\ \partial u/\partial y & \partial v/\partial y \end{bmatrix} \tag{20.9.4}$$

and

$$\mathbf{A} = \mathbf{L} + \mathbf{L}^T = \begin{bmatrix} n & s \\ s & -n \end{bmatrix} \tag{20.9.5}$$

where $n = \frac{\mathrm{d}^2\omega}{\mathrm{d}z^2} + \frac{\mathrm{d}^2\bar{\omega}}{\mathrm{d}\bar{z}^2}$ and $s = \mathrm{i}\left(\frac{\mathrm{d}^2\omega}{\mathrm{d}z^2} - \frac{\mathrm{d}^2\bar{\omega}}{\mathrm{d}\bar{z}^2}\right)$. It follows that

$$\mathbf{A}^2 = \left(n^2 + s^2\right)\mathbf{1} \text{ and } \mathrm{tr}\mathbf{A}^2 = 2\left(n^2 + s^2\right). \tag{20.9.6}$$

Letting U and p_∞ be the velocity and pressure at infinity, respectively, we find the pressure by (20.5.4)

$$p = p_\infty + \frac{\rho}{2}U^2 - \frac{\rho}{2}\frac{\mathrm{d}\omega}{\mathrm{d}z}\frac{\mathrm{d}\bar{\omega}}{\mathrm{d}\bar{z}} + (3\alpha_1 + 2\alpha_2)\frac{1}{2}\left(n^2 + s^2\right). \tag{20.9.7}$$

The stress can then be calculated using (20.5.5); after some arrangement, we find

$$\begin{aligned} \mathbf{T} &= \left[-p_\infty - \frac{\rho}{2}U^2 + \frac{\rho}{2}\frac{\mathrm{d}\omega}{\mathrm{d}z}\frac{\mathrm{d}\bar{\omega}}{\mathrm{d}\bar{z}} - \frac{1}{2}\alpha_1\left(n^2 + s^2\right)\right]\mathbf{1} + \mu\begin{bmatrix} n & s \\ s & -n \end{bmatrix} \\ &\quad + \alpha_1 u\begin{bmatrix} k & q \\ q & -k \end{bmatrix} + \alpha_1 v\begin{bmatrix} q & -k \\ -k & -q \end{bmatrix} \end{aligned} \tag{20.9.8}$$

where $k = \frac{\mathrm{d}^3\omega}{\mathrm{d}z^3} + \frac{\mathrm{d}^3\bar{\omega}}{\mathrm{d}\bar{z}^3}$ and $q = \mathrm{i}\left(\frac{\mathrm{d}^3\omega}{\mathrm{d}z^3} - \frac{\mathrm{d}^3\bar{\omega}}{\mathrm{d}\bar{z}^3}\right)$. Equation (20.9.8) applies to any two-dimensional flow that can be represented by a complex potential ω. We draw the readers' attention to the fact that α_2 does not appear in the expression for the stress in two-dimensional cases, which has been reported in Joseph 1992.

We are interested in the normal stress on the surface of the ellipse. The unit normal vector on the surface is

$$\boldsymbol{n} = \frac{\frac{x}{a^2}\boldsymbol{e}_x + \frac{y}{b^2}\boldsymbol{e}_y}{(x^2/a^4 + y^2/b^4)^{1/2}}. \tag{20.9.9}$$

The normal stress is calculated from $T_{nn} = \boldsymbol{n}\cdot\mathbf{T}\cdot\boldsymbol{n}$.

20.9.1 Normal stress at the surface of the ellipse

We present the results for the normal stress on the ellipse in this section. Besides the angle of attack, there are six relevant parameters: ρ, U, μ, a, b, and α_1 in this problem. Three dimensionless parameters can be

constructed:

$$R_e = \frac{\rho U a}{\mu}, \quad \frac{-\alpha_1}{\rho a^2}, \text{ and } \frac{a}{b}. \tag{20.9.10}$$

Note that the Deborah number can be defined as $D_e = \frac{-\alpha_1}{\mu}\frac{U}{a}$ and $\frac{-\alpha_1}{\rho a^2} = D_e/R_e$. We shall see later that the parameter $-\alpha_1/\left(\rho a^2\right)$ appears in the expressions for the normal stresses at the stagnation points. Therefore we use the parameter $-\alpha_1/\left(\rho a^2\right)$ rather than the Deborah number. The dimensionless normal stress is

$$T^*_{nn} = \frac{T_{nn} + p_\infty}{\rho U^2/2}. \tag{20.9.11}$$

The effects of the three dimensionless parameters on the normal stress at the surface of the ellipse are studied in flows of a zero attack angle. We can obtain explicit expressions for the normal stresses at the stagnation points, from which the effects of the three parameters can be understood readily. Such expressions are not obtained for an arbitrary point on the ellipse surface, instead, we calculate the numerical values of stress and present the plots for the distribution of the normal stress.

At the front stagnation point where $z = a$,we have

$$u = v = 0, \quad n = -2U(a+b)/b^2 \text{ and } s = 0. \tag{20.9.12}$$

Inserting (20.9.12) into (20.9.8) and noting that $T_{nn} = T_{xx}$, we obtain the dimensionless normal stress at the front stagnation point

$$T^*_{nn}(\theta = 0) = -1 + \frac{-\alpha_1}{\rho a^2} 4\left(1 + \frac{b}{a}\right)^2 \frac{a^4}{b^4} - \frac{4}{R_e}\left(1 + \frac{b}{a}\right)\frac{a^2}{b^2}. \tag{20.9.13}$$

Similarly, we can find the dimensionless normal stress at the rear stagnation point

$$T^*_{nn}(\theta = \pi) = -1 + \frac{-\alpha_1}{\rho a^2} 4\left(1 + \frac{b}{a}\right)^2 \frac{a^4}{b^4} + \frac{4}{R_e}\left(1 + \frac{b}{a}\right)\frac{a^2}{b^2}. \tag{20.9.14}$$

The difference between the two stresses is

$$T^*_{nn}(\theta = \pi) - T^*_{nn}(\theta = 0) = \frac{8}{R_e}\left(1 + \frac{b}{a}\right)\frac{a^2}{b^2}. \tag{20.9.15}$$

The normal stresses (20.9.12) and (20.9.13) are analogous to the normal stress (20.8.4) at the stagnation points in the sphere case, in the sense that they are all composed of the inertia, viscous and viscoelastic terms. Here the viscoelastic term $\frac{-\alpha_1}{\rho a^2} 4\left(1 + \frac{b}{a}\right)^2 \frac{a^4}{b^4}$ gives rise to extension at both of the stagnation points; the viscous term $\frac{4}{R_e}\left(1 + \frac{b}{a}\right)\frac{a^2}{b^2}$ leads to compression at the front stagnation point and extension at the rear stagnation point.

20.9.2 The effects of the Reynolds number

We calculate the normal stress at the surface of the ellipse in flows where $-\alpha_1/\left(\rho a^2\right)$ and a/b are fixed at 3 and 1.67 respectively and the Reynolds number changes from 0.01 – 100. In Fig. 20.9, we plot T^*_{nn} at the front and rear stagnation points as functions of the Reynolds number. The stress at the front stagnation point changes from compression to extension as the Reynolds number increases. The critical Reynolds number, at which $T^*_{nn} = 0$ at the front stagnation point, is 0.075, as shown in Fig. 20.9. Equation (20.9.15) indicates that the difference between the two normal stresses vanishes as the Reynolds number tends to infinity; the asymptotic value of the two stresses is

$$T^*_{nn}(R_e \to \infty,\ -\alpha_1/\left(\rho a^2\right) = 3,\ a/b = 1.67) = 236.07.$$

The distribution of the normal stress at the surface is plotted in Fig. 20.10 for flows with Reynolds numbers 0.05 and 1. We notice that the stress is compression at the front stagnation point and extension at the rear stagnation point when $R_e = 0.05$; however, the stress is tension at both of the two stagnation points when $R_e = 1$.

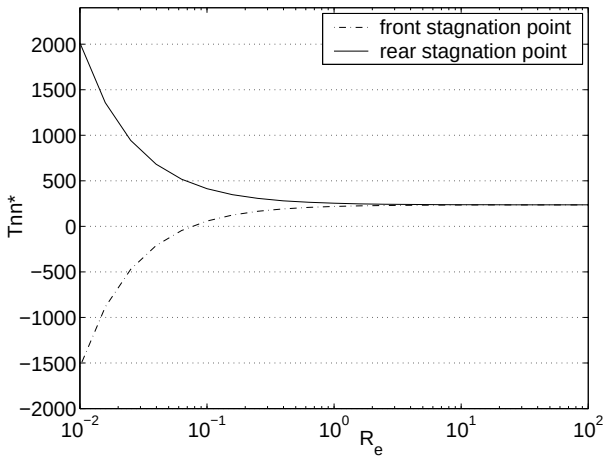

Fig. 20.9. The dimensionless normal stresses T^*_{nn} at the front and rear stagnation points as functions of the Reynolds number. The other two parameters are fixed: $-\alpha_1/\left(\rho a^2\right) = 3$ and $a/b = 1.67$.

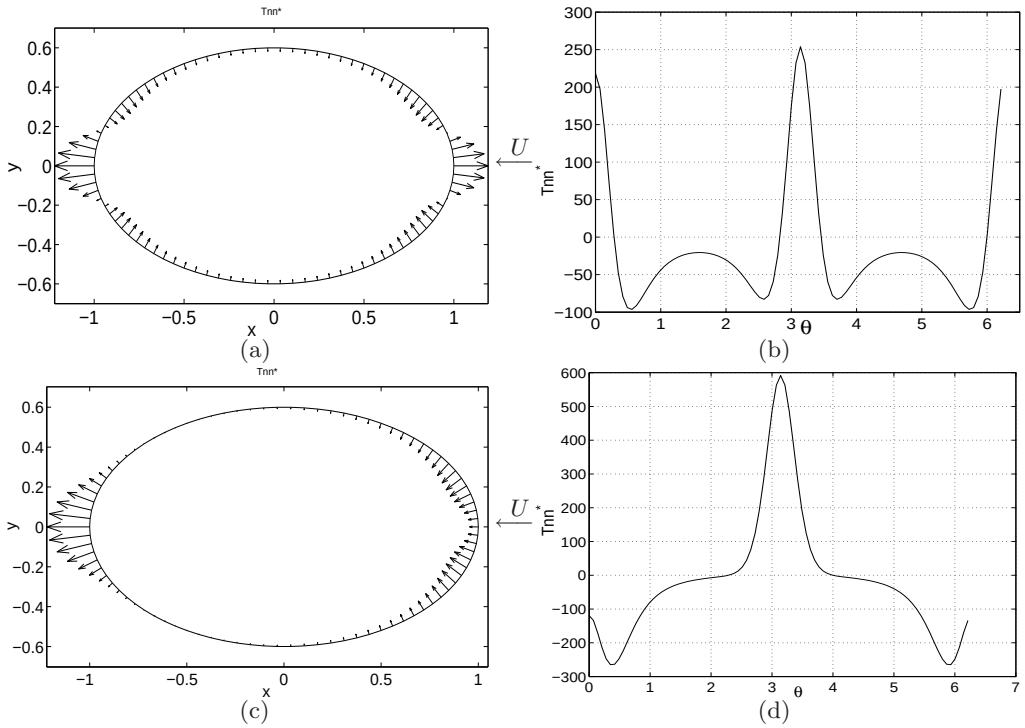

Fig. 20.10. The distribution of the dimensionless normal stress T^*_{nn} at the surface of the ellipse in flows with $-\alpha_1/\left(\rho a^2\right) = 3$ and $a/b = 1.67$. The Reynolds number is 1.0 in figures (a) and (b), and is 0.05 in figures (c) and (d). The normal stress is represented by vectors at the surface of the ellipse in (a) and (c), and is plotted against the polar angle θ in (b) and (d).

20.9.3 The effects of $-\alpha_1/\left(\rho a^2\right)$

The two normal stresses at stagnation points are plotted against the parameter $-\alpha_1/\left(\rho a^2\right)$ in Fig. 20.11; the other two parameters are fixed: $R_e = 0.1$ and $a/b = 1.67$. The difference between the two stresses is independent of the parameter $-\alpha_1/\left(\rho a^2\right)$, as can be seen from (20.9.15). This difference is 355.6 when $R_e = 0.1$ and $a/b = 1.67$. The critical value of $-\alpha_1/\left(\rho a^2\right)$, at which $T^*_{nn} = 0$ at the front stagnation point, is 2.26.

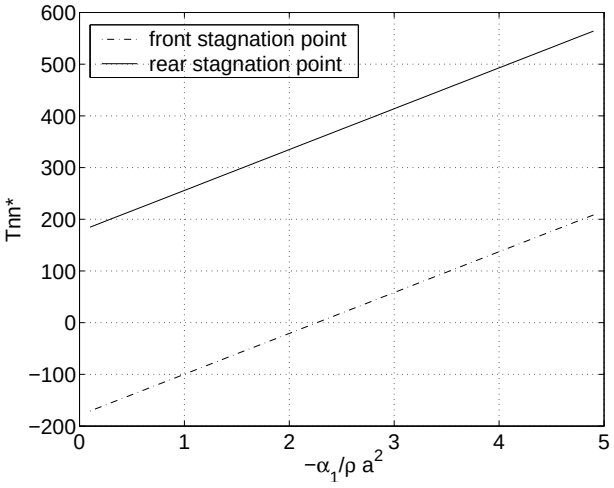

Fig. 20.11. The dimensionless normal stresses T^*_{nn} at the front and rear stagnation points as functions of the parameter $-\alpha_1/\left(\rho a^2\right)$. The other two parameters are fixed: $R_e = 0.1$ and $a/b = 1.67$.

20.9.4 The effects of the aspect ratio

We change the aspect ratio from 1.1 to 10 and compute the normal stress on the surface of the ellipse; the other two parameters are fixed: $R_e = 0.1$ and $-\alpha_1/\left(\rho a^2\right) = 3$. The two stresses at the stagnation points are plotted against the aspect ratio in Fig. 20.12; The values of the stresses change dramatically with the aspect ratio because of the a^4/b^4 term in (20.9.13) and (20.9.14). The stress at the front stagnation point changes from compression to extension as a/b increases; when $a/b = 1.40$, $T^*_{nn} = 0$ at the front stagnation point. (The negative values are not shown on the semi-log plot in Fig. 20.12).

The normal stress distribution at the surface is plotted in Fig. 20.13 for flows with $a/b = 5.0$ and 1.1. It can be seen that in the flow with the higher aspect ratio, the ellipse is under very high extensional stresses at both of the stagnation points. The stress at the front stagnation point is compression when $a/b = 1.1$, which implies that the front nose of a gas bubble will be flattened.

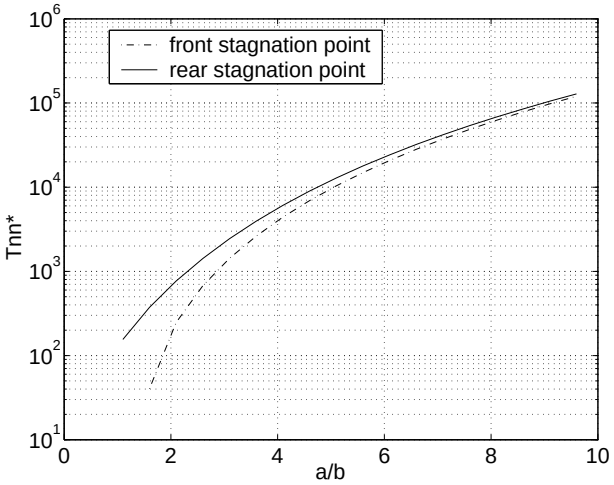

Fig. 20.12. The dimensionless normal stresses T^*_{nn} at the front and rear stagnation points as functions of the aspect ratio a/b. The other two parameters are fixed: $R_e = 0.1$ and $-\alpha_1/\left(\rho a^2\right) = 3$.

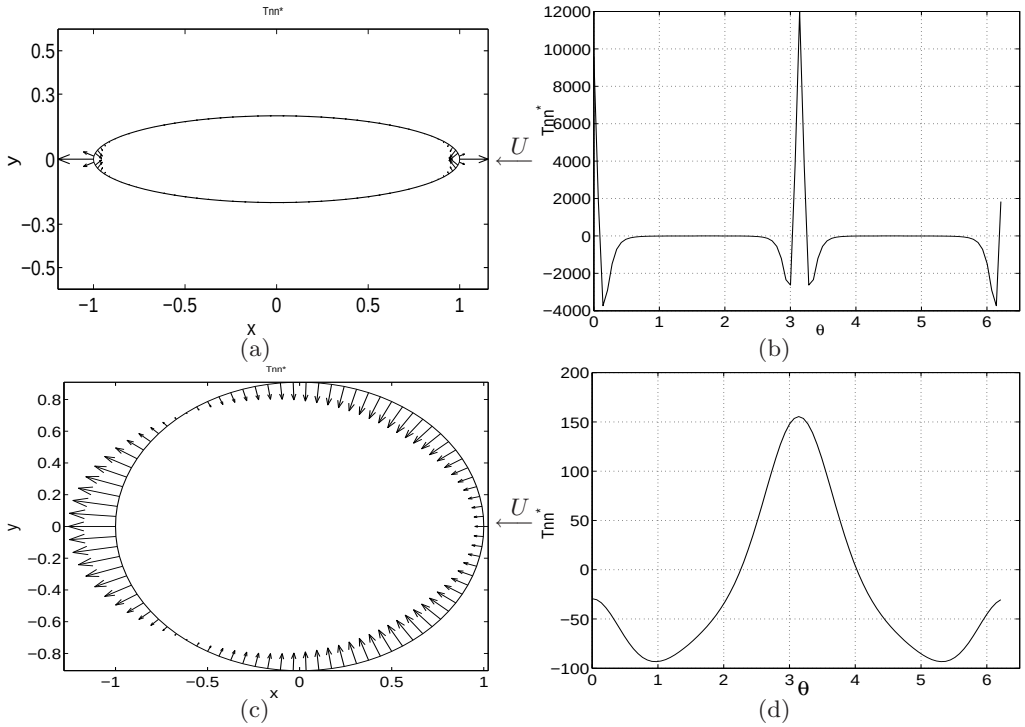

Fig. 20.13. The distribution of the dimensionless normal stress T^*_{nn} at the surface of the ellipse in flows with $R_e = 0.1$ and $-\alpha_1/\left(\rho a^2\right) = 3$. The aspect ratio is 5.0 in figures (a) and (b), and is 1.1 in figures (c) and (d). The normal stress is represented by vectors at the surface of the ellipse in (a) and (c), and is plotted against the polar angle θ in (b) and (d).

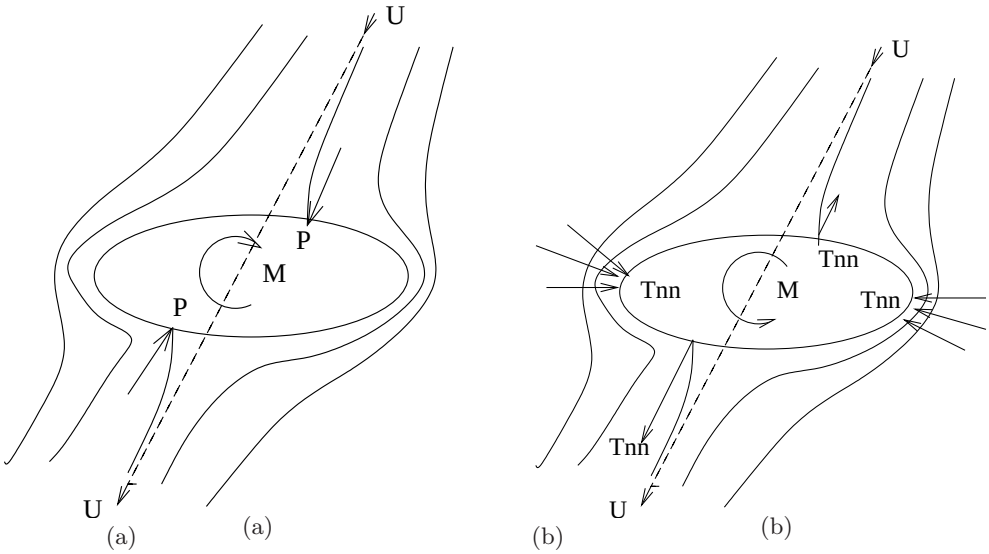

Fig. 20.14. The moment on the ellipse in potential flow. (a) In an inviscid fluid, the high pressures at the stagnation points turn the ellipse broadside-on (across the stream); (b) In a second order fluid, the normal stresses at the two edges where the streamlines are most crowded are compressive and tend to turn the ellipse into the stream. At the two stagnation points, the stresses may change from compression to tension. Here we illustrate the situation in which the stress is compression at the front stagnation point and tension at the rear stagnation point; this pair of stresses gives rise to the moment which tends to turn the ellipse into the stream. Our calculation shows that the resultant moment of the normal stress tends to turn the broad side of the ellipse into the stream when inertia is not dominant.

20.10 The moment on the ellipse

Long bodies falling in a viscoelastic fluid often turn into the streamwise direction (Liu and Joseph 1993). We calculate the dimensionless moment by the normal stress on the ellipse

$$M^* = \frac{M}{\rho U^2 a^2/2} = \frac{\oint \boldsymbol{x} \wedge (T_{nn}\boldsymbol{n})\ \mathrm{d}l}{\rho U^2 a^2/2}. \tag{20.10.1}$$

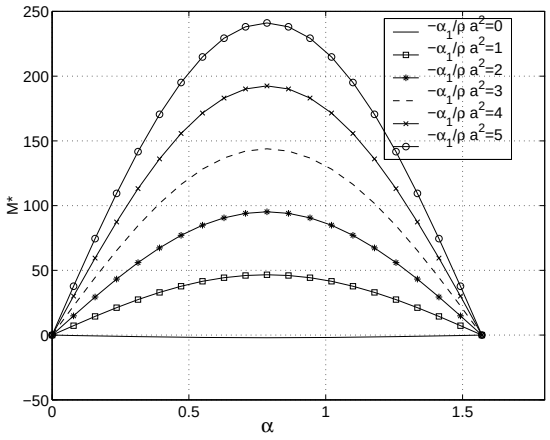

Fig. 20.15. The moment on the ellipse by the normal stress as a function of the attack angle α in the range $[0,\ \pi/2]$. The six curves correspond to six values of the parameter $-\alpha_1/\left(\rho a^2\right)$: 0, 1, 2, 3, 4 and 5; the aspect ratio is fixed at $a/b = 1.67$.

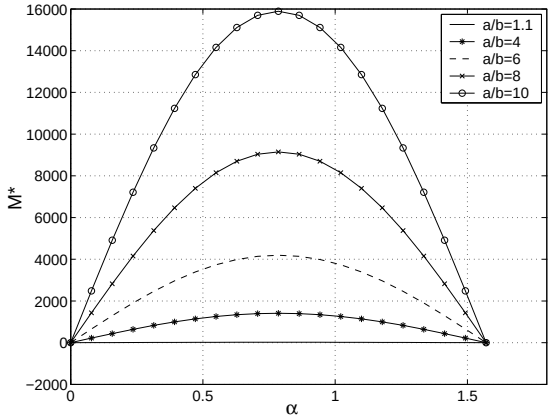

Fig. 20.16. The moment on the ellipse by the normal stress as a function of the attack angle α in the range $[0,\ \pi/2]$. The five curves correspond to five values of the aspect ratio $a/b = 1.1$, 4, 6, 8 and 10; the parameter $-\alpha_1/\left(\rho a^2\right)$ is fixed at 3.

In a Newtonian fluid, the moment can be calculated using the theorem of Blasius and the dimensionless moment is

$$M^* = -2\pi\left(1 - a^2/b^2\right)\sin\alpha\cos\alpha, \tag{20.10.2}$$

which does not depend on the Reynolds number. Our calculation shows that the conclusion is also true in a second order fluid: the dimensionless moment does not depend on the Reynolds number; the parameter $-\alpha_1/\left(\rho a^2\right)$ and the aspect ratio a/b are relevant parameters when the moment is concerned.

We plot the dimensionless moment on the ellipse by the normal stress as a function of the attack angle α in the range $[0, \pi/2]$ in Fig. 20.15. Six values of the parameter $-\alpha_1/\left(\rho a^2\right)$, from 0 to 5, are investigated. The curve corresponding to $-\alpha_1/\left(\rho a^2\right) = 0$ in Fig. 20.15 is in agreement with (20.10.2), which is the moment in a Newtonian fluid. The moment on the ellipse is negative in a Newtonian fluid and turns the ellipse broadside-on to the stream. When the parameter – $\alpha_1/\left(\rho a^2\right)$ is larger, the moment on the ellipse becomes positive and tends to align the broad side of the ellipse with the streamwise direction. Figure 20.15 also shows that the magnitude of the moment reaches its largest value when $\alpha = \pi/4$, which also occurs in a Newtonian fluid.

We show the effects of the aspect ratio on the moment in Fig. 20.16. The five curves correspond to five values of the aspect ratio a/b: 1.1, 4, 6, 8 and 10; the parameter $-\alpha_1/\left(\rho a^2\right)$ is fixed at 3. It can be seen that as the aspect ratio increases, the magnitude of the moment increases to huge values. Hence, long slim bodies turn into the streamwise direction quickly in viscoelastic fluids.

20.11 The reversal of the sign of the normal stress at stagnation points

In Sections 20.8 and 20.9, we have showed that the normal stresses at the stagnation points on a sphere or an ellipse in a second order fluid can be tension, opposite to the high compressive pressures at the stagnation points in Newtonian fluid. This reversal of the sign of the normal stress has significant effects on the behavior of particles and bubbles in Newtonian and viscoelastic fluids.

In Newtonian fluids, long bodies in a uniform flow are turned to the orientation in which their long or broad sides are perpendicular to the stream by the high pressures at stagnation points (see Fig. 20.14.a).

In viscoelastic fluids, long bodies in a uniform flow often turn into the streamwise direction as we discussed in Section 20.10 (see also Liu and Joseph 1993, Joseph and Feng 1996, Huang, Hu and Joseph 1997). The extensional normal stresses at the stagnation points in viscoelastic fluids contribute to the moment which turns the long bodies into the stream (see Fig. 20.14.b and the caption). Long chains of spherical bodies parallel with the stream are in evidence in sedimentation and fluidization flows of viscoelastic fluids; such configurations are opposite to those observed in Newtonian fluids. Another unusual phenomenon in viscoelastic fluids is the two-dimensional cusp at the trailing edge of a rising air bubble (Liu *et al.* 1995). Below a critical capillary number, an air bubble rising in a viscoelastic fluid adopts the shape with a cusp point in one view and a spade edge in the orthogonal view. Figures 20.7, 20.10(c) and 20.13(c) show situations in which the normal stress is compression at the leading edge and tension at the trailing edge; the leading edge is flattened and the trailing edge is extended, tending to the cusped trailing edge observed in experiments. Our calculation on a smooth sphere or an ellipse cannot lead to the exact cusp shape. However, the calculation shows that the normal stress computed on viscoelastic potential agrees with the experiment qualitatively, much better than the pressure which is the only normal force that can act on the body in inviscid potential flow.

20.12 Flow past a flat plate

The flow past an ellipse degenerates to the flow past a flat plate when $b = 0$. The complex potential is

$$\omega = \begin{cases} -U(z\cos\alpha - \mathrm{i}\sqrt{z^2-a^2}\sin\alpha) & \text{up-stream to the plate;} \\ -U(z\cos\alpha + \mathrm{i}\sqrt{z^2-a^2}\sin\alpha) & \text{down-stream to the plate.} \end{cases} \tag{20.12.1}$$

The velocities at the upper and lower surfaces of the plate are, respectively

$$u = -U\left(\cos\alpha - \frac{x\sin\alpha}{\sqrt{a^2-x^2}}\right), \quad v = 0, \quad \text{upper surface;} \tag{20.12.2}$$

$$u = -U\left(\cos\alpha + \frac{x\sin\alpha}{\sqrt{a^2-x^2}}\right), \quad v = 0, \quad \text{lower surface.} \tag{20.12.3}$$

The stagnation points at the upper and lower surfaces are $x = a\cos\alpha$ and $x = -a\cos\alpha$, respectively. The dimensionless normal stresses at the two stagnation points are

$$\frac{T_{nn}+p_\infty}{\rho U^2/2}(x = a\cos\alpha) = -1 + \frac{-\alpha_1}{\rho a^2}\frac{4}{\sin^4\alpha} - \frac{4}{R_e\sin^2\alpha}, \tag{20.12.4}$$

$$\frac{T_{nn}+p_\infty}{\rho U^2/2}(x = -a\cos\alpha) = -1 + \frac{-\alpha_1}{\rho a^2}\frac{4}{\sin^4\alpha} + \frac{4}{R_e\sin^2\alpha}. \tag{20.12.5}$$

These stresses are degenerate cases of (20.9.13) and (20.9.14), which are the stresses at stagnation points in the flow past an ellipse. In (20.12.4) and (20.12.5), the viscoelastic term $\dfrac{-\alpha_1}{\rho a^2}\dfrac{4}{\sin^4\alpha}$ gives rise to extension at both of the stagnation points; the viscous term $\dfrac{4}{R_e}\dfrac{1}{\sin^2\alpha}$ leads to compression at the front stagnation point and extension at the rear stagnation point.

20.13 Flow past a circular cylinder with circulation

The complex potential for the flow past a circular cylinder with circulation is (Milne-Thomson §7.12)

$$\omega = -U(z + a^2/z) - \mathrm{i}\kappa \log(z/a) \tag{20.13.1}$$

where κ is the strength of the circulation. A dimensionless parameter κ/aU can be introduced.

We calculate the stress using the potential (20.13.1) in a second order fluid. The stress at the surface of the cylinder, where $z = a\mathrm{e}^{\mathrm{i}\theta}$, are of interest. We find

$$u = -\sin\theta(2U\sin\theta + \kappa/a), \quad v = \cos\theta(2U\sin\theta + \kappa/a); \tag{20.13.2}$$

$$n = -4U\cos 3\theta/a + 2\kappa\sin 2\theta/a^2, \quad s = -(4U\sin 3\theta/a + 2\kappa\cos 2\theta/a^2); \tag{20.13.3}$$

$$k = 12U\cos 4\theta/a^2 - 4\kappa\sin 3\theta/a^3, \quad q = 12U\sin 4\theta/a^2 + 4\kappa\cos 3\theta/a^3 \tag{20.13.4}$$

at $z = a\mathrm{e}^{\mathrm{i}\theta}$ and the stress tensor is obtained by inserting (20.13.2) – (20.13.4) into (20.9.8). The dimensionless normal stress is given by

$$\begin{aligned}\frac{T_{nn} + p_\infty}{\rho U^2/2} = &\left[-1 + 4\sin^2\theta + \left(\frac{\kappa}{aU}\right)^2 + \frac{\kappa}{aU}4\sin\theta\right] - \frac{8}{R_e}\cos\theta \\ &+\frac{4\alpha_1}{\rho a^2}\left[-4 + 12\sin^2\theta + \left(\frac{\kappa}{aU}\right)^2 + \frac{\kappa}{aU}6\sin\theta\right]\end{aligned} \tag{20.13.5}$$

where the first term on the right hand side is the inertia term, which is the same as the inviscid pressure; the second term is the viscous term and the third term is the viscoelastic term.

The force and moment on the cylinder can be obtained by direct integration of the normal stress over the surface of the cylinder:

$$F_x = \int_0^{2\pi} T_{nn}\cos\theta \; a\mathrm{d}\theta = -4\pi\mu U, \tag{20.13.6}$$

$$F_y = \int_0^{2\pi} T_{nn}\sin\theta \; a\mathrm{d}\theta = 2\pi\kappa U(\rho + 6\alpha_1/a^2). \tag{20.13.7}$$

The moment is obviously zero. Equation (20.13.6) shows that the cylinder experiences a drag due to the viscosity; the drag would be zero if the shear stress were included in the integration. Equation (20.13.7) shows that the lift has a contribution from the viscoelastic effect in addition to the inviscid lift $2\pi\kappa\rho U$. Since α_1 is negative, the viscoelastic lift is opposite to the inviscid lift. When $-\alpha_1/\left(\rho a^2\right) = 1/6$, the total lift force is zero.

20.14 Potential flow of a second-order fluid over a tri-axial ellipsoid

Viana et al 2005 solved the problem of potential flow of a second-order fluid around a three-dimensional ellipsoid using general expressions in Lamb (1932), and the flow and stress fields are computed. The flow fields are determined by the harmonic potential but the stress fields depend on viscosity and the parameters of the second-order fluid. The stress fields on the surface of a tri-axial ellipsoid depend strongly on the ratios of principal axes and are such as to suggest the formation of gas bubble with a round flat nose and two-dimensional cusped trailing edge. A thin flat trailing edge gives rise to a large stress which makes the thin trailing edge thinner.

The main goal of the calculations of Viana et al 2005 for the second-order fluid model was to identify mechanisms which lead to "two-dimensional cusps"(see Fig. 20.17) at the trailing edge of a gas bubble rising in an unbounded liquid where axisymmetric solutions might be expected. They calculated the effects of viscosity, second-order viscoelasticity and inertia. The effects of viscoelasticity are opposite to the effects of inertia; under modest and realizable assumptions about the values of the second-order fluid parameters, the normal stresses

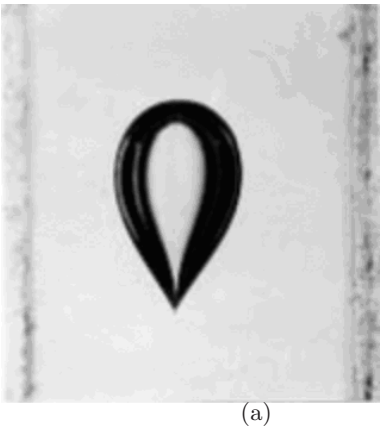

(a)

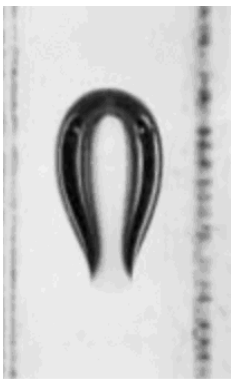

(b)

Fig. 20.17. Two orthogonal views showing the cusped (a) and broad (b) shape of the trailing edge of an air bubble (2 cm^3), rising in a viscoelastic liquid (S1). The two photographs are from Liu, Liao & Joseph (1995).

at points of stagnation change from compression to tension. The effect of inertia and elasticity are essentially symmetric in that they depend on squares of velocity and velocity gradients but the effects of viscosity are asymmetric.

For the rising gas bubbles, the effects of the second-order and viscous terms on the normal stress are such as to extend and flatten the trailing edge. These calculations suggest that "two-dimensional cusping" can be viewed as an instability in which a thin flat trailing edge gives rise to a large stress which makes the thin trailing edge even thinner.

20.15 The lift, drag and torque on an airfoil in foam modeled by the potential flow of a second-order fluid

We compute the irrotational streaming flow of a second-order fluid past a Joukowski airfoil. The pressure and extra stress are evaluated using the irrotational flow theory, and the lift, drag and torque on the airfoil are obtained by integration of the normal stress over the surface of the airfoil. Our calculation can give rise to a lift force opposite to what would be predicted from the classical theory of aerodynamics. The result is in qualitative agreement with the experiments of the flow of a foam past an airfoil by Dollet, Aubouy and Graner 2004.

20.15.1 Introduction

Dollet, Aubouy and Graner (G2004) (hereafter referred to as DAG2004) performed experiments of the flow of a foam past an airfoil. They observed a striking feature that the lift force on the airfoil is opposite to what would be predicted from the classical theory of aerodynamics. They argued that this inverse lift is due to the effect of elasticity of the foam.

Besides the inverse lift on an airfoil, many other unusual features of flows observed in viscoelastic fluids but not in Newtonian fluids can be understood by considering the competition between the effects of inertia and viscoelasticity; for example, the stable orientation of a sedimenting long particle (Liu and Joseph 1993, Galdi *et al.* 2002, Wang *et al.* 2004), chaining of particles in extensional and shear flows and in sedimentation and fluidization (Michele *et al.* 1977, Joseph 1996, 2000, chap. 7), and the two-dimensional cusp at the trailing edge of a rising air bubble (Liu, Liao and Joseph 1995). Our understanding of these phenomena relies on two pillars: a viscoelastic "pressure" generated by normal stress due to shear (Joseph and Feng 1996) and a change in the sign of the normal stress at points of stagnation (Wang and Joseph 2004). These explanations are suggested by analysis of the second-order fluid model which arises asymptotically for motions which are slow and slowly varying.

Wang and Joseph (2004) considered the potential flow of a second-order fluid over a sphere or an ellipse and

calculated the normal stress at the surface. The irrotational normal stress depends in a significant way on the viscosity and viscoelastic parameters and produces torques on solid particles and deformations of gas bubbles which are in qualitative agreement with experiments. The stress $\mathbf{T}$ in an incompressible second-order fluid is given by

$$\mathbf{T} = -p\mathbf{1} + \mu\mathbf{A} + \alpha_1\mathbf{B} + \alpha_2\mathbf{A}^2, \tag{20.15.1}$$

where $\mathbf{A} = \mathbf{L} + \mathbf{L}^T$ is the symmetric part of the velocity gradient $\mathbf{L} = \nabla\boldsymbol{u}$,

$$\mathbf{B} = \partial\mathbf{A}/\partial t + (\boldsymbol{u}\cdot\nabla)\,\mathbf{A} + \mathbf{A}\mathbf{L} + \mathbf{L}^T\mathbf{A}, \tag{20.15.2}$$

μ is the zero shear viscosity, $\alpha_1 = -n_1/2$ and $\alpha_2 = n_1 + n_2$ where $[n_1,\, n_2] = [N_1(\dot\gamma),\, N_2(\dot\gamma)]\,/\dot\gamma^2$ as $\dot\gamma \to 0$ are the constants obtained from the first and second normal stress differences.

In this work, we apply potential flow theory to the flow of a second-order fluid past an airfoil and compute the lift, drag and torque by integration of the normal stress over the surface of the airfoil. Our calculation can give the inverse lift as observed by DAG2004, but quantitative comparison between our results and the experimental ones does not yield good agreement; though foams are elastic, they are almost certainly not well described by a second-order fluid model. DAG2004 showed evidence that the inverse lift on an asymmetric object exists in a 0.5% by weight cellulose solution, which suggests that the inverse lift on an asymmetric object is a common feature in viscoelastic fluids, not only in foams. Our calculation provides a way for explicit analysis of the viscoelastic effects in such problems and offers partial explanation for the inverse lift. We regard the results using the potential flow of a second-order fluid as tentative and subject to ultimate validation by experiments and direct numerical simulation using other models.

20.15.2 Numerical method

We consider a uniform streaming flow with the velocity U_0 past a cambered airfoil at an angle of attack α. The calculation is carried out using dimensionless parameters. Following scales are used

$$[\mathit{length},\, \mathit{velocity},\, \mathit{pressure\,and\,stress},\, \mathit{time}] = [l,\, U_0,\, \frac{1}{2}\rho U_0^2,\, \frac{l}{U_0}], \tag{20.15.3}$$

where l is the length of the airfoil and ρ is the density of the fluid. There are two controlling parameters in this problem:

$$R_e = \frac{\rho U_0 l}{\mu}, \quad \beta = \frac{-\alpha_1}{\rho l^2}, \tag{20.15.4}$$

where R_e is the Reynolds number and $\beta * R_e$ would give the Deborah number. Only the normal stress $T_{nn} = -p + \tau_{nn}$ at the surface is considered and the shear stress is ignored. The lift, drag and torque coefficients are defined as

$$C_L = \frac{L}{\frac{1}{2}\rho U_0^2 l}, \quad C_D = \frac{D}{\frac{1}{2}\rho U_0^2 l}, \quad C_T = \frac{T}{\frac{1}{2}\rho U_0^2 l^2}. \tag{20.15.5}$$

All the variables in the rest part of this section are dimensionless.

The airfoil is obtained by the Joukowski transformation

$$z = \zeta + \frac{c^2}{\zeta}, \tag{20.15.6}$$

in conjunction with a circle in the ζ plane. The center of the circle is displaced a distance m from the origin at an angle δ from the x axis and it is in the second quadrant (see Fig. 20.18). Here m is assumed to be small compared with unity. The circumference of the circle passes through the critical point $\zeta = c$ for the Joukowski transformation, which corresponds to the sharp trailing edge of the airfoil in the z plane.

In the ζ plane, a generic point (r, θ) on the circle satisfies

$$a^2 = r^2 + m^2 - 2rm\cos(\delta - \theta), \tag{20.15.7}$$

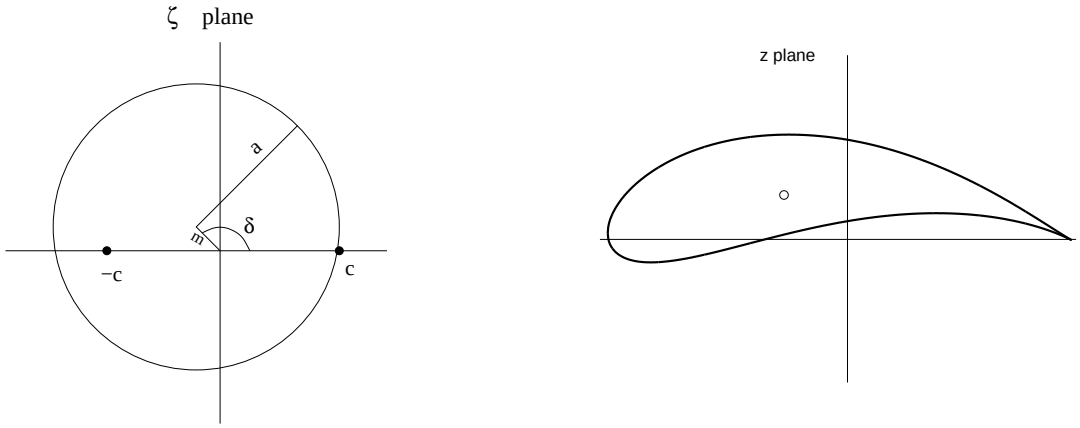

Fig. 20.18. The mapping planes for a Joukowski airfoil. In the ζ plane, the center of the circle is displaced a distance m from the origin at an angle δ from the x axis and it is in the second quadrant. The center of the mass in the z plane (x_0, y_0) is marked.

which gives rise to

$$r = m\cos(\delta - \theta) + \sqrt{a^2 - m^2\sin^2(\delta - \theta)}. \tag{20.15.8}$$

The critical point $(c, 0)$ is on the circle and satisfies

$$r(\theta = 0) = c = m\cos\delta + \sqrt{a^2 - m^2\sin^2\delta}. \tag{20.15.9}$$

The surface of the airfoil in the z plane is then given by

$$z = re^{\imath\theta} + \frac{c^2}{r}e^{-\imath\theta}, \tag{20.15.10}$$

or

$$x = \left(r + \frac{c^2}{r}\right)\cos\theta \quad \text{and} \quad y = \left(r - \frac{c^2}{r}\right)\sin\theta. \tag{20.15.11}$$

The length of the airfoil can be calculated from $x(\theta = 0) - x(\theta = \pi)$ with the aid of (20.15.8) and (20.15.11):

$$1 = m\cos\delta + 3\sqrt{a^2 - m^2\sin^2\delta} + \frac{\left(m\cos\delta + \sqrt{a^2 - m^2\sin^2\delta}\right)^2}{-m\cos\delta + \sqrt{a^2 - m^2\sin^2\delta}}. \tag{20.15.12}$$

Let $\dot{x} = \mathrm{d}x/\mathrm{d}\theta$ and $\dot{y} = \mathrm{d}y/\mathrm{d}\theta$, then the unit norm on the surface pointing outward from the airfoil can be written as

$$\mathbf{n} = n_x\mathbf{e}_x + n_y\mathbf{e}_y = \frac{\dot{y}\mathbf{e}_x - \dot{x}\mathbf{e}_y}{\sqrt{\dot{x}^2 + \dot{y}^2}}, \tag{20.15.13}$$

and

$$\mathrm{d}s = \sqrt{\dot{x}^2 + \dot{y}^2}\mathrm{d}\theta. \tag{20.15.14}$$

Among the four geometric parameters c, a, m and δ, we choose to prescribe m and δ, then compute c and a from (20.15.9) and (20.15.12), respectively.

The complex potential for a uniform flow past a circle with circulation at an angle of attack α in the ζ plane is

$$f(\zeta) = \left[(\zeta - me^{\imath\delta})e^{-\imath\alpha} + \frac{a^2e^{\imath\alpha}}{\zeta - me^{\imath\delta}}\right] + \frac{\imath\Gamma}{2\pi}\log\left(\frac{\zeta - me^{\imath\delta}}{a}\right). \tag{20.15.15}$$

The circulation Γ is determined by Kutta condition, which requires $\mathrm{d}f/\mathrm{d}\zeta = 0$ at the critical point $\zeta = c$. Calculation shows that

$$\Gamma = 4\pi\left(c\sin\alpha - m\cos\delta\sin\alpha + m\sin\delta\cos\alpha\right). \tag{20.15.16}$$

Equation (20.15.15) along with the inverse Joukowski transformation

$$\zeta = \frac{z}{2} \pm \sqrt{\frac{z^2}{4} - c^2} \tag{20.15.17}$$

gives the potential for the flow past an airfoil in the z plane. The velocities can be evaluated using the potential

$$u = \frac{1}{2}\left(\frac{\mathrm{d}f}{\mathrm{d}z} + \frac{\mathrm{d}\bar{f}}{\mathrm{d}\bar{z}}\right) \quad \text{and} \quad v = \frac{\imath}{2}\left(\frac{\mathrm{d}f}{\mathrm{d}z} - \frac{\mathrm{d}\bar{f}}{\mathrm{d}\bar{z}}\right), \tag{20.15.18}$$

where the overbar denotes conjugate variables. Wang and Joseph (2004) gave the expression for the stress of a second-order fluid evaluated using a two-dimensional potential flow solution

$$\mathbf{T} = \left[-p_\infty - 1 + u^2 + v^2 + \beta(n^2 + s^2)\right]\mathbf{1} + \frac{2}{R_e}\begin{bmatrix} n & s \\ s & -n \end{bmatrix} - 2\beta u \begin{bmatrix} k & q \\ q & -k \end{bmatrix} - 2\beta v \begin{bmatrix} q & -k \\ -k & -q \end{bmatrix}, \tag{20.15.19}$$

where

$$n = \frac{\mathrm{d}^2 f}{\mathrm{d}z^2} + \frac{\mathrm{d}^2 \overline{f}}{\mathrm{d}\overline{z}^2}, \qquad s = \imath\left(\frac{\mathrm{d}^2 f}{\mathrm{d}z^2} - \frac{\mathrm{d}^2 \overline{f}}{\mathrm{d}\overline{z}^2}\right), \tag{20.15.20}$$

$$k = \frac{\mathrm{d}^3 f}{\mathrm{d}z^3} + \frac{\mathrm{d}^3 \overline{f}}{\mathrm{d}\overline{z}^3}, \qquad q = \imath\left(\frac{\mathrm{d}^3 f}{\mathrm{d}z^3} - \frac{\mathrm{d}^3 \overline{f}}{\mathrm{d}\overline{z}^3}\right). \tag{20.15.21}$$

The normal stress at the surface of the airfoil can be computed from

$$T_{nn} = \mathbf{n} \cdot \mathbf{T} \cdot \mathbf{n}, \tag{20.15.22}$$

where $\mathbf{n}$ is given in (20.15.13). The drag and lift coefficients are obtained by integration of T_{nn} over the airfoil surface

$$C_D = \oint T_{nn} n_x \,\mathrm{d}s, \qquad C_L = \oint T_{nn} n_y \,\mathrm{d}s. \tag{20.15.23}$$

We compute the torque with respect to the center of the mass $z = (x_0, y_0)$ by integration

$$C_T = \oint [(x - x_0)n_y - (y - y_0)n_x] T_{nn} \,\mathrm{d}s. \tag{20.15.24}$$

20.15.3 Results

We use a Joukowski airfoil described in DAG2004, which can be obtain by setting $m = 0.0911$ and $\delta = 0.688\pi$ in our calculation. The angle of attack is fixed at $\alpha = 0$, in accordance with the experiments of DAG2004. Although the velocity is finite everywhere on the airfoil surface, the velocity gradients are singular at the front nose and trailing edge (corresponding to $\theta = \pi$ and $\theta = 0$, respectively). The numerical integrations (20.15.23) and (20.15.24) cannot converge near these singular points when $\beta \neq 0$ and they have to be excluded from the integration interval. A small number Δ is introduced and the integrations are performed in the following intervals

$$0 + \Delta \leq \theta \leq \pi - \Delta, \quad \text{and} \quad \pi + \Delta \leq \theta \leq 2 * \pi - \Delta. \tag{20.15.25}$$

First we test the inviscid Newtonian fluid. Classical potential flow theory for inviscid fluid shows that the drag is zero (D'Alembert's paradox), and the lift coefficient is

$$C_L = \frac{\rho U_0 \Gamma}{\frac{1}{2}\rho U_0^2 l} = 2\frac{\Gamma}{U_0 l} = 1.90302, \tag{20.15.26}$$

where the dimensionless expression for the circulation (20.15.16) has been used for the calculation.† The torque

† Currie (1974, §4.18) used approximations to the first order of m and obtained another expression for the lift coefficient on the airfoil in an inviscid fluid

$$C_L = 2\pi(1 - m\cos\delta)\sin(\alpha + 4m\sin\delta) = 1.969, \tag{20.15.27}$$

which is close to the exact lift coefficient (20.15.26).

on the airfoil with respect to the origin $z = 0$ can be computed using the Blasius' theorem (written in dimensionless form)

$$C_T^0 = \oint (xn_y - yn_x)T_{nn}\,\mathrm{d}s = -\mathrm{Real}\left(\oint zW^2\,\mathrm{d}z\right) = -0.0965562, \tag{20.15.28}$$

where $W = \mathrm{d}f(z)/\mathrm{d}z$ is the complex velocity. Then the torque with respect to the center of the mass ($x_0 = -0.1362$, $y_0 = 0.0978$)can be obtained

$$\begin{aligned} C_T &= \oint (xn_y - yn_x)T_{nn}\,\mathrm{d}s - x_0 \oint n_y T_{nn}\,\mathrm{d}s + y_0 \oint n_x T_{nn}\,\mathrm{d}s \\ &= C_T^0 - x_0 C_L + y_0 C_D = 0.162651. \end{aligned} \tag{20.15.29}$$

Now we compute C_D, C_L and C_T by integration of the normal stress over the airfoil surface. The inviscid Newtonian fluid can be achieved by setting $R_e \to \infty$ and $\beta = 0$. The results are listed in the first row of Table 20.1 and they are in perfect agreement with the classical potential flow theory. The calculation for the inviscid fluid can converge with $\Delta = 0$; we set $\Delta = 0.05$ and repeat the calculation to test the effect of Δ. The second row of Table 20.1 shows that the disturbance caused by this Δ is small and C_D, C_L and C_T remain almost the same.

The total stress can be decomposed into three parts, the inertia term, the viscous term and the viscoelastic term. For an inviscid Newtonian fluid, the inertia term is the only term in the total stress. We can probe the viscous term by setting R_e to be a finite number. In the second section in Table 20.1, we set $R_e = 1$ and 10 and $\beta = 0$. The viscous effects lead to a positive drag, indicating that the viscous stress gives rise to a drag on the airfoil in the same direction as the incoming flow. The lift C_L increases from the value for an inviscid Newtonian fluid, showing that the viscous stress gives rise to a lift force pointing upward, in the same direction as the aerodynamic lift. The viscous stress also gives rise to a counter-clockwise torque, which is in the same direction as the torque induced by the inertia term. The viscous effects are stronger when R_e is smaller.

We set $R_e \to \infty$ and $\beta = 0.01$, 0.05 and 0.1 to suppress the viscous effects and investigate the viscoelastic effects. The third section in Table 20.1 shows that the viscoelastic term gives rise to a negative drag, which is opposite to the incoming flow. The viscoelastic term leads to a negative lift, which offsets the lift by inertia and gives a total lift which points downward when β is large enough. This result is in agreement with the conclusion in DAG2004 that the inverse lift is generated by viscoelasticity of the fluid. The torque due to the viscoelastic stress is clockwise, opposite to the inertia and viscous torques.

Next we consider the combined effects of the inertia term, the viscous term and the viscoelastic term. We arbitrarily set R_e from 1 to 3 and keep β to be a constant at 0.1. When $1 \le R_e \le 2.5$, the viscous contribution to C_D outweigh the viscoelastic contribution and leads to a positive drag; however, the viscoelastic contribution to C_L prevails over the viscous contribution and gives rise to a negative lift. The viscous effects attenuate as R_e increases and the viscoelastic effects become dominant. When $R_e = 3$, both C_D and C_L are negative, showing dominant viscoelastic effects. When the torque is concerned, the viscoelastic term gives the major contribution when $1 \le R_e \le 3$ and $\beta = 0.1$ and the torque is clockwise.

We plot the normal stress on the airfoil surface as a function of the angle θ in Fig. 20.19; the three curves correspond to the inviscid Newtonian fluid with $R_e = \infty$, the viscous Newtonian fluid with $R_e = 10$, and the viscoelastic fluid with $R_e = 10$ and $\beta = 0.01$, respectively. We set $p_\infty = 0$ in this calculation. The pressure is the only component of the normal stress for the inviscid Newtonian fluid. The front nose ($\theta = \pi$) is the stagnation point and the pressure gives rise to a compressive nornal stress at $\theta = \pi$. For the Newtonian fluid with $R_e = 10$, the viscous stress comes into play; Fig. 20.19 shows that the viscous effects make the normal stress more compressive at the stagnation point. For the viscoelastic fluid with $R_e = 10$ and $\beta = 0.01$, the normal stress varies dramatically near the stagnation point. Although we cannot compute the normal stress precisely at $\theta = \pi$ because it is singular, we can compute points close to $\theta = \pi$ and connect them to obtain a curve. The curve in Fig. 20.19 shows that T_{nn} becomes tensile near $\theta = \pi$ due to the viscoelastic effects. This change of sign of the normal stress at the stagnation point plays a role in the inverse lift force on the airfoil; it also has significant importance in many unusual features in viscoelastic fluids, such as the stable orientation

R_e	β	Δ	C_D	C_L	C_T
∞	0	0	0	1.903	0.1627
∞	0	0.05	10^{-6}	1.903	0.1626
1	0	0.05	11.674	4.288	2.670
10	0	0.05	1.167	2.141	0.4134
∞	0.01	0.05	-0.3937	1.029	-0.4167
∞	0.05	0.05	-1.969	-2.465	-2.734
∞	0.1	0.05	-3.937	-6.833	-5.630
1.0	0.1	0.05	7.737	-4.449	-3.123
1.5	0.1	0.05	3.846	-5.244	-3.959
2.0	0.1	0.05	1.900	-5.641	-4.377
2.5	0.1	0.05	0.732	-5.879	-4.627
3.0	0.1	0.05	-0.0459	-6.038	-4.795

Table 20.1. *The lift, drag and torque coefficients on a Joukowski airfoil in the potential flow of a second-order fluid as a function of the controlling parameters R_e and β (20.15.4). The profile of the airfoil is determined by $m = 0.0911$ and $\delta = 0.688\pi$, and the angle of attack is fixed at $\alpha = 0$.*

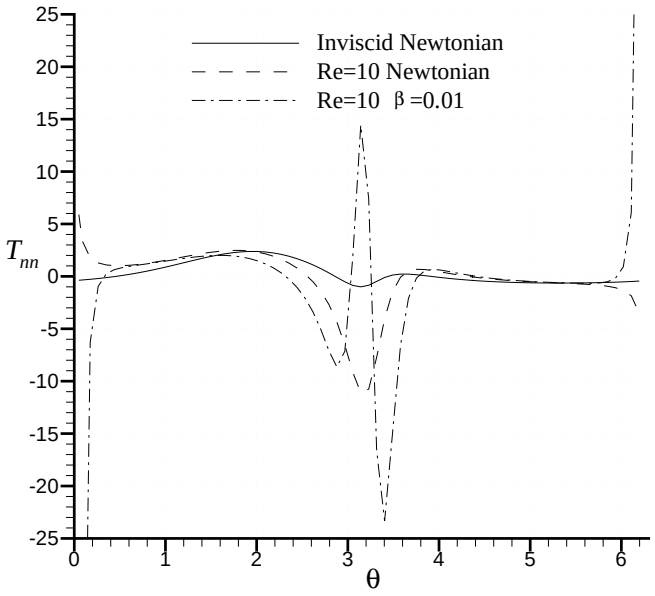

Fig. 20.19. The normal stress on the airfoil surface as a function of the angle θ. The solid line corresponds to the inviscid Newtonian fluid with $R_e = \infty$, the dashed line to the viscous Newtonian fluid with $R_e = 10$, and the dash-dotted line to the viscoelastic fluid with $R_e = 10$ and $\beta = 0.01$.

of a sedimenting long particle, chaining of particles in extensional and shear flows, and the cusp at the trailing edge of a rising air bubble (Wang and Joseph 2004).

DAG2004 measured the drag and lift on an airfoil in the streaming flow of a foam. The drag is in the same direction as the streaming flow; the lift is in the opposite direction to what would be predicted from the theory of aerodynamics. Compared to our calculation, their experiments correspond to the regime in which the viscous contribution prevails for the drag, whereas the viscoelastic contribution prevails for the lift. In Figure 20.20 the lift and drag coefficients measured by DAG2004 are plotted against the Reynolds number.

Our calculation cannot reproduce the experimental results of DAG2004 shown in Figure 20.20 quantitatively. The parameter β for the foam used in the experiments is not known. We cannot find a value of β which leads to good agreement between our calculation and the experimental results. Part of the reason may be due to the

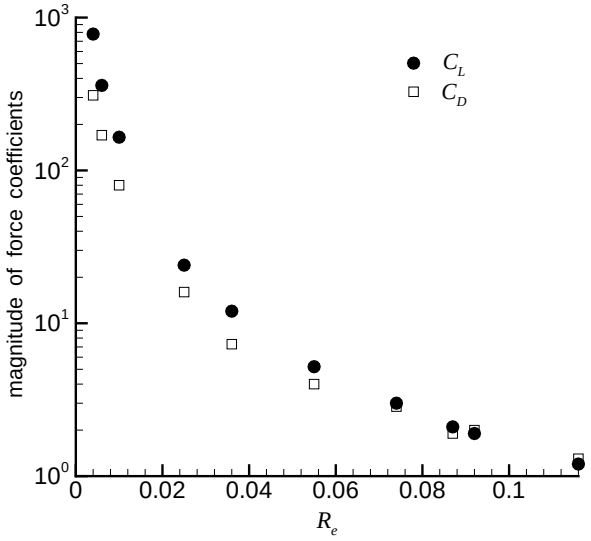

Fig. 20.20. The magnitude of C_L and C_D on an airfoil in the flow of a foam measured by DAG2004 against the Reynolds number. The drag is in the uniform flow direction; the direction of the lift force is opposite to what would be predicted from the theory of aerodynamics.

fact that the experiments of DAG2004 are in low Reynolds number ($R_e \sim 0.1$) regime and the yield stress of the foam plays an important role, which is not accounted for in the second-order fluid model. Nevertheless, our calculation can correctly predict the directions of the drag and lift and is an improvement on the inviscid potential flow theory in aerodynamics. Potential flow of a second-order fluid provides an explicit and effective way of analyzing viscoelastic effects in simple flows.